VNIVERSITAT DE VALÈNCIA

DEPARTAMENT DE FÍSICA APLICADA I ELECTROMAGNETISME

DOCTORAL PROGRAMME IN PHYSICS

NOVEL CHARACTERIZATION METHODS OF FORWARD BRILLOUIN SCATTERING IN OPTICAL FIBERS AND THEIR APPLICATIONS

DOCTORAL THESIS

LUIS ALBERTO SÁNCHEZ DOMÍNGUEZ

Valencia, June 2023

SUPERVISORS

PROF. MIGUEL V. ANDRÉS BOU

PROF. ANTONIO DÍEZ CREMADES

Dr. Miguel V. ANDRÉS BOU, Catedrático de Física Aplicada y Electromagnetismo, y Dr. Antonio DÍEZ CREMADES, Catedrático de Física Aplicada y Electromagnetismo, ambos de la Universitat de València

CERTIFICAN que la presente memoria "*Novel Characterization Methods of Forward Brillouin Scattering in Optical Fibers and their Applications*" resume el trabajo de investigación realizado, bajo su dirección, por D. Luis Alberto SÁNCHEZ DOMÍNGUEZ y constituye su Tesis para optar al Grado de Doctor en Física.

Y para que conste y en cumplimiento de la legislación vigente, firma el presente certificado en Valencia, a

Fdo. Dr. Miguel V. Andrés Bou **Fdo. Dr. Antonio Díez Cremades**

Abstract

In recent years, the potential of forward Brillouin scattering (FBS) in optical fibers has been widely recognized in the fields of sensing and characterization. A large number of the acoustic resonances responsible for this interaction can be excited in fibers by optical electrostriction using intense light pulses. However, a significant challenge in the systematic implementation of FBS is the non-trivial measurement of the interaction. Conventional phase modulation of a probe wave requires long fiber sections, leading to poor axial resolution and low quality factors of the acoustic resonances. To overcome this limitation, novel techniques for efficient and high-resolution detection and characterization of FBS signals are required.

This thesis aims to develop new techniques for FBS detection and characterization of transverse acoustic modes. These techniques are based on pump and probe schemes that convert the elastic modulation generated by the acoustic resonances into optical power modulation. The techniques consist of fiber gratings inscribed in the core of the fiber and optical whispering gallery modes, which resonate near the fiber's surface. The different responses obtained in each case are supported by a theoretical description of the excitation and detection of FBS by light pulses.

By employing the developed FBS detection methods, this work shows novel applications of FBS. By combining the characteristics of different families of acoustic resonances, the sensing and fiber characterization capabilities of FBS are greatly enhanced. Specifically, we demonstrate simultaneous sensing of strain and temperature based on the distinct sensitivity of radial and torsional-radial resonances to changes in these magnitudes. Additionally, we propose a

method for accurately measuring the Poisson's ratio in optical fibers based on frequency measurements of acoustic modes, without the need for length measurements, thereby reducing the relative error in the measurement.

Acknowledgements

I would like to express my gratitude to my thesis supervisors, Dr. Antonio Díez and Dr. Miguel V. Andrés. Their guidance, mentorship and support throughout this journey have been invaluable. Their dedication and expertise have helped shaping me into the researcher that I am today. I am also grateful to Dr. José Luis Cruz for the resources provided to carry out the experiments, and to Dr. Martina Delgado Pinar for always being willing to help and advise, not only scientifically. I would like to thank my fellow department members during these years, specially Abraham, Tomás, Josu, Daniel, Carolina, Carlos and Pablo. Their enthusiasm, knowledge, and companionship have made my work environment not only productive but also enjoyable. I would also like to express my gratitude to all the people of Photonets UV for their illusion, enthusiasm and, above all, willingness to have fun. Thanks also to the people who welcomed me in Florence during my stay, especially Dr. Silvia Soria and Dr. Gabriele Frigenti.

I would like to thank the Ministerio de Ciencia e Innovación for the FPI contract that allowed me to accomplish this thesis.

Finally, I would like to thank all the people who have helped me get here in one way or another. To my friends, both near and far, thanks for all the distraction and fun you have provided me over this period. To Stef, my partner, for her daily support, patience, love and humor. And, above all, to my family for their constant encouragement and for always believing in me.

Table of Contents

Resumen en español

Objetivos de la tesis

La interacción entre ondas electromagnéticas y acústicas ha sido un tema estudiado ampliamente desde mediados del siglo pasado, lo que ha dado lugar a ramas de estudio como son la acusto-óptica y la opto-mecánica. Las fibras ópticas son un medio excelente para la implementación de este tipo de interacción, debido a sus características de guía de onda tanto para ondas electromagnéticas como acústicas. El principio de operación de esta interacción es el siguiente: la onda acústica genera una modulación elástica del medio, lo que produce un cambio geométrico y además se traduce en una variación de las propiedades ópticas del medio debido al efecto foto-elástico.

Dependiendo de las diferentes familias de modos acústicos que puede soportar una fibra óptica, pueden ocurrir distintas interacciones con la luz. En particular, los modos acústicos transversales, cuyo vector de desplazamiento solo tiene componentes en la dirección transversal de la fibra, pueden producir la dispersión de la luz incidente en la misma dirección en la que esta se propaga. El vector de onda de estos modos acústicos es muy pequeño (en la práctica, casi nulo), lo que hace que presenten un comportamiento resonante en la dirección transversal de la fibra.

El fenómeno de la dispersión copropagante de la luz por modos acústicos transversales se conoce como *forward Brillouin scattering* (FBS), y su estudio en fibras ópticas comenzó a mediados de los años 80. Desde entonces, se han realizado numerosas técnicas para la detección de este fenómeno en fibras ópticas

convencionales, micro-fibras, fibras microestructuradas o fibras mantenedoras de polarización. Esta interacción, al principio estudiada como un efecto no deseado en comunicaciones ópticas, comenzó a alcanzar relevancia hace una década debido a las aplicaciones que empezaron a proponerse, principalmente en el campo de los sensores de fibra óptica. Así, durante los últimos años se han demostrado aplicaciones basadas en FBS para detección de líquidos a partir de la impedancia acústica, sensores de temperatura y de humedad, e incluso detectores de radiación gamma.

La presente tesis se ha desarrollado dentro del marco de *forward Brillouin scattering* en fibras ópticas. Los objetivos de la misma se pueden diferenciar en dos partes. En primer lugar, encontramos el desarrollo de nuevas técnicas eficientes de medida de FBS. En particular, hemos incidido en el desarrollo de métodos que sean relativamente sencillos de implementar y que no requieran largas secciones de fibra. Esta segunda característica, como se verá más adelante, tiene repercusión tanto en lo que se refiere a las prestaciones del método de medida, como a las aplicaciones, ya que permite dispositivos más cortos y precisos. En segundo lugar, dedicamos una buena parte del trabajo a la demostración de nuevas aplicaciones de FBS explotando las características de las técnicas de detección presentadas.

La primera parte de la tesis engloba el estudio teórico y experimental del proceso de generación de ondas acústicas transversales mediante pulsos ópticos y su detección mediante técnicas ópticas. La aportación fundamental del trabajo en relación a este aspecto se centra en el desarrollo de las técnicas de detección. Empleamos dos tipos de estrategias. Por un lado, mediante el uso de transductores locales de fibra óptica. En concreto, empleamos diferentes tipos de redes de difracción de fibra óptica. Por otro lado, a partir de las propiedades de la propia fibra óptica como microresonador óptico, basado en *whispering-gallery modes* (WGMs). En ambos casos, las perturbaciones foto-elásticas producidas por los modos acústicos transversales dan lugar a una modulación de la potencia óptica transmitida en la que queda codificada la información acercar de la oscilación

acústica de la fibra óptica. Ambas estrategias, han dado lugar a métodos de detección del proceso de FBS eficientes, con una alta resolución axial, lo que mejora sustancialmente el factor de calidad de las resonancias acústicas características del FBS.

La segunda parte de la tesis está dedicada a la demostración de nuevas aplicaciones de FBS en el ámbito del sensado y caracterización de fibra óptica, a partir de las técnicas y métodos desarrollados. El estudio en profundidad de las propiedades de las distintas resonancias acústicas que se dan en el FBS, nos ha llevado a poder demostrar que es posible ampliar las posibilidades de FBS en estos campos de aplicación combinando las distintas propiedades y respuestas de diferentes familias de ondas acústicas transversales. Como resultados más novedosos, destacamos la demostración de un sensor puntual con capacidad de medir simultáneamente deformación y temperatura, discriminando entre ambas magnitudes, y la medición del coeficiente de Poisson de una fibra óptica con una precisión sin precedente.

Fundamentos de TAMRs en fibras ópticas

Una fibra óptica puede describirse como una guía dieléctrica con simetría cilíndrica que puede guiar tanto ondas electromagnéticas como ondas acústicas. En una fibra óptica monomodo, únicamente el modo fundamental se propaga por su núcleo. Desde el punto de vista acústico, la fibra óptica, que se suele considerar como un cilindro homogéneo –las propiedades acústicas del núcleo y de la cubierta se consideran idénticas– puede soportar una gran cantidad de modos acústicos en toda su extensión. En este trabajo se ha realizado un estudio teórico de los distintos modos acústicos que pueden existir en una fibra a partir de la resolución de la ecuación de ondas elásticas para una estructura cilíndrica. A partir de las condiciones de contorno para el tensor de esfuerzo, se ha obtenido el sistema de ecuaciones homogéneo que describe los distintos modos acústicos de la fibra.

El fenómeno de *forward Brillouin scattering* involucra modos acústicos trans-

versales, con un vector de onda axial cercano a cero. Esto hace que estos modos presenten un comportamiento resonante en la dirección transversal de la fibra, con frecuencias de resonancia discretas para cada uno de los modos. Además, sus vectores de desplazamiento solo presentan componentes en las direcciones angular y azimutal. Estos modos son conocidos como *transverse acoustic mode resonances* (TAMRs). En concreto, hemos estudiado dos familias concretas de TAMRs: los modos radiales de orden azimutal $n = 0$ y los modos torsionales-radiales de orden azimutal $n = 2$, ya que son los modos que pueden ser excitados en fibras ópticas monomodo mediante electrostricción.

En fibras ópticas convencionales, los TAMRs presentan frecuencias características que van desde los 30 MHz hasta más allá de 1 GHz, dependiendo del orden del modo. Además de la resolución numérica de las frecuencias de resonancias de los TAMRs, se ha obtenido expresiones asintóticas de la ecuación característica que permiten obtener de forma analítica las frecuencias de resonancia. Estas expresiones han resultado de gran utilidad en relación al análisis de los resultados experimentales. Por otro lado, aportan información de interés en cuanto las propiedades físicas de los TAMRs. Muestran una dependencia lineal de la frecuencia de resonancia con el orden radial, en el que el factor de proporcionalidad es diferente según la familia de resonancias estudiada. Para los modos radiales, este factor depende del cociente entre la velocidad acústica longitudinal del medio y el radio de la fibra. El desarrollo asintótico ha permitido identificar dos comportamientos diferentes de los modos torsionales-radiales, lo que nos ha llevado a hablar de dos subfamilias de resonancias, una de ellas dependiente de la velocidad acústica longitudinal y la otra de la velocidad acústica de cizalla.

La disipación de la energía acústica determina el ancho espectral de las resonancias. En la tesis se estudia teóricamente las diferentes contribuciones. Estas contribuciones son esencialmente tres, cuyo origen es: la radiación de energía acústica en función de la impedancia del medio exterior, las inhomogeneidades en la geometría de la fibra y la viscosidad del medio. Para fibras desprovistas de recubrimiento e inmersas en aire, la contribución por diferencia de impedancia

al incremento en la anchura espectral de las resonancias acústicas es de aproximadamente 1 kHz. La contribución por las inhomogeneidades en la geometría dependerá del tramo de fibra en el cual se detecten las ondas acústicas. Para tramos de unos pocos centímetros, la contribución se estimó del orden de varias decenas de kHz. Por último, la contribución intrínseca por la viscosidad calculada fue del orden de varias centenas de kHz.

TAMRs en fibras ópticas pueden ser generados a partir de luz guiada mediante el proceso de electrostricción. Para ello tiene que existir un ajuste de fase entre las ondas acústica y ópticas. Dicho ajuste de fase se puede dar para frecuencias de la onda acústica próximas a la frecuencia de corte de los TAMRs. En estas condiciones, el vector de onda de los TAMRs en la dirección axial es muy pequeño, lo que hace que la energía de estos modos acústicos no se propague apenas a lo largo de la fibra. En el trabajo, se ha estudiado teóricamente la fuerza electrostrictiva que generan dos ondas electromagnéticas monocromáticas propagándose en una fibra monomodo, para diferentes casos de polarización. Se obtuvo que, ajustando las condiciones de polarización de las ondas de luz, se pueden generar unas u otras familias de TAMRs. También se estudió el caso particular de generación de TAMRs mediante pulsos ópticos, los cuales generan paquetes de ondas acústicas dentro del rango de frecuencias del ancho de banda del pulso.

Por último, se ha estudiado teóricamente la variación producida en el tensor dieléctrico de la fibra como consecuencia de la presencia de TAMRs. Las ondas acústicas generan una deformación elástica en el material, la cual deriva en una variación del tensor dieléctrico debido a la respuesta foto-elástica de la fibra. Estas variaciones en el tensor dieléctrico modulan las propiedades de propagación de las ondas electromagnéticas guiadas en la fibra y son el fundamento de todos los métodos ópticos de detección de los TAMRs, junto a las variaciones de la geometría.

Nuevas técnicas ópticas para la detección de FBS en fibras ópticas

La medición de FBS es un punto crítico a la hora de desarrollar aplicaciones basadas en este fenómeno. En la mayoría de los experimentos se generan TAMRs en la fibra óptica mediante pulsos láser intensos y la detección se fundamenta en la medida de la modulación de fase que estos provocan en una onda óptica de prueba que se hace propagar por la fibra. Estas medidas normalmente se realizan mediante técnicas interferométricas que, debido a las pequeñas eficiencias de dispersión de FBS, requieren de grandes longitudes de fibra para obtener una señal medible.

En esta parte de la tesis, se presentan nuevas técnicas alternativas para la detección de FBS basadas (1) en redes de difracción grabadas en la fibra y (2) en las propiedades de micro-resonador de las fibras ópticas, de tal modo que actúan transformando las deformaciones elásticas generadas por TAMRs en la modulación de la potencia óptica de una señal, la cual se puede detectar fácilmente mediante un fotodetector.

(1) Redes de difracción en fibra

La primera de las técnicas consiste en utilizar redes de difracción grabadas en la fibra óptica. Las redes de difracción permiten el acoplo entre distintos modos ópticos de la fibra. En el caso de las redes de Bragg, el modo fundamental propagante es acoplado al modo contrapropagante, actuando como un reflector para una determinada banda de longitud de onda. En cambio, las redes de periodo largo (LPG) acoplan el modo fundamental del núcleo a modos de la cubierta, de manera que la potencia óptica termina siendo absorbida por el recubrimiento de la fibra. En ambos casos, el espectro de la luz transmitida muestra una respuesta del tipo filtro elimina-banda, con una caída en la potencia transmitida centrada en una determinada longitud de onda de resonancia.

La longitud de onda de resonancia para la que ocurre esto depende, entre otras

cosas, de las propiedades ópticas de la fibra, en concreto del índice de refracción efectivo (índice modal) de los modos ópticos acoplados por la red de difracción. La presencia de deformaciones elásticas en la fibra hace que el índice efectivo de los modos ópticos varíe, modulando a su vez la longitud de onda de resonancia de la red de difracción. La oscilación de la longitud de onda de resonancia de la red de difracción se puede monitorizar en tiempo real sintonizando un láser de prueba a uno de los bordes del espectro de transmisión de la red, de modo que la oscilación de un TAMR dará lugar a una modulación de la potencia óptica transmitida cuya frecuencia y amplitud vendrán determinadas por las características concretas de la oscilación acústica presente.

Para la realización experimental, se grabaron diferentes redes de periodo largo y redes de Bragg en fibra óptica fotosensible mediante un láser ultravioleta. En el caso de las LPGs se empleó la técnica de grabación punto a punto mientras que para grabar las FBGs se empleó una máscara de fase. Para la generación de TAMRs en la fibra óptica, se utilizó un láser pulsado a 1 μm con duración de pulso de 700 ps. La respuesta de las redes ante la oscilación de los TAMRs se monitorizó mediante la medida, con un fotodetector rápido y un osciloscopio, de la potencia transmitida de un láser sintonizable a 1.5 μm que se sintonizó a la longitud de onda correspondiente a uno de los flancos del espectro de la red de difracción. Se utilizaron diferentes multiplexadores de fibra óptica y filtros para separar las señales de bombeo y de prueba.

La red de periodo largo utilizada en el experimento presentaba una anchura espectral de 1.3 nm y una longitud de 11 cm, y con ella se pudo medir una variación de índice efectivo del modo del núcleo desde 10^{-9} hasta 10^{-6}, en función de la potencia de bombeo. La anchura espectral de los TAMRs caracterizados con esta técnica van desde 22.5 kHz para la resonancia acústica de orden más bajo, hasta 406.8 kHz, para la resonancia de orden alto, en línea con los estimado teóricamente.

La red de Bragg utilizada presentaba una anchura espectral de 125 pm y una longitud de 1 cm. La sensibilidad demostrada de la red de Bragg fue 2.5 veces menor

que la de la red de periodo largo. Por otro lado, las redes de Bragg resultan más estables ante cambios del medio externo a la fibra, por lo que puede resultar más adecuadas para ciertas aplicaciones en las que se vean afectadas las propiedades ópticas externas a la fibra como, por ejemplo, la detección de líquidos externos basados en FBS.

(2) *Whispering-gallery modes*

La segunda técnica que presentamos para la detección y caracterización de TAMRs en fibra óptica consiste en la excitación de *whispering-gallery modes* ópticos de la propia fibra óptica a caracterizar. WGMs son modos ópticos resonantes, para los que la luz circula en la dirección azimutal de la fibra óptica, con los campos confinados muy cerca de la superficie. En este sentido, una fibra óptica es un micro-resonador dieléctrico con geometría cilíndrica. Los valores de longitud de onda óptica para los que existen los diferentes WGMs dependen de la geometría, concretamente del radio exterior de la fibra, y del índice de refracción de la misma.

Los WGMs en una fibra óptica pueden excitarse mediante el campo evanescente de una micro-fibra colocada perpendicularmente y en contacto con la fibra. De esta manera, la potencia de la luz transmitida por la micro-fibra decae cuando se acopla luz al resonador. El principio de detección de TAMRs es similar al de las redes de difracción: al producirse un cambio de índice de refracción o de radio del resonador debido a la deformación elástica, también se genera un desplazamiento de la longitud de onda de resonancia del WGM, lo que produce una modulación en la intensidad de la luz transmitida por la micro-fibra. En este caso, la amplitud de la señal modulada depende de la amplitud de la oscilación acústica, pero también de la frecuencia de la vibración y del factor de calidad del WGM.

Una de las ventajas que presenta este método se debe a que las señales de bombeo y de prueba se propagan por fibras distintas, por lo que no es necesario incluir filtros u otros elementos multiplexadores, por lo que el montaje experimental se

simplifica. Para la demostración experimental, se hizo uso de un procedimiento de tratamiento térmico de la fibra problema para obtener resonancias WGM de distintos factores de calidad. Se observó que la amplitud de modulación de la señal de prueba producida por los TAMRs presenta atenuación para las frecuencias acústicas altas, similar a un filtro paso-bajo, con una la frecuencia de corte inversamente proporcional al factor de calidad del WGM. El grueso de los experimentos se realizó con un WGM que presentaba una anchura espectral de 2.8 pm ($Q = 5.5 \times 10^5$), y la excitación de TAMRs permitió medir variaciones de la longitud de onda de resonancia del WGM de menos de 50 fm. Cabe destacar los valores de la anchura espectral de los TAMRs observados con este método, que fueron un 25 % menor que con las redes de difracción. Comprobamos, además, que los modos torsionales-radiales no son detectados mediante los WGMs debido al promediado en la dirección azimutal entre el solapamiento de campos electromagnético y acústico, que es nulo.

Por último, los resultados obtenidos con estos experimentos ponen de manifiesto que la oscilación de la longitud de onda del WGM se debe a la superposición de dos contribuciones, una debido al cambio de índice de refracción y otra debida al cambio de radio, provocados ambos por la onda acústica en la la fibra. Estas dos contribuciones presentan signos opuestos y, cuando son de magnitud comparable, pueden cancelarse parcialmente la una a la otra. Así, en el espectro de radio-frecuencia de la señal de prueba medido mediante WGMs se muestra un mínimo en amplitud para una cierta resonancia acústica.

Nuevas aplicaciones de FBS

FBS presenta un gran potencial para aplicaciones de sensado y caracterización de fibras ópticas. Debido a que los TAMRs responsables de este efecto se extienden a lo largo de toda la sección transversal de la fibra, pueden ser utilizados para medir tanto propiedades internas de la fibra como externas. La mayor parte de las aplicaciones demostradas de FBS con este fin se han enfocado únicamente en el estudio de los modos radiales o torsionales-radiales por separado. En este

trabajo demostramos que, combinando las características de ambas familias de modos acústicos, se amplían las capacidades de FBS en este ámbito.

Mediante las expresiones asintóticas obtenidas para las frecuencias de los modos radiales y torsionales-radiales, se demuestra que distintos conjuntos de modos presentan distintas dependencias con las velocidades acústicas, longitudinal y de cizalla. Con una correcta identificación de los modos acústicos en el espectro de TAMRs obtenido con alguna de las técnicas de medida demostradas, se pueden ajustar las frecuencias a estas expresiones, obteniendo valores para el cociente entre las velocidades acústicas y el radio de la fibra con gran precisión.

Medición simultánea de deformación y temperatura

La medición simultánea de la deformación elástica y la temperatura en fibras ópticas ha supuesto un reto a lo largo de la historia debido a que ambas magnitudes suelen afectar de manera similar al principio físico en el que se basan estos sensores. Normalmente, esto se resuelve mediante dos sensores diferentes (como por ejemplo, dos redes de difracción en fibra) o dos principios físicos diferentes combinados (como por ejemplo, dispersión de Brillouin y fluorescencia). En este contexto, hemos demostrado que FBS es una alternativa interesante para el sensado de deformación y temperatura gracias al hecho de que las velocidades acústicas longitudinales y de cizalla presentan dependencias diferentes con estas magnitudes.

Para la caracterización del sensor se utilizó una red de periodo largo como técnica de detección de FBS. La fibra en la que estaba grabada la red se sometió por separado a temperaturas entre -20 y $+80$ °C en una cámara térmica y a deformaciones entre 0 y 1.5 mε en una plataforma lineal para obtener los correspondientes coeficientes del sensor. Para cada valor de temperatura y de deformación se obtuvo las frecuencias de resonancia de los modos acústicos radiales y torsionales-radiales. Se demostró la capacidad de discriminación entre temperatura y deformación. A partir de las desviaciones estándar de las frecuencias relativas de los TAMRs medidas, se estimó una precisión de ± 0.2 °C para la

temperatura y de ± 25 $\mu\epsilon$ para la deformación elástica.

Medición de alta precisión del coeficiente de Poisson

Durante muchos años, se ha asumido un valor para el coeficiente de Poisson en fibras óptica de sílice fundida de entre 0.16 y 0.17, con una incertidumbre de ± 0.01. Esto ha limitado la disponibilidad de simulaciones precisas de los experimentos realizados y el desarrollo de aplicaciones que dependen de este coeficiente, como el estudio de los efectos foto-elásticos en fibras y el desarrollo de sensores. Los métodos clásicos de determinación del coeficiente de Poisson consisten en la medida de las velocidades acústicas longitudinales y de cizalla mediante técnicas que normalmente requieren la medición de las dimensiones del medio. Esto hace que los errores relativos cometidos en las medidas difícilmente sean inferiores al $10\,\%$.

En este contexto, hemos demostrado que la información sobre estas velocidades acústicas que se puede extraer a partir de FBS en fibras ópticas permite el cálculo del coeficiente de Poisson con una precisión sin precedentes. Debido a que el coeficiente de Poisson depende del cociente entre estas dos velocidades, mediante el método de ajuste de los resultados experimentales mencionado anteriormente, podemos calcular esta magnitud sin necesidad de realizar mediciones de las dimensiones de la fibra. Para la fibra empleada en el experimento se obtuvo (a temperatura ambiente y sin deformación aplicada) un valor para el coeficiente de Poisson de 0.1740 con un error relativo del 1.1‰, el cual es dos órdenes de magnitud menor que los valores reportados con anterioridad. La alta precisión de esta técnica permitió también caracterizar el coeficiente de Poisson en función de la deformación elástica y de la temperatura. Respecto a ambas magnitudes, se observó una dependencia lineal del coeficiente de Poisson, siendo los siguientes coeficientes de deformación y temperatura -2.45×10^{-7} y 3.76×10^{-5} $^{\circ}\mathrm{C}^{-1}$, respectivamente.

Conclusiones

En esta tesis se ha profundizado en el estudio de *forward Brillouin scattering* en fibras ópticas de dos maneras: en primer lugar, se han desarrollado métodos novedosos de detección de los modos acústicos que dan lugar al FBS y, en segundo lugar, se han demostrado nuevas aplicaciones del FBS a partir del análisis detallado del fenómeno y de las ventajas que proporcionan los métodos de detección desarrollados.

El trabajo experimental realizado en esta tesis, se complementa con los fundamentos teóricos que se requieren para describir adecuadamente las observaciones. En primer lugar, se presentó el marco teórico del FBS y el estudio de las ondas acústicas transversales en una fibra óptica. Se estudiaron las distintas posibilidades de excitación de TAMRs mediante electrostricción óptica en fibra monomodo, así como la disipación acústica en tramos de fibra cortos. También se estudiaron las perturbaciones que provoca los TAMRs en las propiedades de propagación de la luz en la fibra, lo que resulta la base para los métodos de detección desarrollados.

Los métodos de detección demostrados se fundamentan (1) en el uso de redes de difracción grabadas en la propia fibra y (2) en las propiedades de la fibra óptica como micro-resonadores de *whispering-gallery modes*. Con ambos métodos, las perturbaciones elásticas producidas por los TAMRs se convierten en variaciones de potencia de una señal óptica. Los resultados obtenidos demostraron que se puede detectar eficientemente FBS utilizando tramos de fibra cortos, obteniendo un alto factor de calidad para las resonancias acústicas medidas. Ambas técnicas resultan complementarias y permiten medir los TAMRs en distintas localizaciones de la fibra que pueden multiplexarse en longitud de onda, por ejemplo.

Basándonos en estas técnicas de medida, que ofrecen algunas ventajas respecto a otros métodos, y permiten de un modo práctico la caracterización del conjunto de los modos acústicos radiales y torsionales-radiales generados, hemos desarrollado nuevas aplicaciones de FBS en los campos de sensado y caracterización

de fibras ópticas. En primer lugar, se ha demostrado un sensor puntual que discrimina entre deformación elástica y temperatura, que es capaz de proporcionar ambas magnitudes simultáneamente. Esta característica se fundamenta en la distinta sensibilidad que presentan las diferentes familias de TAMRs a estas magnitudes. Como puntos fuertes de esta aplicación, podemos destacar que utiliza resonancias acústicas con alto factor de calidad y las medidas experimentales se pueden realizar en el dominio de la frecuencia con una precisión alta, lo que incide positivamente en la precisión de la respuesta del sensor. En segundo lugar, se ha desarrollado una técnica para la determinación del coeficiente de Poisson con una precisión sin precedentes, gracias a las ventajas mencionadas anteriormente. Este método es aplicable a fibras basadas en otros materiales, así como para la medición de otras propiedades elásticas.

En definitiva, las técnicas de medida y caracterización basadas en FBS descritas en esta tesis muestran un gran potencial gracias a su alta eficiencia y calidad de las resonancias. Estas técnicas pueden servir como alternativa a los sensores distribuidos demostrados hasta el momento basados en *Brillouin scattering*, los cuales requieren de montajes experimentales y métodos de procesado de señal complejos. Por otro lado, los sensores demostrados en esta tesis se fundamentan en el desplazamiento de las frecuencias de resonancia de los modos acústicos. Existen otras opciones viables, por ejemplo, sensores basados en la medida del ensanchamiento de las resonancias, que pueden beneficiarse del alto factor calidad obtenido mediante nuestras técnicas, mejorando su límite de detección y sensibilidad. Futuros trabajos podrían centrarse en el sensado a larga distancia y bajo condiciones extremas, así como sus aplicaciones en sensores medioambientales y biológicos.

1 | Introduction

Interaction between light and acoustic waves in a medium is a branch of physics that emerged in the first half of the last century, and has been fundamental to the development of the fields of acousto-optics and opto-mechanics. Acoustic waves can manipulate light by altering its amplitude and phase, deflecting it, focusing it, or changing its frequency. The basis of this interaction lies in the phenomenon of photo-elasticity, where the optical properties of the medium change due to the presence of a mechanical deformation, and in the changes of the geometry on the medium.

Optical fibers are excellent platforms for the study and implementation of this type of interaction. According to their geometry and structure, optical fibers can support different modes of optical and acoustic waves that propagate in the axial direction, which can result into the interaction between these waves with significant interaction lengths. For example, flexural acoustic waves in single-mode optical fibers can induce coupling between core and cladding optical modes, which can be utilized to develop band-rejection filters [1]. Another interaction between acoustic and optical waves in optical fibers, which is of great relevance in the field of fiber sensing, is Brillouin scattering [2]. Brillouin scattering is a nonlinear effect in which the optical beams can themselves excite or modify the acoustic field through the phenomenon of electrostriction. The most commonly observed mechanism of Brillouin scattering occurs when forward propagating light is backscattered by longitudinal acoustic waves. This effect, known as backward Brillouin scattering (BBS) or simply Brillouin scattering, was traditionally studied as an undesired effect in optical fiber communications due to the limitation on the transmitted power. In recent decades, however, significant advances have been made in the field of sensing based on BBS in optical fibers.

Distributed sensors with outstanding capabilities based on BBS are currently a reality [3, 4]. In silica optical fibers, the frequencies of these longitudinal waves are on the order of 11 GHz.

Brillouin scattering in optical fibers can also occur between copropagating optical waves. This phenomenon is known as forward Brillouin scattering (FBS); coupling between the two optical waves is met by acoustic modes close to the cutoff frequency [5]. In silica, these cutoff frequencies range from 30 MHz to beyond 1 GHz. These acoustic modes are characterized by a very small axial wave vector, which makes them to exhibit a resonance-like behaviour in the transverse plane of the fiber, being able to exhibit high quality factors.

1.1 Historical background

The study of forward Brillouin scattering of light in an optical fiber began to become relevant in the 1980s after the work of Shelby *et al.* [6]. In this work, they theoretically described and experimentally measured the forward scattered spectrum of light due to the spontaneous thermal excitation of transverse acoustic modes resonances (TAMRs) in a 56-cm uncoated single mode optical fiber. They named the interaction as guided acoustic-wave Brillouin scattering (GAWBS), emphasizing the importance of the confinement and guiding of the acoustic wave in the scattering process. Poustie *et al.* also investigated thermally-induced GAWBS in the early 1990s using optical pulses [7] and different core diameters [8]. However, their studies did not mention the optical generation of acoustic waves through electrostriction.

In 1990 and 1992, Dianov *et al.* theoretically described the long-range self-action and interaction of picosecond pulses via electrostriction in optical fibers larger than 1000 km, as an undesired effect in communication systems [9, 10]. In 1994, Golovchenko *et al.* theoretically described for the first time the excitation of both radial and torsional-radial acoustic modes by light pulses in optical fibers and the dependence on light polarization [11]. Experimental observation of electrostriction-induced TAMRs was carried out in the following

years: Nishizawa *et al.* observed radial and torsional-radial acoustic modes spectrum in polarization maintaining fibers [12], and Townsend *et al.* measured the refractive-index modulation of electrostrictively-induced radial acoustic modes using a pump-probe measurement technique in a l-km-long fiber Sagnac-loop interferometer [13]. In 1998, Du Mouza *et al.* observed, for the first time, the temporal acoustic response on a probe wave of mixed radial and torsional-radial acoustic modes [14]. A revised and more detailed model of the generation of acoustic wave generation by light pulses was presented by Biryukov *et al.* in 2002 [15], with good agreement with the experimental results in previous works.

Different nomenclatures are used in the literature to describe this interaction, each highlighting a different aspect of the scattering process. GAWBS emphasizes the importance of the confinement and guidance of the acoustic wave in the scattering process, and it is frequently used in the spontaneous thermal excitation regime. Raman-like light scattering is another term that is used, which highlights the similarity of the frequency shift to that observed in Raman scattering, both being independent on the wavelength of the optical pump. This term was commonly employed in the 2000s, in works that studied this interaction in photonic-crystal fibers [16–18], and fiber microtapers [19]. Another designation for this process, as opposed to BBS, is forward Brillouin scattering (FBS) or forward stimulated Brillouin scattering (FSBS). This term was also used by Shelby *et al.* in 1985 [20], and by Russell *et al.* in 1990 to describe intermodal forward Brillouin scattering in a dual-mode optical fiber [21]. Since the early 2010s, this is the term most commonly used in the literature to describe this interaction [22] and will be the one we will use in the scope of this thesis.

1.2 Applications of FBS in optical fibers

Although forward Brillouin scattering was studied for several decades, it has primarily been viewed as an undesired effect that should be avoided in optical communication systems rather than an interaction with potential applications. Some early studies focused on characterizing TAMRs for calculating the elastic prop-

erties of the material [23], as well as their dependence on physical parameters like temperature [24, 25] and strain [26], suggesting their potential application as sensors.

In the mid 2010s, forward Brillouin scattering starts to gain relevance again, this time focusing on its potential applications. Due to their characteristics, TAMRs are strongly dependent on the geometry of the optical fiber, as well as the elastic properties of the fiber itself and the media that surrounds it. TAMRs attenuation depends on the acoustic impedance of the surrounding medium. Based on such feature opto-mechanical sensing of liquids on the outside of uncoated fibers has been demonstrated through radial modes [27], torsional-radial modes [28], and also on the outside of thin polymide-coated fibers [29]. Wave attenuation of TAMRs has also been used to characterize the elastic properties of fiber coatings [30], and even gamma radiation sensing due to the increase in the coating stiffness [31]. Recently, highly nonlinear fibers have been proposed for conducting such experiments due to their superior signal-to-noise ratio and measurement sensitivity as compared to standard single mode fibers [32]. FBS has also been studied in polarization maintaining fibers [33], demonstrating the possibility to build up a forward Brillouin fiber laser [34].

A common issue in fiber sensing technology is the multiparameter crosstalk, that is, changes of different parameters affect in a similar way the properties of the light guided by the fiber. Hence, methods that address the joint effects of various environmental parameters and explicitly quantify each response are appreciated. In this line, FBS has been used for simultaneous and discriminated measurement of magnitudes. For example, in [35] they used both the frequency shift of TAMRs and their linewidth broadening due to the changes in temperature and relative humidity to simultaneously measure both magnitudes. Another example can be found in [36], where they simultaneously sensed temperature and acoustic impedance.

Both, point-sensing and distributed sensing schemes, have been demonstrated with FBS. Distributed sensing, i.e., continuous measurements along the length

of the fiber, with FBS is particularly challenging. In backward Brillouin scattering this can be achieved by means of time-of-flight measurements, but in forward Brillouin scattering this is non-trivial since light is scattered in the same direction as the incident one. In 2018, Chow *et al* [37] and Bashan *et al.* [38] proposed similar techniques to overcome this issue. In the first case, they measured the longitudinal phase evolution due to TAMRs of a reading optical pulse by a method similar to Brillouin optical-time domain analysis (BOTDA), achieving a resolution of 15 m in a 730-m long optical fiber [37]. In the second case, the Rayleigh backscattered light for two optical tones that are coupled by TAMRs was measured, obtaining a 100 m resolution in a 3-km fiber [38]. Some years later, Pang *et al.* improved this concept with a resolution of 2 m in a 225-m fiber by using two-tone probing of FBS [39]. Acoustic impedance point sensors based on forward Brillouin scattering have also been proposed in multi-core optical fibers by monitoring the photo-elastic perturbations on a fiber Bragg grating written in an off-axis core [40, 41].

1.3 Aim of this thesis

The objectives of this thesis can be differentiated into two main topics. In the first place, we develop new techniques for FBS detection and characterization of TAMRs, with high efficiency and axial resolution. In the second place, we demonstrate new applications of FBS in two fields: fiber optic sensing, with the development of new sensing approaches, and fiber optic characterization, regarding new methods for measurement of mechanical and geometrical properties of optical fibers.

Firstly, we establish the theoretical framework for the interaction of optical waves and TAMRs. Since the observable results of this interaction depend on a large number of variables such as geometry, characteristics of medium and measurement method, an in-depth theoretical description is necessary for their correct interpretation. The general and particular descriptions of the phenomenon are given in Chapter 2 and Chapter 3.

One objective of this thesis is the implementation of new optical techniques for the detection of forward Brillouin scattering in optical fibers. With these techniques, the photo-elastic perturbation generated by transverse acoustic modes is converted into optical power modulation in a simple and efficient way. The methods included in this thesis are based on in-fiber components, in particular, different type of fiber gratings, and on whispering gallery mode resonances. In many aspects, these techniques overcome the performance of techniques previously shown. They allow high resolution, point measurement of FBS with a much simpler experimental set-up, as well as making it possible to be implemented in a wide variety of optical fibers. The quality factor of the measured acoustic resonances is also substantially enhanced by using these techniques. The experimental results for the detection of FBS are presented in Chapter 3.

Another objective of this work is focused on the demonstration of new applications of FBS using the developed detection techniques, as presented in Chapter 4. By combining the properties and responses of various types of optically-excited TAMRs, we present novel sensing and characterization applications of FBS. Specifically, we demonstrate a highly sensitive strain and temperature point sensor with simultaneous and discriminative measurements. Additionally, we show that FBS can be employed for accurate measurements of the elastic properties of optical fibers, in particular measurement of the Poisson's ratio is reported. It can be remarked that sensing methods based on TAMRs can rely on its frequency features, which can be measured very accurately, thus, they can provide unparalleled precision. Such feature allowed us, for example, investigating the dependence of the Poisson's ratio on magnitudes like temperature and strain.

References

[1] E. P. Alcusa-Sáez, A. Díez, E. Rivera-Pérez, W. Margulis, L. Norin, and M. V. Andrés, "Acousto-optic interaction in polyimide coated optical fibers with flexural waves", *Optics Express*, vol. 25, no. 15, p. 17 167, 2017.

[2] L. Brillouin, "Diffusion de la lumière et des rayons X par un corps transparent homogène - influence de l'agitation thermique", *Annales de Physique*, vol. 9, no. 1717, pp. 88–122, 1922.

[3] M. Niklès, L. Thévenaz, and P. A. Robert, "Simple distributed fiber sensor based on Brillouin gain spectrum analysis", *Optics Letters*, vol. 21, no. 10, p. 758, 1996.

[4] C. A. Galindez-Jamioy and J. M. López-Higuera, "Brillouin distributed fiber sensors: An overview and applications", *Journal of Sensors*, vol. 2012, pp. 1–17, 2012.

[5] C. Wolff, M. J. A. Smith, B. Stiller, and C. G. Poulton, "Brillouin scattering—theory and experiment: Tutorial", *Journal of the Optical Society of America B*, vol. 38, no. 4, p. 1243, 2021.

[6] R. M. Shelby, M. D. Levenson, and P. W. Bayer, "Guided acoustic-wave Brillouin scattering", *Phys. Rev. B*, vol. 31, pp. 5244–5252, 8 1985.

[7] A. J. Poustie, "Guided acoustic-wave Brillouin scattering with optical pulses", *Journal of the Optical Society of America B*, vol. 17, no. 4, p. 691, 1993.

[8] A. J. Poustie, "Bandwidth and mode intensities of guided acoustic-wave Brillouin scattering in optical fibers", *Journal of the Optical Society of America B*, vol. 10, no. 4, p. 691, 1993.

[9] E. M. Dianov, A. V. Luchnikov, A. N. Pilipetskii, and A. N. Starodumov, "Electrostriction mechanism of soliton interaction in optical fibers", *Optics Letters*, vol. 15, no. 6, p. 314, 1990.

[10] E. M. Dianov, A. V. Luchnikov, A. N. Pilipetskii, and A. M. Prokhorov, "Long-range interaction of picosecond solitons through excitation of

acoustic waves in optical fibers", *Applied Physics B Photophysics and Laser Chemistry*, vol. 54, no. 2, pp. 175–180, 1992.

[11] E. A. Golovchenko and A. N. Pilipetskii, "Acoustic effect and the polarization of adjacent bits in soliton communication lines", *Journal of Lightwave Technology*, vol. 12, no. 6, pp. 1052–1056, 1994.

[12] N. Nishizawa, S. Kume, M. Mori, T. Goto, and A. Miyauchi, "Characteristics of guided acoustic wave Brillouin scattering in polarization maintaining fibers", *Optical Review*, vol. 3, no. 1, pp. 29–33, 1996.

[13] P. D. Townsend, A. J. Poustie, P. J. Hardman, and K. J. Blow, "Measurement of the refractive-index modulation generated by electrostriction-induced acoustic waves in optical fibers", *Optics Letters*, vol. 21, no. 5, p. 333, 1996.

[14] L. Du Mouza, Y. Jaouën, and C. Chabran, "Transverse Brillouin effect characterization in optical fibers and its geometrical aspects", *IEEE Photonics Technology Letters*, vol. 10, no. 10, pp. 1455–1457, 1998.

[15] A. S. Biryukov, M. E. Sukharev, and E. M. Dianov, "Excitation of sound waves upon propagation of laser pulses in optical fibres", *Quantum Electronics*, vol. 32, no. 9, pp. 765–775, 2002.

[16] P. Dainese *et al.*, "Raman-like light scattering from acoustic phonons in photonic crystal fiber", *Optics Express*, vol. 14, no. 9, p. 4141, 2006.

[17] J.-C. Beugnot, T. Sylvestre, H. Maillotte, G. Mélin, and V. Laude, "Guided acoustic wave Brillouin scattering in photonic crystal fibers", *Optics Letters*, vol. 32, no. 1, p. 17, 2007.

[18] M. S. Kang, A. Nazarkin, A. Brenn, and P. S. J. Russell, "Tightly trapped acoustic phonons in photonic crystal fibres as highly nonlinear artificial Raman oscillators", *Nature Physics*, vol. 5, no. 4, pp. 276–280, 2009.

[19] M. S. Kang, A. Brenn, G. S. Wiederhecker, and P. S. J. Russell, "Optical excitation and characterization of gigahertz acoustic resonances in optical fiber tapers", *Applied Physics Letters*, vol. 93, no. 13, pp. 65–68, 2008.

[20] R. M. Shelby, M. D. Levenson, and P. W. Bayer, "Resolved forward Brillouin scattering in optical fibers", en, *Physical Review Letters*, vol. 54, no. 9, pp. 939–942, 1985.

[21] P. S. J. Russell, D. Culverhouse, and F. Farahi, "Experimental observation of forward stimulated Brillouin scattering in dual-mode single-core fibre", *Electronics Letters*, vol. 26, no. 15, pp. 1195–1196, 1990.

[22] J. Wang, Y. Zhu, R. Zhang, and D. J. Gauthier, "FSBS resonances observed in a standard highly nonlinear fiber", *Optics express*, vol. 19, no. 6, pp. 5339–5349, 2011.

[23] K. Shiraki and M. Ohashi, "Sound velocity measurement based on guided acoustic-wave Brillouin scattering", *IEEE Photonics Technology Letters*, vol. 4, no. 10, p. 1177, 1992.

[24] Y. Tanaka and K. Ogusu, "Temperature coefficient of sideband frequencies produced by depolarized guided acoustic-wave Brillouin scattering", *IEEE Photonics Technology Letters*, vol. 10, no. 12, p. 1769, 1998.

[25] E. Carry, J.-C. Beugnot, B. Stiller, M. W. Lee, H. Maillotte, and T. Sylvestre, "Temperature coefficient of the high-frequency guided acoustic mode in a photonic crystal fiber", *Applied Optics*, vol. 50, no. 35, p. 6543, 2011.

[26] Y. Tanaka and K. Ogusu, "Tensile-strain coefficient of resonance frequency of depolarized guided acoustic-wave Brillouin scattering", *IEEE Photonics Technology Letters*, vol. 11, no. 7, p. 865, 1999.

[27] Y. Antman, A. Clain, Y. London, and A. Zadok, "Optomechanical sensing of liquids outside standard fibers using forward stimulated Brillouin scattering", *Optica*, vol. 3, no. 5, p. 510, 2016.

[28] N. Hayashi, Y. Mizuno, K. Nakamura, S. Y. Set, and S. Yamashita, "Experimental study on depolarized GAWBS spectrum for optomechanical sensing of liquids outside standard fibers", *Optics Express*, vol. 25, no. 3, p. 2239, 2017.

[29] D. M. Chow and L. Thévenaz, "Forward Brillouin scattering acoustic impedance sensor using thin polyimide-coated fiber", *Optics Letters*, vol. 43, no. 21, p. 5467, 2018.

[30] H. H. Diamandi, Y. London, G. Bashan, K. Shemer, and A. Zadok, "Forward stimulated Brillouin scattering analysis of optical fibers coatings", *Journal of Lightwave Technology*, vol. 39, no. 6, pp. 1800–1807, 2021.

[31] Y. London *et al.*, "Opto-mechanical fiber sensing of gamma radiation", vol. 39, pp. 6637–6645, 2021.

[32] K. Zeng *et al.*, "High-sensitivity acoustic impedance sensing based on forward Brillouin scattering in a highly nonlinear fiber", *Optics Express*, vol. 31, no. 5, p. 8595, 2023.

[33] G. Bashan *et al.*, "Forward stimulated Brillouin scattering and opto-mechanical non-reciprocity in standard polarization maintaining fibres", *Light: Science & Applications*, vol. 10, no. 1, p. 119, 2021.

[34] G. Bashan, H. H. Diamandi, E. Zehavi, K. Sharma, Y. London, and A. Zadok, "A forward Brillouin fibre laser", *Nature Communications*, vol. 13, no. 1, p. 3554, 2022.

[35] Y. Xu, X. Zhao, Y. Li, Z. Qin, Y. Pang, and Z. Liu, "Simultaneous measurement of relative humidity and temperature based on forward Brillouin scattering in polyimide-overlaid fiber", *Sensors and Actuators B: Chemical*, vol. 348, no. September, p. 130 702, 2021.

[36] Z. Zhang, Y. Lu, Y. Tanaka, J. Peng, and Z. Zhuang, "Discriminative sensing of temperature and acoustic impedance by using forward Brillouin scattering in large effective area fiber", *Applied Physics Express*, vol. 14, no. 4, 2021.

[37] D. M. Chow, Z. Yang, M. A. Soto, and L. Thévenaz, "Distributed forward Brillouin sensor based on local light phase recovery", *Nature communications*, vol. 9, no. 1, pp. 1–9, 2018.

[38] G. Bashan, H. H. Diamandi, Y. London, E. Preter, and A. Zadok, "Optomechanical time-domain reflectometry", en, *Nature Communications*, vol. 9, no. 1, p. 2991, 2018.

[39] C. Pang *et al.*, “Opto-mechanical time-domain analysis based on coherent forward stimulated Brillouin scattering probing”, en, *Optica*, vol. 7, no. 2, p. 176, 2020.

[40] H. H. Diamandi *et al.*, “Opto-mechanical interactions in multi-core optical fibers and their applications”, *IEEE Journal of Selected Topics in Quantum Electronics*, vol. 26, no. 4, 2020.

[41] K. Shemer *et al.*, “Optical fiber point sensors based on forward Brillouin scattering”, *Optics Express*, vol. 30, no. 22, p. 39 321, 2022.

2 | Fundamentals of TAMRs in optical fibers

An optical fiber can be described as a cylindrical dielectric waveguide that can guide both, acoustic and optical waves. Interactions between these two types of waves are known as opto-acoustic interactions. In a single-mode fiber, only the fundamental optical mode propagates through the fiber core. Regarding to the acoustic properties, an optical fiber can be considered as a homogeneous cylinder –acoustic properties of core and cladding are considered identical– that can support a large number of different acoustic modes. In this chapter, we will review the main theoretical features of the opto-acoustic interaction for the purpose of this work. First, we will describe the different acoustic modes in optical fibers by solving the elastic wave equation for an isotropic cylinder with special emphasis on transverse acoustic mode resonances (TAMRs), which are the acoustic modes responsible for forward Brillouin scattering. Then, we will focus on the generation of TAMRs through optical electrostriction in single-mode fibers in different scenarios, including optical pulses. Finally, we will analyze photo-elastic perturbations caused by TAMRs to optical guided modes in the fiber.

2.1 Elastic modes in optical fibers

The dynamics of elastic modes in solids can be described by the equation of motion for the particle displacement field $\mathbf{U}(\mathbf{r},t)$ [m]. In the absence of external driving forces, an acoustic wave propagating through a lossless medium is

described by the elasto-dynamic equation,

$$\rho \frac{\partial^2 U_i}{\partial t^2} = \frac{\partial T_{ij}}{\partial x_j}, \tag{2.1}$$

where T_{ij} is the stress tensor, $i, j \in \{x, y, z\}$ denote the Cartesian coordinates and ρ is the density of the medium. For small forces, the stress T_{ij} can be related to the strain S_{kl} through a linear relationship by means of the elastic stiffness tensor c_{ijkl},

$$T_{ij} = c_{ijkl} S_{kl}, \tag{2.2}$$

$$S_{kl} = \frac{1}{2}\left(\frac{\partial U_k}{\partial x_l} + \frac{\partial U_l}{\partial x_k}\right). \tag{2.3}$$

Both T_{ij} and S_{kl} are symmetric second rank tensors, consequently they only have 6 independent components. This reduces the number of components for the fourth rank tensor c_{ijkl} from 81 to 36. Further reduction for the stiffness tensor can be demonstrated in the case of an elastic material which preserves the energy [1]. In this instance, c_{ijkl} is also symmetric and the number of independent components is 21.

From a mechanical point of view an optical fiber can be considered as an isotropic, solid cylinder. We will also assume the fiber is a homogeneous medium, neglecting the small differences between the elastic properties of the core and the cladding of the fiber [2]. For an isotropic linear elastic material, the response of the material to stress is the same in all directions, i.e. the stiffness tensor must be invariant under rotations. This reduces the stiffness constants to,

$$c_{ijkl} = \lambda \delta_{ij} \delta_{kl} + \mu \left(\delta_{ik} \delta_{jl} + \delta_{il} \delta_{jk}\right), \tag{2.4}$$

where δ_{mn} is the Kronecker delta, and λ and μ are the Lamé coefficients of the material.

2.1.1 Elastic wave equation

For an isotropic linear elastic medium with no losses, the homogeneous equation 2.1 can be expressed in the following vector form,

$$(\lambda+\mu)\nabla(\nabla\cdot\mathbf{U})+\mu\nabla^2\mathbf{U}-\rho\frac{\partial^2\mathbf{U}}{\partial t^2}=0. \tag{2.5}$$

In this equation, the three components of the displacement vector $\mathbf{U}$ are coupled. To obtain decoupled equations, we will assume a solution containing a scalar potential ϕ and a vector potential $\mathbf{\Psi}$ so that $\mathbf{U}=\nabla\phi+\nabla\times\mathbf{\Psi}$. If we substitute this into 2.5, taking into account that $\nabla\times(\nabla\phi)=0$ and $\nabla\cdot(\nabla\times\mathbf{\Psi})=0$, we have two separate equations for the scalar and vector potentials,

$$\nabla^2\phi-\frac{1}{V_L^2}\frac{\partial^2\phi}{\partial t^2}=0 \tag{2.6}$$

$$\nabla^2\mathbf{\Psi}-\frac{1}{V_S^2}\frac{\partial^2\mathbf{\Psi}}{\partial t^2}=0. \tag{2.7}$$

These equations show that each potential propagates independently of the other, with longitudinal and shear velocities given by $V_L=\sqrt{(\lambda+2\mu)/\rho}$ and $V_S=\sqrt{\mu/\rho}$. For silica, these values are $V_L=5996\,\mathrm{m/s}$ and $V_S=3740\,\mathrm{m/s}$ under room conditions of pressure and temperature. Equation 2.6 corresponds to longitudinal waves since it gives $\nabla\times\mathbf{U}=0$, whereas equation 2.7 describes shear waves due to $\nabla\cdot\mathbf{U}=0$. It is important to note that, since we have expressed the displacement vector $\mathbf{U}$ as a combination of the scalar and vector potentials ϕ and $\mathbf{\Psi}$, we have increased the number of variables by one, giving us the opportunity to impose a relation between these four variables.

2.1.2 Cylindrical waveguide

Due to the cylindrical symmetry of an optical fiber, it is useful to adopt a cylindrical coordinate system (r,ϕ,z) as shown in Fig. 2.1. In order to solve the wave

equation 2.6, we will assume that the scalar potential ϕ can be expressed as,

$$\phi = f(r)\, g(\phi)\, e^{j(\Omega t - Kz)}, \tag{2.8}$$

where $f(r)$ and $g(\phi)$ are functions that describe the radial and azimuthal profile, respectively, and we have considered a time-harmonic wave propagating along the z axis. Now, we can split the wave equation into two parts, one for the radial profile $f(r)$ and another for the angular variation $g(\phi)$,

$$\frac{d^2 g}{d\phi^2} + n^2 g = 0, \tag{2.9}$$

$$\frac{d^2 f}{dr^2} + \frac{1}{r}\frac{df}{dr} + \left(\frac{\Omega^2}{V_L^2} - K^2\right) f - \frac{n^2}{r^2} f = 0, \tag{2.10}$$

where n is a decoupling constant. The solutions of Eq. 2.9 are $\sin(n\phi)$ and $\cos(n\phi)$. The continuity and periodicity of the azimuthal variation of ϕ implies that n must be an integer number. Eq. 2.10 is satisfied by Bessel functions [3] of integer order n. Given that ϕ must be finite at $r = 0$, the solutions for the radial differential equation must involve only Bessel functions of the first kind, J_n. The solution for ϕ is then,

$$\phi = C_1 J_n(pr) \left\{ \begin{matrix} \cos(n\phi) \\ \sin(n\phi) \end{matrix} \right\} e^{j(\Omega t - Kz)}, \tag{2.11}$$

where $p^2 = (\Omega^2/V_L^2) - K^2$.

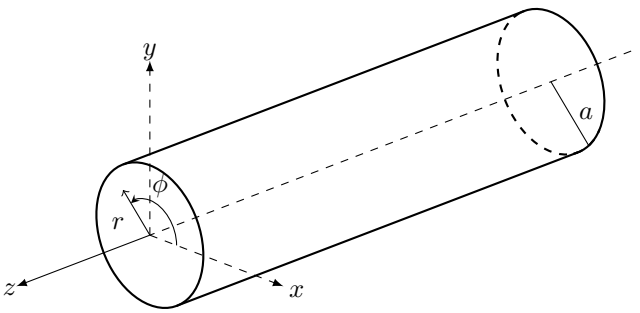

Figure 2.1: Cylindrical coordinate system. The radius of the cylinder is a.

We can follow a similar procedure for the vector potential $\boldsymbol{\Psi}$. By applying the Laplacian to $\boldsymbol{\Psi}$ in Eq. 2.7, we obtain three different equations. Assuming a time-harmonic dependence,

$$\nabla^2\Psi_r - \frac{\Psi_r}{r^2} - \frac{2}{r^2}\frac{\partial\Psi_\phi}{\partial\phi} + \frac{\Omega^2}{V_S^2}\Psi_r = 0, \tag{2.12}$$

$$\nabla^2\Psi_\phi - \frac{\Psi_\phi}{r^2} + \frac{2}{r^2}\frac{\partial\Psi_r}{\partial\phi} + \frac{\Omega^2}{V_S^2}\Psi_\phi = 0, \tag{2.13}$$

$$\nabla^2\Psi_z + \frac{\Omega^2}{V_S^2}\Psi_z = 0. \tag{2.14}$$

We can see that Eq. 2.14 is analogous to Eq. 2.6 for the scalar potential. In the same way, we will assume a similar solution for Ψ_z,

$$\Psi_z = C_2\, J_n(qr)\left\{\begin{smallmatrix}\sin(n\phi)\\ -\cos(n\phi)\end{smallmatrix}\right\} e^{j(\Omega t - Kz)}, \tag{2.15}$$

with $q^2 = (\Omega^2/V_S^2) - K^2$. The radial and azimuthal components are coupled through Eqs. 2.12 and 2.13. We will assume solutions for these components similar to the previous ones with unknown radial profiles,

$$\Psi_r = \Psi_r(r)\left\{\begin{smallmatrix}\sin(n\phi)\\ -\cos(n\phi)\end{smallmatrix}\right\} e^{j(\Omega t - Kz)}, \tag{2.16}$$

$$\Psi_\phi = \Psi_\phi(r)\left\{\begin{smallmatrix}\cos(n\phi)\\ \sin(n\phi)\end{smallmatrix}\right\} e^{j(\Omega t - Kz)}. \tag{2.17}$$

The presence of orthogonal trigonometric factors in Eqs. 2.16 and 2.17 is justified because the angular derivative of the coupled terms for Ψ_r and Ψ_ϕ are of opposite signs. If we substitute these solutions into Eqs. 2.12 and 2.13, we obtain these two differential equations,

$$\frac{d^2\Psi_r}{dr^2} + \frac{1}{r}\frac{d\Psi_r}{dr} + \frac{1}{r^2}(-n^2\Psi_r + 2n\Psi_\phi - \Psi_r) + q^2\Psi_r = 0, \tag{2.18}$$

$$\frac{d^2\Psi_\phi}{dr^2} + \frac{1}{r}\frac{d\Psi_\phi}{dr} + \frac{1}{r^2}(-n^2\Psi_\phi + 2n\Psi_r - \Psi_\phi) + q^2\Psi_\phi = 0, \tag{2.19}$$

which are the same equation but interchanging the indices r and ϕ. By subtracting and adding these two equations, we obtain two new equations whose solutions are,

$$\Psi_r - \Psi_\phi = 2C_3 J_{n+1}(qr), \tag{2.20}$$

$$\Psi_r + \Psi_\phi = 2C_4 J_{n-1}(qr). \tag{2.21}$$

As we discussed before, the displacement field $\mathbf{U}$ has three components, while the potential function formulation provides four unknown constants C_1, C_2, C_3 and C_4. Without loss of generality, any of these constants C_i can be equated to zero. We will conveniently set $C_4 = 0$ so that $\Psi_r = -\Psi_\phi$. Thus, the expressions for the scalar and vector potential are,

$$\phi = C_1 J_n(pr) \left\{ \begin{matrix} \cos(n\phi) \\ \sin(n\phi) \end{matrix} \right\} e^{j(\Omega t - Kz)}, \tag{2.22}$$

$$\Psi_r = C_3 J_{n+1}(qr) \left\{ \begin{matrix} \sin(n\phi) \\ -\cos(n\phi) \end{matrix} \right\} e^{j(\Omega t - Kz)}, \tag{2.23}$$

$$\Psi_\phi = -C_3 J_{n+1}(qr) \left\{ \begin{matrix} \cos(n\phi) \\ \sin(n\phi) \end{matrix} \right\} e^{j(\Omega t - Kz)}, \tag{2.24}$$

$$\Psi_z = C_2 J_n(qr) \left\{ \begin{matrix} \sin(n\phi) \\ -\cos(n\phi) \end{matrix} \right\} e^{j(\Omega t - Kz)}. \tag{2.25}$$

We can now calculate the components of the displacement field through the expression $\mathbf{U} = \nabla\phi + \nabla \times \mathbf{\Psi}$,

$$U_r = \left[C_1 p J_n'(pr) + C_2 \frac{n}{r} J_n(qr) + jC_3 K J_{n+1}(qr) \right] \left\{ \begin{matrix} \cos(n\phi) \\ \sin(n\phi) \end{matrix} \right\} e^{j(\Omega t - Kz)}, \tag{2.26}$$

$$U_\phi = \left[C_1 \frac{n}{r} J_n(pr) + C_2 q J_n'(qr) - jC_3 K J_{n+1}(qr) \right] \left\{ \begin{matrix} -\sin(n\phi) \\ \cos(n\phi) \end{matrix} \right\} e^{j(\Omega t - Kz)}, \tag{2.27}$$

$$U_z = \left[jC_1 K J_n(pr) - C_3 q J_n(qr) \right] \left\{ \begin{matrix} \cos(n\phi) \\ \sin(n\phi) \end{matrix} \right\} e^{j(\Omega t - Kz)}. \tag{2.28}$$

The strain tensor can be calculated from the displacement field using Eq. 2.3. In cylindrical coordinates, this is given by,

$$S_{rr} = \frac{\partial U_r}{\partial r}, \tag{2.29}$$

$$S_{\phi\phi} = \frac{1}{r}\left(\frac{\partial U_\phi}{\partial \phi} + U_r\right), \tag{2.30}$$

$$S_{zz} = \frac{\partial U_z}{\partial z}, \tag{2.31}$$

$$S_{r\phi} = \frac{1}{2}\left(\frac{1}{r}\frac{\partial U_r}{\partial \phi} + \frac{\partial U_\phi}{\partial r} - \frac{U_\phi}{r}\right), \tag{2.32}$$

$$S_{\phi z} = \frac{1}{2}\left(\frac{\partial U_\phi}{\partial z} + \frac{1}{r}\frac{\partial U_z}{\partial \phi}\right), \tag{2.33}$$

$$S_{rz} = \frac{1}{2}\left(\frac{\partial U_r}{\partial z} + \frac{\partial U_z}{\partial r}\right). \tag{2.34}$$

2.1.3 Boundary conditions

For an infinite cylindrical waveguide which is not subjected to external stress, stress free boundary condition at the curved surface apply, i.e., the components T_{rr}, $T_{r\phi}$ and T_{rz} of the stress tensor must be zero at $r = a$ (see Fig. 2.2). We can express these three components of the stress tensor in terms of the displacement field using Eqs. 2.2 and 2.3,

$$T_{rr} = \lambda S + 2\mu \frac{\partial U_r}{\partial r}, \tag{2.35}$$

$$T_{r\phi} = \mu\left[\frac{1}{r}\left(\frac{\partial U_r}{\partial \phi} - U_\phi\right) + \frac{\partial U_\phi}{\partial r}\right], \tag{2.36}$$

$$T_{rz} = \mu\left(\frac{\partial U_r}{\partial z} + \frac{\partial U_z}{\partial r}\right), \tag{2.37}$$

where $S = \nabla \cdot \mathbf{U}$. If we calculate T_{rr}, $T_{r\phi}$ and T_{rz} using Eqs. 2.26, 2.27 and 2.28 and equal them to zero at $r = a$, we obtain the following system of equations,

$$\begin{pmatrix} [-q^2+K^2+\frac{2}{a^2}n(n+1)]J_n(pa) & \frac{2n}{a}[-\frac{n+1}{a}J_n(qa) & j2K\{[q-\frac{2}{qa^2}n(n+1)]J_n(qa) \\ -\frac{2p}{a}J_{n-1}(pa) & +qJ_{n-1}(qa)] & +\frac{n+1}{a}J_{n-1}(pa)\} \\ \frac{2n}{a}[\frac{n+1}{a}J_n(pa) & [q^2-\frac{2}{a^2}n(n+1)]J_n(qa) & jK\{[q-\frac{4}{qa^2}n(n+1)]J_n(qa) \\ -pJ_{n-1}(pa)] & +\frac{2q}{a}J_{n-1}(qa) & +\frac{2}{a}(n+1)J_{n-1}(qa)\} \\ j2K[-\frac{n}{a}J_n(pa) & j\frac{nK}{a}J_n(qa) & \frac{n}{qa}(q^2-2K^2)J_n(qa) \\ +pJ_{n-1}(pa)] & & -(q^2-K^2)J_{n-1}(qa) \end{pmatrix} \begin{pmatrix} C_1 \\ C_2 \\ C_3 \end{pmatrix} = 0, \tag{2.38}$$

where we have used the identity $\lambda(p^2+K^2)+2\mu p^2 = \mu(q^2-K^2)$ to eliminate λ from T_{rr}. The homogeneous system is valid for all integer values $n \geq 0$. Non-trivial solutions are obtained by setting the determinant of the coefficient matrix equal to zero.

Equation 2.38 yields the wavenumber K of spatial acoustic modes in the cylindrical waveguide that propagate in the axial direction with fields oscillating at a frequency Ω. Modes with $n = 0$ are known as axially symmetric modes because the argument of the sets of trigonometric functions is zero, thus their fields do

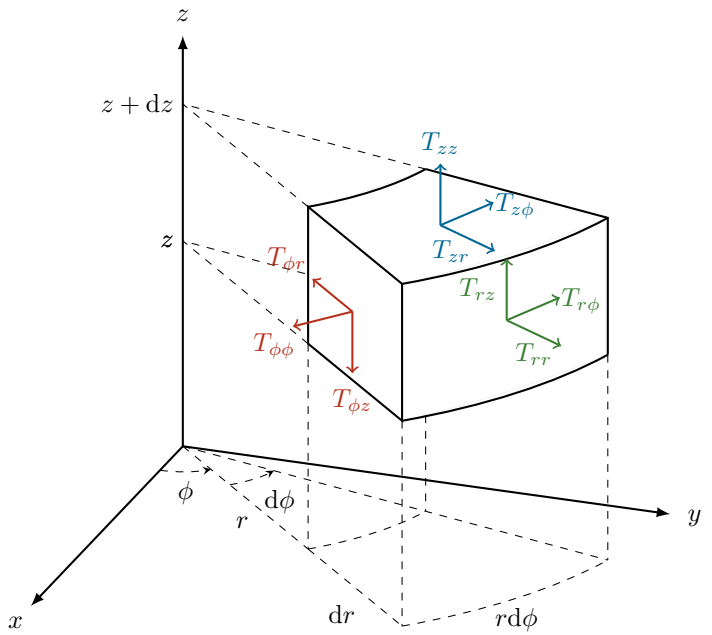

Figure 2.2: Stress tensor components in cylindrical coordinates.

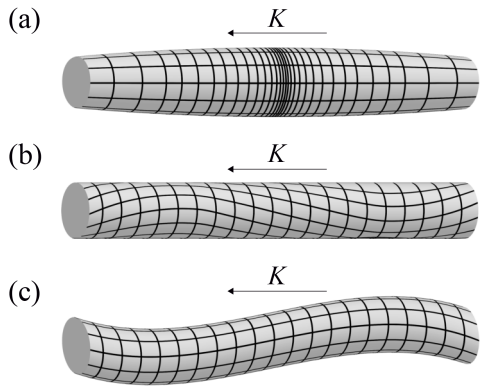

Figure 2.3: Representation of the displacement fields for different acoustic modes in a cylindrical waveguide. (a) Longitudinal or dilatational modes. (b) Torsional modes. (c) Flexural modes.

not depend on the azimuthal coordinate [1, 4, 5]. In this case, for the upper set of trigonometric equations we obtain the Pochhammer-Chree equation, which gives the longitudinal or dilatational modes (Fig. 2.3(a)). These modes are described by a displacement vector with components $U_r(r,z,t)$ and $U_z(r,z,t)$. The lower set of trigonometric equations, describe torsional modes, whose displacement vector contains only the $U_\phi(r,z,t)$ component (Fig. 2.3(b)). Modes with $n = 1$ are the lowest order flexural modes. Radial motions at opposite points of the transverse section of the cylinder move in anti-phase, causing a flexing motion of the solid (Fig. 2.3(c)). In general, this motion involves all three displacement components U_r, U_ϕ and U_z with dependence on the three cylindrical coordinates. Modes with $n \geq 2$ are known as high order flexural modes.

2.2 Transverse acoustic mode resonances

A special case of acoustic modes in a cylindrical waveguide occurs when the axial wavenumber $K = 0$ and the modes reach their cutoff frequency. In this case, acoustic modes do not propagate along the waveguide and they can only exist at discrete acoustic frequencies. They exhibit a resonant-like behavior. For these resonances, the axial component U_z of the displacement vector is always

zero. They are known as transverse acoustic mode resonances (TAMRs). For the aim of this thesis we will focus only on two types of TAMRs: radial modes $R_{0,m}$ and torsional-radial modes with $n = 2$, $TR_{2,m}$. We focused on these two type of modes since they are the only acoustic modes involved in the process of forward Brillouin scattering in single-mode optical fibers, on which the thesis is focused. Acoustic waves with axial wavenumbers very close to zero similar to these acoustic resonances can be easily excited in single-mode optical fibers through optical electrostriction. The displacement vector of $R_{0,m}$ contains only the radial component U_r, which depends only on the radial coordinate, r. For torsional-radial modes, the two components of the displacement, U_r and U_ϕ are nonzero, and they depend on the radial coordinate r and the azimuthal angle ϕ.

For negligible values of the wavenumber K, p and q can be approximated by $p \approx \Omega/V_L$ and $q \approx \Omega/V_S$, and equation 2.38 can be separated into two different conditions,

$$\begin{pmatrix} \left[-\zeta^2+2n(n+1)\right]J_n(\alpha\zeta)-2\alpha\zeta J_{n-1}(\alpha\zeta) & 2n\left[-(n+1)J_n(\zeta)+\zeta J_{n-1}(\zeta)\right] \\ 2n\left[(n+1)J_n(\alpha\zeta)-\alpha\zeta J_{n-1}(\alpha\zeta)\right] & \left[\zeta^2-2n(n+1)\right]J_n(\zeta)+2\zeta J_{n-1}(\zeta) \end{pmatrix} \begin{pmatrix} C_1 \\ C_2 \end{pmatrix} = 0, \quad (2.39)$$

$$\left[n\zeta J_n(\zeta) - \zeta^2 J_{n-1}(\zeta)\right] C_3 = 0, \quad (2.40)$$

where $\zeta = \Omega a/V_S$ is the normalized acoustic frequency and $\alpha = V_S/V_L$. Equation 2.40 corresponds to resonances with purely axial displacement, as we can set the coefficients C_1 and C_2 to zero. The condition 2.39 refers to resonances with displacement fields in the transverse plane as $C_3 = 0$.

For each TAMR, we can define a normalized displacement $\mathbf{u}^{(n,m)}$ [m^{-1}] such that,

$$\mathbf{U}^{(n,m)}(r,\phi,t) = B^{(0)}_{n,m} \cdot \mathbf{u}^{(n,m)}(r,\phi)\, e^{j\Omega t}, \quad (2.41)$$

$$\int_0^a \int_0^{2\pi} |\mathbf{u}^{(n,m)}(r,\phi)|^2 r dr d\phi = 1, \quad (2.42)$$

where a lossless medium has been assumed. The relation between the total displacement field and the normalized one is given through the amplitude $B^{(0)}_{n,m}$ [m^2]

that will depend on the excitation mechanism for the transverse acoustic mode resonances. Similarly, we can define a normalized strain tensor $\bar{\boldsymbol{s}}^{(n,m)}$ [m^{-2}] expressed in terms of the normalized displacement field following Eqs. 2.29-2.34 and Eq. 2.41,

$$\bar{\boldsymbol{S}}^{(n,m)}(r,\phi,t) = B_{n,m}^{(0)} \cdot \bar{\boldsymbol{s}}^{(n,m)}(r,\phi)\, e^{j\Omega t}. \tag{2.43}$$

2.2.1 Radial mode resonances

Mode resonances with $n = 0$ are independent on the azimuthal coordinate. The condition in Eq. 2.39 becomes diagonal, and we can set either the coefficient C_1 or C_2 equal to zero. In this second case, C_1 remains as the only nonzero coefficient and the displacement field becomes purely radial as shown in Eqs. 2.26, 2.27 and 2.28. This family of mode resonances are known as radial mode resonances and they are denoted as $R_{0,m}$, where m is the mode order. Typical form of the characteristic equation of these modes can be obtained from the upper-left element in Eq. 2.39 by applying Bessel function identities [6],

$$\left(1-\alpha^2\right) J_0(\alpha\zeta) - \alpha^2 J_2(\alpha\zeta) = 0. \tag{2.44}$$

The cutoff (or resonance) frequencies $\Omega_{0,m}$ can be obtained by solving numerically this characteristic equation. The cutoff frequencies of the first 20 radial modes for a silica cylinder of radius $a = 62.5$ µm µm are listed on Tab. 2.1. The values of the acoustic velocities for silica assumed in this calculation were $V_L = 5996\,\mathrm{m/s}$ and $V_S = 3740\,\mathrm{m/s}$.

Although the numerical calculation of the frequencies is not cumbersome, in certain situations it is convenient to have a simple expression that allows obtaining the frequencies in an analytical way. For example, when fitting experimental data to the characteristic equation 2.44 is required. To solve this, we derived analytical asymptotic expression for this equation that provide accurate values of the resonance frequencies and also some more physical insight than the numerical calculation. Full derivation of the analytical asymptotic expressions can be found

Table 2.1: Cutoff frequencies for the $R_{0,m}$ mode resonances (from $m = 1$ to $m = 20$) for a silica cylinder of radius $a = 62.5$ µm.

m	$\Omega_{0,m}/2\pi$ (MHz)	m	$\Omega_{0,m}/2\pi$ (MHz)
1	30.52	11	515.36
2	82.06	12	563.35
3	130.74	13	611.34
4	179.03	14	659.33
5	227.18	15	707.31
6	275.26	16	755.29
7	323.31	17	803.27
8	371.34	18	851.25
9	419.36	19	899.23
10	467.36	20	947.21

in Appendix A. Cutoff frequencies of $R_{0,m}$ resonances can be approximated by,

$$\Omega_{0,m} \approx \frac{V_L}{a}\left(c_m - \frac{16\alpha^2 - 1}{8c_m}\right), \tag{2.45}$$

where $c_m = m\pi - \pi/4$. Eq. 2.45 contains a linear term with the mode order m and a term which is inversely proportional to m that becomes small for higher orders. In addition, the frequencies of the radial resonances depend mainly on the longitudinal velocity V_L, divided by the radius of the cylinder a. The relative error made by this approximation decreases fast with the mode order, reaching values of 10^{-3} for $m \geq 2$, as shown in Fig. A.1 in Appendix A.

The normalized displacement vector $\mathbf{u}^{(0,m)}(r)$ for the $R_{0,m}$ modes is given by,

$$\mathbf{u}^{(0,m)}(r) = u_r^{(0,m)}(r)\,\hat{\mathbf{r}}, \tag{2.46}$$

$$u_r^{(0,m)}(r) = \frac{J_1\left(\frac{\Omega}{V_L}r\right)}{\sqrt{2\pi\int_0^a \left[J_1\left(\frac{\Omega}{V_L}r\right)\right]^2 r dr}}, \tag{2.47}$$

The calculated normalized displacement field and intensity for the $R_{0,3}$ and $R_{0,5}$

resonances of a silica optical fiber are shown in Fig. 2.4(a)-(b). As it can be seen, the order of the resonance indicates the number of nodes along the radial coordinate of the fiber. Following Eq. 2.43 and Eqs. 2.29-2.34, the nonzero components of the normalized strain tensor are $s_{rr}^{(0,m)}$ and $s_{\phi\phi}^{(0,m)}$, which are given by,

$$s_{rr}^{(0,m)}(r) = \frac{\partial u_r^{(0,m)}(r)}{\partial r}, \tag{2.48}$$

$$s_{\phi\phi}^{(0,m)(r)} = \frac{u_r^{(0,m)}(r)}{r}. \tag{2.49}$$

Figures 2.4(c)-(d) shows the radial profile of $s_{rr}^{(0,m)}$ and $s_{\phi\phi}^{(0,m)}$ for the $R_{0,3}$ and $R_{0,5}$ resonances. The absolute value of the strain is maximum at the core of the fiber, and at $r = a$, although small, it is nonzero.

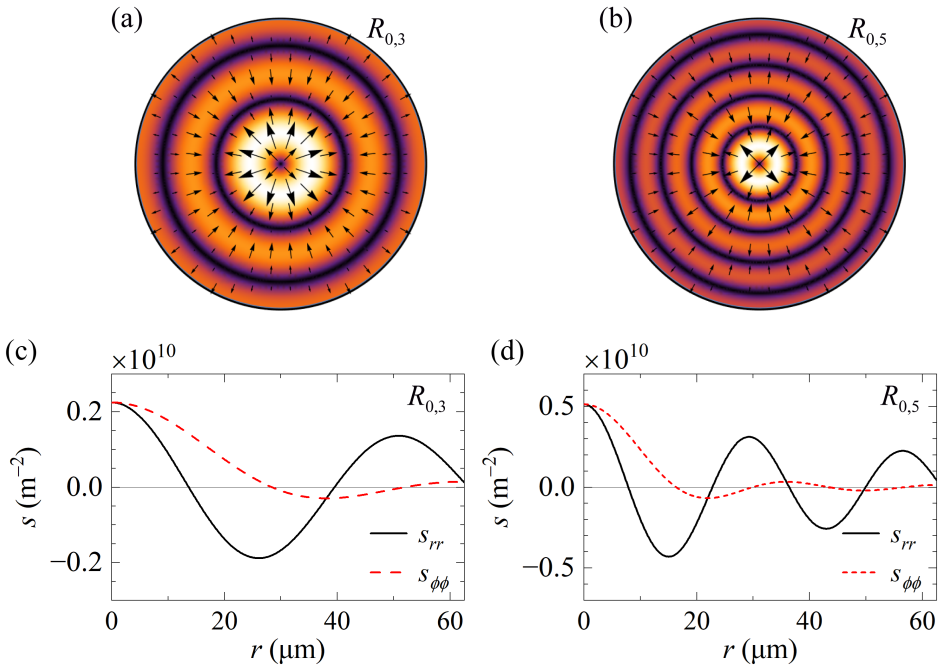

Figure 2.4: (a)-(b) Normalized displacement field $\mathbf{u}^{(0,m)}$ (arrows) and intensity $|\mathbf{u}^{(0,m)}|^2$ (white represents maximum value, black is zero) of resonances $R_{0,3}$ and $R_{0,5}$. (c)-(d) Radial profile of normalized strain components $s_{rr}^{(0,m)}$ and $s_{\phi\phi}^{(0,m)}$ of resonances $R_{0,3}$ and $R_{0,5}$.

2.2.2 Torsional-radial mode resonances

In the case of $n = 2$, the four elements of Eq. 2.39 are in general different from zero, with both coefficients C_1 and C_2 different from zero. This corresponds to torsional-radial acoustic resonances denoted as $TR_{2,m}$. The displacement field of this resonances contains the radial and the azimuthal components, which depend on both the radial and the azimuthal coordinates. The solutions to the condition 2.39 are degenerated due to the two different sets of trigonometric functions in 2.26 and 2.27, which describe the same fields but one rotated by 45º with respect to the other. The characteristic equation for the cutoff frequencies of $TR_{2,m}$ resonances is obtained by setting to zero the determinant of the coefficient matrix in Eq. 2.39. After some manipulations,

$$\begin{vmatrix} \left(3-\zeta^2/2\right)J_2(\alpha\zeta) & \left(6-\zeta^2/2\right)J_2(\zeta)-3\zeta J_3(\zeta) \\ J_2(\alpha\zeta)-\alpha\zeta J_3(\alpha\zeta) & \left(2-\zeta^2/2\right)J_2(\zeta)+\zeta J_3(\zeta) \end{vmatrix} = 0. \tag{2.50}$$

We also derived asymptotic expressions to calculate analytically the cutoff frequencies of torsional-radial resonances. In this case, further approximations must be made in order to obtain simple expressions. A detailed explanation of the asymptotic analysis can be found at Appendix A. This analysis allowed us to conclude that within the series of $TR_{2,m}$ modes, we can differentiate two subgroups of modes denoted as $TR^{(1)}_{2,m}$ and $TR^{(2)}_{2,m}$, each subgroup formed by modes with analogous properties, and different from the modes of the other. For each of these subgroups, we have obtained a different asymptotic expression for the cutoff frequencies,

$$\Omega^{(1)}_{2,m} \approx \frac{V_S}{a}\left(c_{m+1}-\frac{15}{8c_{m+1}}\right), \tag{2.51}$$

$$\Omega^{(2)}_{2,m} \approx \frac{V_L}{a}\left(c_{m+1}-\frac{15}{8c_{m+1}}\right). \tag{2.52}$$

The cutoff frequencies for the first series, $TR^{(1)}_{2,m}$, depend mainly on the shear acoustic velocity V_S. For the second series, $TR^{(2)}_{2,m}$, they depend on the longitudinal velocity V_L as the purely radial modes. This makes the $TR^{(2)}_{2,m}$ and $R_{0,m}$

Table 2.2: Cutoff frequency of $TR^{(1)}_{2,m}$ and $TR^{(1)}_{2,m}$ resonances for a silica cylinder of radius $a = 62.5$ µm.

m	$\Omega^{(1)}_{2,m}/2\pi$ (MHz)	m	$\Omega^{(1)}_{2,m}/2\pi$ (MHz)	m	$\Omega^{(2)}_{2,m}/2\pi$ (MHz)	m	$\Omega^{(2)}_{2,m}/2\pi$ (MHz)
1	39.46	9	290.55	1	70.72	9	466.23
2	81.65	10	322.51	2	126.81	10	514.46
3	108.45	11	350.53	3	176.91	11	560.19
4	139.97	12	380.63	4	224.68	12	610.56
5	169.29	13	410.45	5	273.59	13	658.65
6	200.19	14	440.53	6	319.88	14	706.58
7	230.77	15	470.63	7	370.03	15	754.68
8	260.33	16	500.43	8	418.32	16	802.76

resonances quasi-degenerated. Using these asymptotic expressions, we can identify which exact solutions of Eq. 2.50 correspond to each series. The cutoff frequency of the first 16 modes of both series of an optical fiber calculated numerically by solving Eq. 2.50 are listed on Tab. 2.2. We can comment that the relative error between frequency values given by the numerical calculation from Eq. 2.50, and values given by the asymptotic analytical expressions 2.51 and 2.52 also decreases as the mode order increases, as shown in Fig. A.2 in Appendix A.

The normalized displacement components $\mathbf{u}^{(2,m)}(r,\phi)$ is given by [6],

$$\mathbf{u}^{(2,m)}(r,\phi) = u_r^{(2,m)}(r)\left\{\begin{smallmatrix}\cos(2\phi)\\ \sin(2\phi)\end{smallmatrix}\right\}\hat{\mathbf{r}} + u_\phi^{(2,m)}(r)\left\{\begin{smallmatrix}-\sin(2\phi)\\ \cos(2\phi)\end{smallmatrix}\right\}\hat{\boldsymbol{\phi}}, \tag{2.53}$$

$$u_r^{(2,m)}(r) = \tfrac{1}{\mathscr{N}}\left[\gamma_1 \tfrac{2}{r} J_2\left(\tfrac{\Omega}{V_S} r\right) + \gamma_2 \tfrac{\Omega}{V_L} J_2'\left(\tfrac{\Omega}{V_L} r\right)\right], \tag{2.54}$$

$$u_\phi^{(2,m)}(r) = \tfrac{1}{\mathscr{N}}\left[\gamma_2 \tfrac{2}{r} J_2\left(\tfrac{\Omega}{V_L} r\right) + \gamma_1 \tfrac{\Omega}{V_S} J_2'\left(\tfrac{\Omega}{V_S} r\right)\right], \tag{2.55}$$

$$\gamma_1 = \left[6 - \left(\tfrac{\Omega a}{V_S}\right)^2\right] J_2\left(\tfrac{\Omega a}{V_L}\right), \tag{2.56}$$

$$\gamma_2 = \left[6 - \tfrac{1}{2}\left(\tfrac{\Omega a}{V_S}\right)^2\right] J_2\left(\tfrac{\Omega a}{V_S}\right) - 3\left(\tfrac{\Omega a}{V_S}\right) J_3\left(\tfrac{\Omega a}{V_S}\right), \tag{2.57}$$

where $\mathcal{N}$ is the normalization constant so that $\int_0^a \int_0^{2\pi} |\mathbf{u}^{(2,m)}|^2 r dr d\phi = 1$. The normalized displacement fields and intensity of different modes of both series of torsional-radial resonances are shown in Figure 2.5(a)-(d). As can be seen, the displacement vector of modes of the first series is predominantly azimuthal, whereas for modes of the second series, it is mainly radial. Such behavior is more evident for high order modes. The nonzero components of the normalized strain tensor for $TR_{2,m}$ resonances are given by,

$$s_{rr}^{(2,m)}(r,\phi) = \frac{\partial u_r^{(2,m)}(r)}{\partial r} \left\{ \begin{matrix} \cos(2\phi) \\ \sin(2\phi) \end{matrix} \right\} \tag{2.58}$$

$$s_{\phi\phi}^{(2,m)}(r,\phi) = \frac{1}{r} \left[u_r^{(2,m)}(r) - \frac{\partial u_\phi^{(2,m)}(r)}{\partial \phi} \right] \left\{ \begin{matrix} \cos(2\phi) \\ \sin(2\phi) \end{matrix} \right\} \tag{2.59}$$

$$s_{r\phi}^{(2,m)}(r,\phi) = \frac{1}{2} \left[\frac{1}{r} \frac{\partial u_r^{(2,m)}(r)}{\partial \phi} + \frac{\partial u_\phi^{(2,m)}(r)}{\partial r} - \frac{u_\phi^{(2,m)}(r)}{r} \right] \left\{ \begin{matrix} -\sin(2\phi) \\ \cos(2\phi) \end{matrix} \right\}. \tag{2.60}$$

Figures 2.5(e)-(f) shows the radial profile of $s_{rr}^{(2,m)}$, $s_{\phi\phi}^{(2,m)}$ and $s_{r\phi}^{(2,m)}$ for the $TR_{2,3}^{(1)}$, $TR_{2,8}^{(1)}$, $TR_{2,3}^{(2)}$ and $TR_{2,8}^{(2)}$ resonances. Calculations using the upper set of trigonometric functions were done at $\phi = 0$ for s_{rr} and $s_{\phi\phi}$, while for $s_{r\phi}$ were done at $\phi = \pi/4$.

2.2.3 Acoustic dissipation

In Eq. 2.5 we assumed a lossless medium. In a realistic solid media, the acoustic dissipation is given by a fourth order viscosity tensor η_{ijkl}. Here we will take a simpler approach adding a frequency dependent scalar parameter $\Gamma(\Omega)$ to the differential equation [7],

$$V_L^2 \nabla(\nabla \cdot \mathbf{U}) - V_S^2 \nabla \times (\nabla \times \mathbf{U}) - \Gamma(\Omega) \frac{\partial \mathbf{U}}{\partial t} - \frac{\partial^2 \mathbf{U}}{\partial t^2} = 0. \tag{2.61}$$

This damping parameter accounts for the linewidths of the acoustic resonances. In general, the variation of Γ with the frequency is slow. In our experimental con-

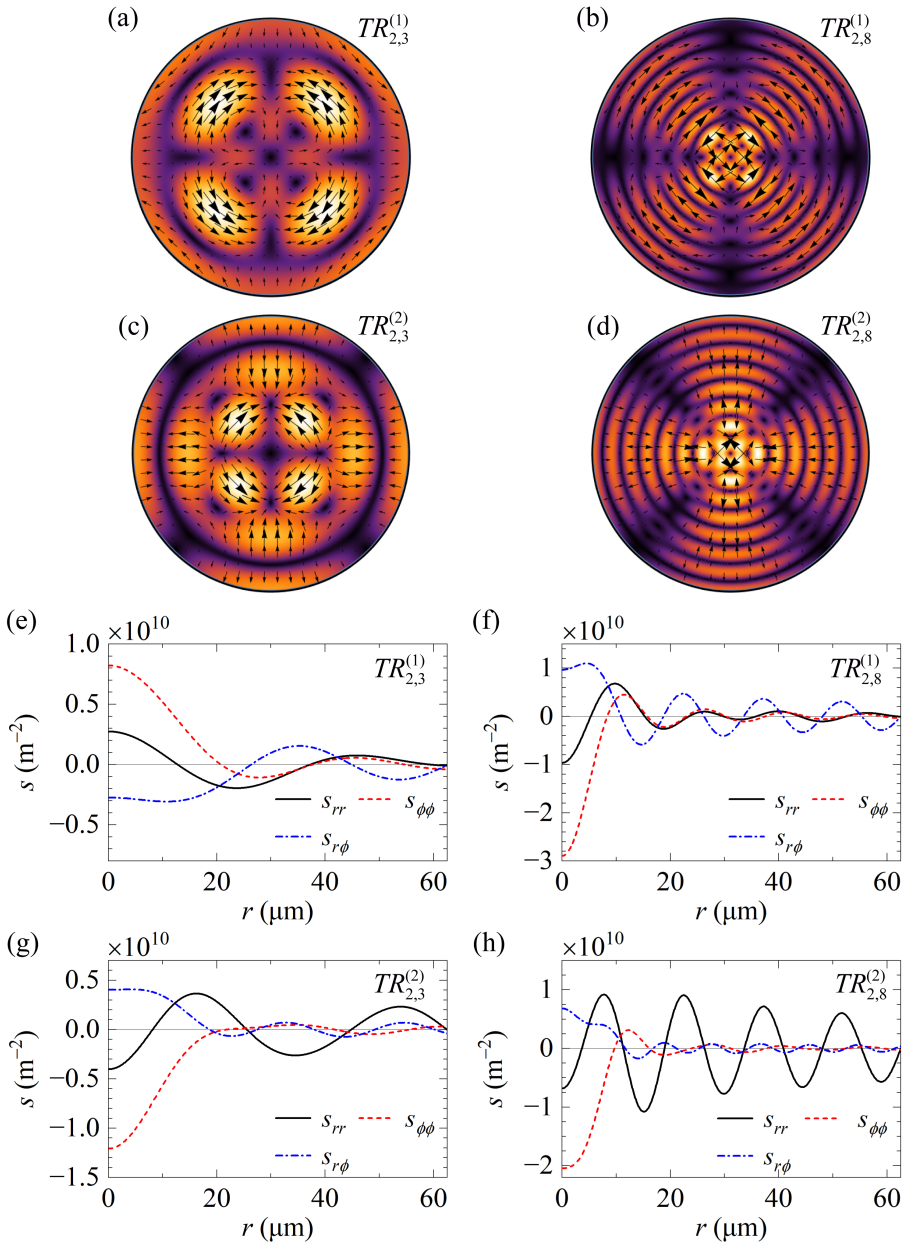

Figure 2.5: Normalized displacement field $\mathbf{u}^{(2,m)}$ (arrows) and intensity $|\mathbf{u}^{(2,m)}|^2$ (white represents maximum value, black is zero) of resonances $TR^{(1)}_{2,3}$, $TR^{(1)}_{2,8}$, $TR^{(2)}_{2,3}$ and $TR^{(2)}_{2,8}$. (e)-(h) Radial profile of normalized strain components $s^{(2,m)}_{rr}$, $s^{(2,m)}_{\phi\phi}$ and $s^{(2,m)}_{r\phi}$ of the same resonances.

ditions the measured linewidths for TAMRs are in the range of tens-to-hundreds of kHz, so $\Gamma(\Omega) \ll \Omega_{n,m}$, then, within a resonance it can be taken as a constant, thus $\Gamma(\Omega)$ can be replaced by a constant modal linewidth $\Gamma(\Omega_{n,m}) = \Gamma_{n,m}$ for each resonance.

In optical fibers, linewidth broadening of acoustic resonances is mainly due to three factors: surface damping, inhomogeneities of the fiber, and viscous damping [8],

$$\Gamma_{n,m} = \Gamma^{sur}_{n,m} + \Gamma^{inh}_{n,m} + \Gamma^{vis}_{n,m}. \tag{2.62}$$

Surface damping arises from the difference in acoustic impedances between the resonator medium and the surroundings: the larger the impedance difference, the larger the reflection coefficient at the boundary. The linewidth broadening due to this effect can be estimated through the following expression [9],

$$\Gamma^{sur}_{n,m} = \frac{\Gamma_i}{\pi} \ln\left(\left|\frac{Z_s + Z_r}{Z_s - Z_r}\right|\right), \tag{2.63}$$

where Z_s and Z_r are the acoustic impedances for the surrounding and resonator media, respectively, and Γ_i is the average frequency separation between a given resonance of order m and its two adjacent resonances $m+1$ and $m-1$. For a typical silica optical fiber stripped of its polymeric coating and surrounded by air, we have that $Z_r = 13.1 \times 10^6$ kg $\cdot$ m$^{-2} \cdot$ s^{-1} and $Z_s = 409.4$ kg $\cdot$ m$^{-2} \cdot$ s^{-1}. Radial mode resonances $R_{0,m}$ in an optical fiber of radius $a = 62.5$ µm are quasi-evenly spaced by $\Gamma_i \approx 2\pi \times 47.5$ MHz, yielding a linewidth broadening of approximately 1 kHz for all the resonances.

Diameter fluctuations of the radius of the resonator along its axis also widen the linewidth of observed TAMRs. Techniques for measuring TAMRs in optical fibers typically require fiber segments that can range from a few centimeters to several kilometers. The experiments exhibited in this thesis were performed with fiber segments of ten centimeters or less, so we will focus on the broadening generated by fiber inhomogeneities in segments of these dimensions. In sections of such a length of conventional single-mode fibers, the diameter fluctuations are

in the order of a few nanometers [10]. For small changes of fiber radius Δa, the attenuation can be approximated by [8],

$$\frac{\Gamma^{inh}_{n,m}}{\Omega_{n,m}} \approx \frac{\Delta a}{a}. \tag{2.64}$$

Assuming a value of $\Delta a = 5$ nm, the linewidth broadening for the $R_{0,m}$ resonances due to this fluctuation ranges from 2.4 kHz for the $m = 1$ resonance to 71 kHz for the $m = 20$. Figure 2.6 shows Γ^{inh} up to 1 GHz for an optical fiber with a radius fluctuation of this magnitude.

Finally, linewidth broadening due to intrinsic viscous damping can be estimated from the attenuation coefficient α_μ of the material [5],

$$\Gamma^{vis}_{n,m} \approx \frac{2 \times 10^6}{8.7} \alpha_\mu (\mathrm{dB/\mu s}). \tag{2.65}$$

In general, the attenuation coefficient depends on the material, the type of wave propagation and, in the case of crystalline materials, of the propagation direction. Fused silica shows different attenuation coefficients for longitudinal and shear

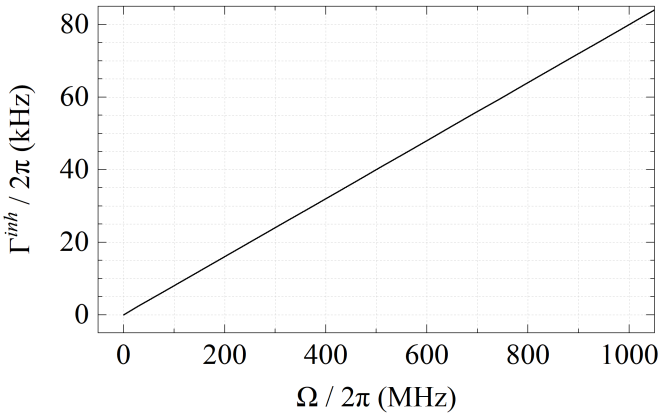

Figure 2.6: Linewidth broadening produced by fiber radius inhomogeneities of acoustic resonances in a conventional optical fiber for a radius fluctuation of $\Delta a = 5$ nm.

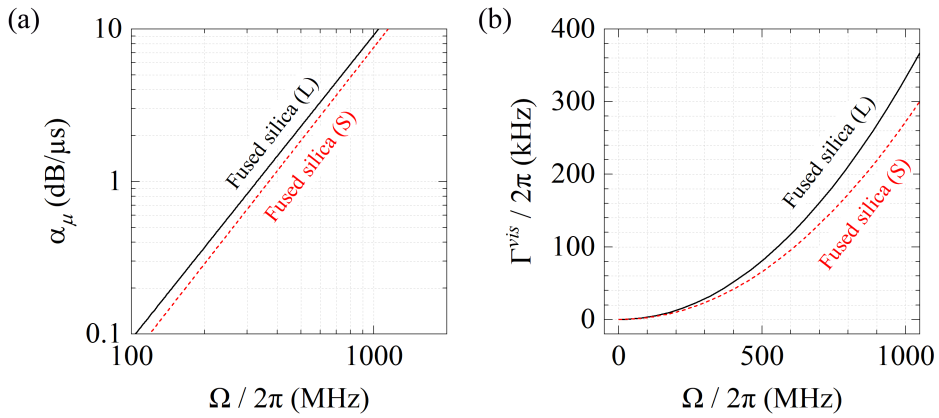

Figure 2.7: (a) Attenuation of longitudinal (L) and shear (S) acoustic waves in fused silica, extracted from [5]. (b) Viscosity contribution to linewidth broadening of longitudinal and shear acoustic waves in silica.

waves, as shown in Fig. 2.7(a). The calculated linewidth broadening due to viscosity for longitudinal and shear acoustic waves is plotted in Fig. 2.7(b). For example, the broadening due to viscosity of radial resonance $m = 1$ and $m = 20$ are 0.3 kHz and 289 kHz, respectively.

2.3 Optical generation of TAMRs in optical fibers

Electrostriction is a property of dielectric media that causes a mechanical deformation under the application of an electric field. From a microscopic point of view, the positive and negative charges of the atoms are displaced in opposite directions as a consequence of the field. This displacement accumulates though the bulk material and generates elongation along the direction of the electric field. Unlike piezoelectricity, reversing the field does not change the direction of the strain. In optical fibers, electrostriction appears when an electromagnetic wave propagates through them. Although in silica it is a relatively weak effect, the small core in optical fibers allows the electric fields to be large enough for this phenomenon to be considered. As it is shown in this section, transverse acoustic mode resonances can be excited by an electromagnetic wave propagating along

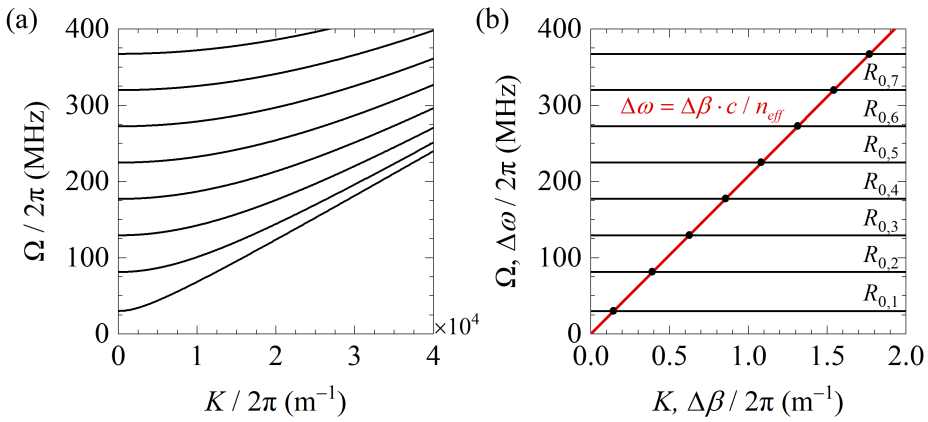

Figure 2.8: (a) Dispersion relations of radial acoustic modes for a silica optical fiber of radius $a = 62.5$ µm. (b) Dispersion relations for small wavenumber/propagation constant for radial acoustic (black) and optical (red) modes.

the fiber via electrostriction. This interaction can be seen as a scattering process in which two co-propagating optical waves with frequencies $\omega_{1,2} = \omega_p \pm \frac{1}{2}\Omega$ couple to an acoustic wave with frequency Ω. This scattering process is commonly known as forward Brillouin scattering (FBS) and is used to describe both the generation of TAMRs by an optical pumping wave and the phase modulation experienced by a probe wave [6–8]. Phase-matching between the optical and acoustic waves is achieved close to the cutoff frequency of TAMRs: for small axial wavenumber, TAMRs axial group velocity tends to zero and the axial phase velocity can reach values equal to those of the optical wave (see Fig. 2.8). Therefore, the wavenumber K of the excited acoustic wave is close to zero and very little energy is guided along the waveguide. For example, for an optical wave at $\lambda_p = \frac{2\pi c}{\omega_p} = 1550$ nm propagating in a single-mode optical fiber, the acoustic wavelengths for the excited resonances $R_{0,1}$ and $R_{0,10}$ are 6.8 m and 44.3 cm, respectively.

Let's consider two continuous and monochromatic optical waves with frequencies ω_1 and ω_2 propagating in a single-mode optical fiber with propagation factors β_1 and β_2 along the z direction. In the weak-guidance approximation, the electric field of the fundamental mode LP_{01} is almost entirely transverse and can

be expressed, in Cartesian coordinates, as,

$$\mathbf{E}_{1,2}(x,y,z,t) = \mathbf{A}_{1,2}(z) \cdot E_T(x,y) \cdot e^{j(\omega_{1,2}\, t - \beta_{1,2}\, z)}, \tag{2.66}$$

where $\mathbf{A}_{1,2}$ [V] are the complex vector amplitudes of the electric fields and E_T [m^{-1}] is the transverse profile of the fundamental optical mode. This transverse profile is normalized such that $\int\int |E_T(x,y)|^2 dx\, dy = 1$. For a single-mode fiber, we can approximate it by a Gaussian radial distribution:

$$E_T(x,y) = \frac{1}{\sqrt{\pi} w} e^{-\frac{x^2+y^2}{2w^2}}, \tag{2.67}$$

where $w = d_{MFD}/(2\sqrt{2})$ is the Gaussian beam radius and d_{MFD} is the mode field diameter [11].

The differential elastic equation of motion in the presence of an external driving force is [12],

$$V_L^2\, \nabla(\nabla \cdot \mathbf{U}) - V_S^2\, \nabla \times (\nabla \times \mathbf{U}) - \Gamma(\Omega) \frac{\partial \mathbf{U}}{\partial t} - \frac{\partial^2 \mathbf{U}}{\partial t^2} = \frac{\mathbf{F^{str}}}{\rho_0}, \tag{2.68}$$

where $F_i^{str} = -\sum_j (\partial T_{ij}^{str}/\partial x_j)$ is the force per unit volume. The electrostrictive stress tensor T_{ij}^{str} [$\mathrm{N/m^2}$] generated by the two optical waves will contain terms oscillating at the frequency $\Omega = \omega_1 - \omega_2$ and propagating along the fiber axis with a propagation constant $K = \beta_1 - \beta_2$. In general, the electrostrictive tensor is related to the optical fields as $T_{ij}^{str} = -\frac{1}{4}\varepsilon_0 n^4 \sum_{kl} [p_{ijkl}(E_{1k}E_{2l}^* + E_{1l}E_{2k}^*)]$, where p_{ijkl} are the strain-optic coefficients. For a single-mode silica optical fiber, taking the fields from Eq. 2.66, the non-zero components of the electrostrictive stress tensor are,

$$T_{xx}^{str} = -\frac{1}{2}\varepsilon_0 n^4 E_T^2(x,y) \left[p_{11} A_{1x}(z) A_{2x}^*(z) + p_{12} A_{1y}(z) A_{2y}^*(z)\right] e^{j(\Omega t - Kz)}, \tag{2.69}$$

$$T_{yy}^{str} = -\frac{1}{2}\varepsilon_0 n^4 E_T^2(x,y) \left[p_{12} A_{1x}(z) A_{2x}^*(z) + p_{11} A_{1y}(z) A_{2y}^*(z)\right] e^{j(\Omega t - Kz)}, \tag{2.70}$$

$$T_{zz}^{str} = -\frac{1}{2}\varepsilon_0 n^4 E_T^2(x,y) \left[p_{12} A_{1x}(z) A_{2x}^*(z) + p_{12} A_{1y}(z) A_{2y}^*(z)\right] e^{j(\Omega t - Kz)}, \tag{2.71}$$

$$T_{xy}^{str} = -\frac{1}{2}\varepsilon_0 n^4 E_T^2(x,y)\left[p_{44}A_{1x}(z)A_{2y}^*(z) + p_{44}A_{1y}(z)A_{2x}^*(z)\right]e^{j(\Omega t - Kz)}, \quad (2.72)$$

where $p_{11} = 0.12$, $p_{12} = 0.27$ and $p_{44} = \frac{1}{2}(p_{11} - p_{12})$ are the strain-optic coefficients of fused silica. It should be noted that the impedance difference and electrostrictive pressure terms at the boundary between the core and the cladding of the fiber are neglected, since the difference in the elastic properties between the two media is minimal.

Depending on the propagation direction of $\mathbf{E}_1$ and $\mathbf{E}_2$, we can distinguish two different interactions. When the two optical waves are counterpropagating, i.e. β_1 and β_2 have opposite signs, the acoustic wavenumber K will be large and the spatial derivatives on z of the electrostrictive tensor will predominate over the transverse derivatives. Therefore, the dominant term $F_z^{str} = -\partial T_{zz}^{str}/\partial z$ will generate acoustic waves with a material displacement in the z axis. This interaction is the origin of backward Brillouin scattering. However, when the two optical waves are copropagating, the acoustic wavenumber K is negligible. As the variations of $A_{1i}(z)A_{2i}^*(z)$ are slow with z (at least several cm in single-mode fibers), the force is dominated by the transverse terms $F_x^{str} = (-\partial T_{xx}^{str}/\partial x - \partial T_{xy}^{str}/\partial y)$ and $F_y^{str} = (-\partial T_{xy}^{str}/\partial x - \partial T_{yy}^{str}/\partial y)$ and will generate acoustic waves with a material displacement in the transverse plane. The latter interaction is behind the excitation of TAMRs. Hence, in the next sections we address only the case of copropagating optical waves, with different polarizations.

2.3.1 Optical waves with aligned linear polarization

Let's assume that both copropagating optical waves are polarized in the $\hat{\mathbf{x}}$ direction and that they are undepleted. We also assume that there is no power exchange between the two optical waves. As the two beams are copolarized, $T_{xy}^{str} = 0$. The transverse forces are given by [12],

$$F_x^{str} = -(a_1 + a_2)\frac{P}{4nc}\frac{\partial E_T^2(x,y)}{\partial x}e^{j(\Omega t - Kz)}, \quad (2.73)$$

$$F_y^{str} = -a_2 \frac{P}{4nc} \frac{\partial E_T^2(x,y)}{\partial y} e^{j(\Omega t - Kz)}, \tag{2.74}$$

where $P = 2nc\varepsilon_0 A_{1x} A_{2x}^*$ [W] is the optical power related to the beating of the two waves, and we have defined the photo-elastic coefficients $a_1 = -n^4(p_{11} - p_{12})$ and $a_2 = -n^4 p_{12}$. We can rewrite the electrostrictive force in cylindrical coordinates,

$$\mathbf{F}^{str}(r,\phi,z,t) = \frac{P}{4nc} [\mathbf{f}_0(r) + \mathbf{f}_2(r,\phi)] e^{j(\Omega t - Kz)}, \tag{2.75}$$

$$\mathbf{f}_0(r) = -(a_1 + 2a_2) \frac{\partial E_T(r)}{\partial r} E_T(r) \hat{\mathbf{r}}, \tag{2.76}$$

$$\mathbf{f}_2(r,\phi) = -a_1 \frac{\partial E_T(r)}{\partial r} E_T(r) [\cos(2\phi)\hat{\mathbf{r}} - \sin(2\phi)\hat{\boldsymbol{\phi}}]. \tag{2.77}$$

The term $\mathbf{f}_0(r)$ is radially symmetric and the direction is purely radial. Such a term leads to the excitation of the $R_{0,m}$ resonances. The term $\mathbf{f}_2(r,\phi)$ depends on both the radial and the azimuthal coordinates, and contains both radial and azimuthal components with a twofold azimuthal symmetry, and leads to the generation of the $TR_{2,m}$ resonances. Figure 2.9 shows both terms at the core of a conventional optical fiber.

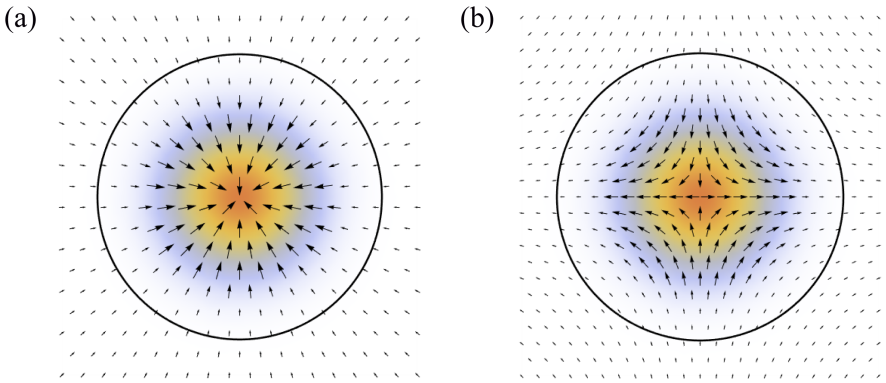

Figure 2.9: Terms of the electrostrictive transverse forces (a) $\mathbf{f}_0(r)$ and (b) $\mathbf{f}_2(r,\phi)$ generated by the fundamental mode (color scheme) in a single-mode optical fiber. The black circumference indicates the core of the fiber.

We can now take the driving electrostrictive force to the wave equation 2.68 and work out the amplitudes $B_{n,m}^{(0)}$ for each one of the TAMRs. As the normalized transverse profiles $\mathbf{u}^{(n,m)}$ form an orthonormal basis [7], we can multiply each side of the wave equation by $(\mathbf{u}^{(n,m)})^{\dagger}$ and integrate over the transverse coordinates to calculate the amplitude of each individual mode,

$$B_{n,m}^{(0)} = \frac{Q_{n,m}^{ES}}{4nc\rho_0} \frac{P}{\Omega_{n,m}^2 - \Omega^2 - j\Omega\Gamma(\Omega)} \approx \frac{Q_{n,m}^{ES}}{4nc\rho_0\Gamma_{n,m}\Omega_{n,m}} \frac{P}{j - 2(\Omega - \Omega_{n,m})/\Gamma_{n,m}}, \tag{2.78}$$

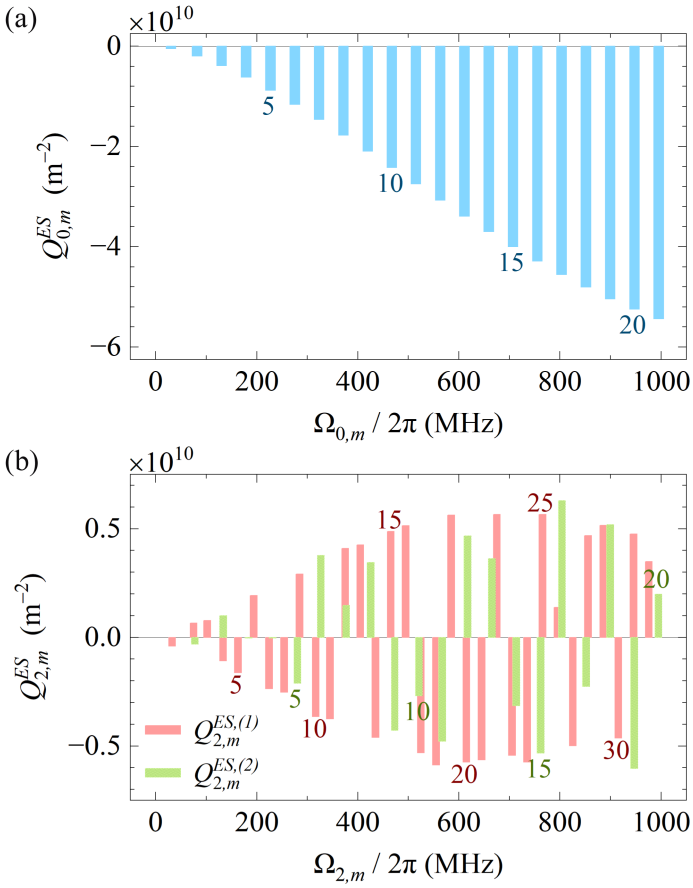

Figure 2.10: Overlap integral $Q_{n,m}^{ES}$ of the electrostrictive force and displacement fields for (a) $R_{0,m}$ resonances, (b) $TR_{2,m}^{(1,2)}$ resonances. The mode field diameter of the pump optical wave was 3.5 µm.

$$Q_{n,m}^{ES} = \int_0^{2\pi} \int_0^a (\mathbf{u}^{(n,m)})^\dagger [\mathbf{f}_0(r) + \mathbf{f}_2(r,\phi)] r dr d\phi. \tag{2.79}$$

The frequency response of the amplitude takes the form of a Lorentzian curve with maximum magnitude at $\Omega = \Omega_{n,m}$. In Eq. 2.78 the acoustic attenuation $\Gamma(\Omega)$ is approximated by the constant modal linewidth $\Gamma_{n,m}$, as discussed in Section 2.2.3. The term $Q_{n,m}^{ES}$ [m^{-2}] denotes the overlap integral between the transverse electrostrictive force generated by the optical pump and the acoustic field. For the $R_{0,m}$ resonances, only the integral with the term $\mathbf{f}_0$ of the electrostrictive force yields a non-zero value, while in the case of the $TR_{2,m}$ resonances, it is $\mathbf{f}_2$ the term that gives a nonzero contribution. Specifically, only the upper set of trigonometric functions in Eqs. 2.54 and 2.55 produces a non-zero value. Thus, despite the angular degeneracy of the $TR_{2,m}$ modes, only one polarization can be excited by this way. Figure 2.10 shows the calculated $Q_{n,m}^{ES}$ for the radial resonances and the two series of torsional-radial resonances in a single-mode optical fiber, for a pump optical wave with a mode field diameter $d_{MFD} = 3.5$ µm, similar to the one used for the experimental results shown in the following chapters.

2.3.2 Optical waves with orthogonal linear polarization

In this scenario, two copropagating optical waves are linearly polarized along the orthogonal directions $\hat{\mathbf{x}}$ and $\hat{\mathbf{y}}$. In this case, the only non-zero component of the electrostrictive stress tensor is T_{xy}^{str} and the forces are given by,

$$F_x^{str} = -a_1 \frac{P(z)}{8nc} \frac{\partial E_T^2(x,y)}{\partial y} e^{j(\Omega t - Kz)}, \tag{2.80}$$

$$F_y^{str} = -a_1 \frac{P(z)}{8nc} \frac{\partial E_T^2(x,y)}{\partial x} e^{j(\Omega t - Kz)}, \tag{2.81}$$

where $P(z) = 2nc\varepsilon_0 A_{1x}(z) A_{2y}^*(z)$. In cylindrical coordinates, the electrostrictive force is:

$$\mathbf{F}^{str}(r,\phi,z,t) = \frac{P(z)}{8nc} \mathbf{f}_{2'}(r,\phi)\, e^{j(\Omega t - Kz)}, \tag{2.82}$$

$$\mathbf{f}_{2'}(r,\phi) = a_1 \frac{\partial E_T(r)}{\partial r} E_T(r) [\sin(2\phi)\hat{\mathbf{r}} + \cos(2\phi)\hat{\boldsymbol{\phi}}]. \tag{2.83}$$

Taking into account the dependence of the force on the azimuthal coordinate ϕ, we can conclude that only $TR_{2,m}$ resonances with the lower set of trigonometric functions (see Eqs. 2.54 and 2.55) can be excited.

2.3.3 Optical waves with circular polarization

For two optical waves with circular polarization, we can distinguish two situations: both waves have the same circular polarization (either right-handed or left-handed), or the two waves have opposite circular polarizations. In the first scenario, and assuming a right-handed circular polarization for both waves, the amplitudes are given by $\mathbf{A}_{1,2}(z) = \frac{A_{1,2}(z)}{\sqrt{2}}(\hat{\mathbf{x}} - j\hat{\mathbf{y}})$. Both T_{xx}^{str} and T_{yy}^{str} will contribute to the electrostrictive force, while $T_{xy}^{str} = 0$. This leads to the following terms of the force,

$$F_x^{str} = -(a_1 + a_2)\frac{P(z)}{8nc}\frac{\partial E_T^2(x,y)}{\partial x}e^{j(\Omega t - Kz)}, \tag{2.84}$$

$$F_y^{str} = -(a_1 + a_2)\frac{P(z)}{8nc}\frac{\partial E_T^2(x,y)}{\partial y}e^{j(\Omega t - Kz)}, \tag{2.85}$$

where $P(z) = 2nc\varepsilon_0 A_1(z)A_2^*(z)$. If we calculate the force components in cylindrical coordinates, we obtain,

$$\mathbf{F}^{str}(r,\phi,z,t) = \frac{P(z)}{8nc}\mathbf{f}_0(r)\,e^{j(\Omega t - Kz)}. \tag{2.86}$$

We can see that the force is only proportional to the term $\mathbf{f}_0(r)$ that was introduced in Section 2.3.1, which is responsible for exciting the radial resonances. Therefore, torsional-radial resonances cannot be generated. The same result is obtained when both optical waves are left-handed circularly polarized.

When the two optical waves are circularly polarized in opposite directions, i.e., $\mathbf{A}_1(z) = \frac{A_1(z)}{\sqrt{2}}(\hat{\mathbf{x}} - j\hat{\mathbf{y}})$ and $\mathbf{A}_2(z) = \frac{A_2(z)}{\sqrt{2}}(\hat{\mathbf{x}} + j\hat{\mathbf{y}})$, the terms of the electrostrictive stress tensor T_{xx}^{str}, T_{yy}^{str} and T_{xy}^{str} contribute to the force. In Cartesian coordinates,

the force is given by,

$$F_x^{str} = -a_1 \frac{P(z)}{8nc} \left[\frac{\partial E_T^2(x,y)}{\partial x} - j \frac{\partial E_T^2(x,y)}{\partial y} \right] e^{j(\Omega t - Kz)}, \tag{2.87}$$

$$F_y^{str} = a_1 \frac{P(z)}{8nc} \left[\frac{\partial E_T^2(x,y)}{\partial y} + j \frac{\partial E_T^2(x,y)}{\partial x} \right] e^{j(\Omega t - Kz)}. \tag{2.88}$$

In cylindrical coordinates,

$$\mathbf{F}^{str}(r,\phi,z,t) = \frac{P(z)}{8nc} [\mathbf{f}_2(r,\phi) + j\,\mathbf{f}_{2'}(r,\phi)]\, e^{j(\Omega t - Kz)}. \tag{2.89}$$

The force is a combination of a term proportional to $\mathbf{f}_2(r,\phi)$ and $\mathbf{f}_{2'}(r,\phi)$, introduced in sections 2.3.1 and 2.3.2, thus, it can lead to the excitation of the two sets of torsional-radial resonances described in Eqs. 2.53-2.57 with a phase difference of $\pi/2$. Purely radial resonances are not stimulated.

2.3.4 Optical pulses

Transverse acoustic mode resonances can be easily excited through relatively intense optical pulses in single-mode optical fibers. Pulses with durations of hundreds of picoseconds and peak powers of several kilowatts may generate an acoustic wave packet that propagates in the transverse direction of the optical fiber comprising several TAMRs with resonance frequency within the pulse's radio-frequency bandwidth. Optical pulses of these durations have a spatial extension of tens of centimeters along the fiber, thus the derivative of the optical field intensity along this axis is much lower than in the transverse direction. Therefore, we can again consider that $F_z^{str} = 0$ and address the problem at any z position in the fiber.

Let $A(t)$ be the local slowly-varying amplitude of an optical pulse linearly polarized along a transverse direction of the fiber. The instantaneous optical power can be defined in the same way as in the previous section as $P(t) = 2nc\varepsilon_0 A(t) A^*(t)$ and its Fourier transform is $\tilde{P}(\Omega) = \frac{1}{2\pi} \int_{-\infty}^{\infty} P(t) e^{j\Omega t} dt$. In the same way, we can express the electrostrictive force and displacement field of TAMRs in the

frequency domain,

$$\tilde{\mathbf{F}}^{str}(r,\phi,\Omega) = \frac{\tilde{P}(\Omega)}{4nc}\left[\mathbf{f}_0(r)+\mathbf{f}_2(r,\phi)\right], \tag{2.90}$$

$$\tilde{\mathbf{U}}(r,\phi,\Omega) = \sum_{n,m}\tilde{B}_{n,m}(\Omega)\cdot\mathbf{u}^{(n,m)}(r,\phi), \tag{2.91}$$

where the amplitude of the modes in the frequency domain is given by,

$$\tilde{B}_{n,m}(\Omega) \approx \frac{Q^{ES}_{n,m}}{4nc\rho_0\Gamma_{n,m}\Omega_{n,m}}\,\frac{\tilde{P}(\Omega)}{j-2(\Omega-\Omega_{n,m})/\Gamma_{n,m}}. \tag{2.92}$$

In these Eqs., $\mathbf{u}^{(n,m)}(r,\phi)$, $\mathbf{f}_0(r)$, $\mathbf{f}_2(r,\phi)$ and $Q^{ES}_{n,m}$ are the same as in the continuous wave scenario. In the frequency domain, the amplitude of each resonance follows a Lorentzian weighted by $\tilde{P}(\Omega)$ and $Q^{ES}_{n,m}$.

In the time-domain, the amplitudes of TAMRs can be obtained by the inverse Fourier transform as $B_{n,m}(t) = \int_{-\infty}^{\infty}\tilde{B}_{n,m}(\Omega)e^{-j\Omega t}d\Omega$. The total displacement field can be expressed in the time-domain as,

$$\mathbf{U}(r,\phi,t) = \sum_{n,m}B_{n,m}(t)\cdot\mathbf{u}^{(n,m)}(r,\phi), \tag{2.93}$$

and

$$B_{n,m}(t) \equiv B^{(0)}_{n,m}\cdot e^{-(\Gamma_{n,m}/2)t}\cdot e^{j\Omega_{n,m}t}\cdot H(t), \tag{2.94}$$

where $H(t)$ is the Heaviside step function. Figure 2.11 shows the amplitudes for the $R_{0,m}$ and $TR_{2,m}$ modes excited by a sech^2 optical pulse with a duration of 700 ps and a peak power of 6 kW in a single-mode fiber with 3.5 μm modal diameter. Linewidths of the different acoustic modes, which are required to evaluate Eq. 2.92, were estimated taking into account all the contributions studied in Section 2.2.3. Although the fields of lower order modes have a poorer overlap with the electrostrictive force, as shown in Fig. 2.10, this is compensated by the radio-frequency spectral components of the pulse (inset in Fig. 2.11) and the lower attenuation losses of these acoustic modes. As a result, in the frequency domain, the peak amplitude of lower order modes is larger when using an optical pulse.

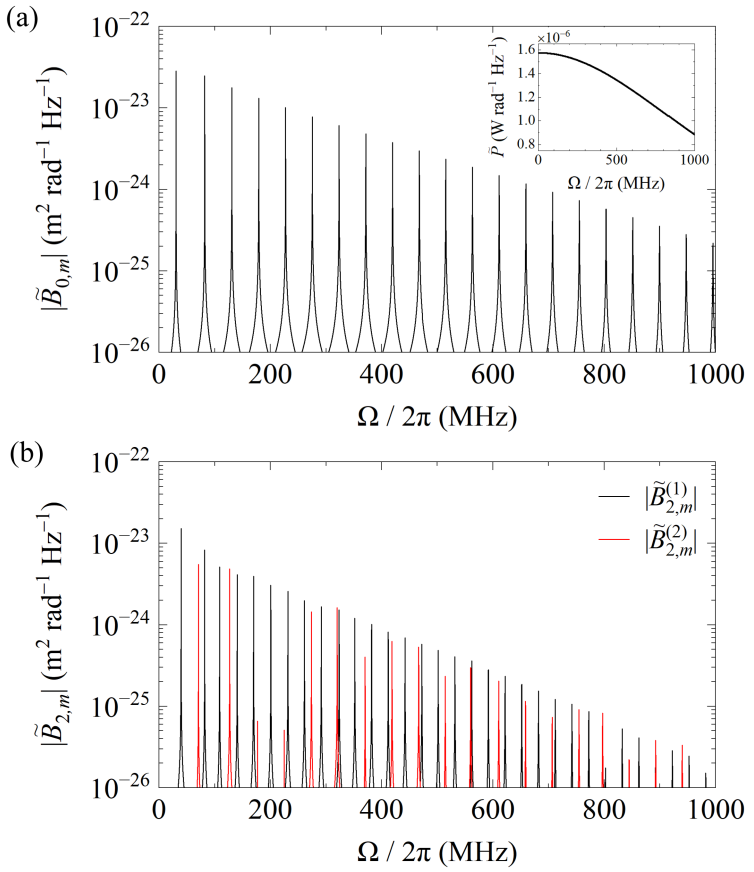

Figure 2.11: Amplitudes (a) $\left|\tilde{B}_{0,m}(\Omega)\right|$ and (b) $\left|\tilde{B}_{2,m}(\Omega)\right|$ for TAMRs generated by a sech^2 optical pulse with time duration of 700 ps, peak power of 6 kW and mode field diameter of 3.5 μm.

For a circularly polarized pulse, the electrostrictive force depends on the transverse coordinates (r,ϕ) as in the case of two waves with the same circular polarization analyzed in Section 2.3.3. Therefore, only the $R_{0,m}$ resonances can be stimulated. By contrast, it is not possible to stimulate only $TR_{2,m}$ resonances with circularly polarized pulses (similarly as depicted in Section 2.3.2), not even by using two orthogonally polarized pulses, since each of them carries spectral components that generates radial resonances.

2.4 Photo-elastic perturbations induced by TAMRs

Photo-elasticity refers to the effect for which the permittivity of a dielectric medium changes when it undergoes a strain. For small mechanical deformations in a solid, the relation between the change in the elements of the dielectric tensor $\bar{\boldsymbol{\varepsilon}}$ and the strain field $\bar{\boldsymbol{S}}$ is given by the strain-optic coefficients p_{ijkl} such that $\Delta\varepsilon_{ij} = -n^4 \sum p_{ijkl} S_{kl}$. It is worth to note that, the strain-optic coefficients are present in both the photo-elasticity and electrostriction phenomena: on the one hand, strain induces a change in the refractive index which results in a change in the stored electrical energy; on the other hand, the stored electrical energy generates a strain in the material.

For an optical fiber, the local perturbation in the dielectric tensor due to the presence of transverse acoustic mode resonances is such that,

$$\Delta\bar{\boldsymbol{\varepsilon}}^{(n,m)} = \begin{pmatrix} \Delta\varepsilon_{rr}^{(n,m)} \\ \Delta\varepsilon_{\phi\phi}^{(n,m)} \\ \Delta\varepsilon_{zz}^{(n,m)} \\ \Delta\varepsilon_{r\phi}^{(n,m)} \\ \Delta\varepsilon_{\phi z}^{(n,m)} \\ \Delta\varepsilon_{rz}^{(n,m)} \end{pmatrix} = -n^4 \begin{pmatrix} p_{11} & p_{12} & p_{12} & & & \\ p_{12} & p_{11} & p_{12} & & & \\ p_{12} & p_{12} & p_{11} & & & \\ & & & p_{44} & & \\ & & & & p_{44} & \\ & & & & & p_{44} \end{pmatrix} \begin{pmatrix} S_{rr}^{(n,m)} \\ S_{\phi\phi}^{(n,m)} \\ 0 \\ 2S_{r\phi}^{(n,m)} \\ 0 \\ 0 \end{pmatrix} \tag{2.95}$$

where the dependence on spatial coordinates and time has been omitted for convenience. Taking into account the strain components of each type of mode, we can conclude that $TR_{2,m}$ resonances lead to nonzero values of four elements, $\Delta\varepsilon_{rr}^{(2,m)}$, $\Delta\varepsilon_{\phi\phi}^{(2,m)}$, $\Delta\varepsilon_{zz}^{(2,m)}$ and $\Delta\varepsilon_{r\phi}^{(2,m)}$, while for the $R_{0,m}$ resonances only the diagonal components $\Delta\varepsilon_{rr}^{(2,m)}$, $\Delta\varepsilon_{\phi\phi}^{(2,m)}$, $\Delta\varepsilon_{zz}^{(2,m)}$ are different from zero. Following Eqs. 2.41 and 2.43, the variation in the dielectric tensor produced by the oscillation of a given TAMR can be expressed in the following way,

$$\Delta\bar{\boldsymbol{\varepsilon}}^{(n,m)}(r,\phi,t) = B_{n,m}^{(0)} \cdot \Delta\bar{\boldsymbol{e}}^{(n,m)}(r,\phi) \cdot e^{j\Omega t}, \tag{2.96}$$

where $\Delta\bar{\boldsymbol{e}}^{(n,m)}$ [m^2] is a normalized magnitude, expressed in terms of the normalized displacement fields $\mathbf{u}^{(n,m)}$. It should be noted that Eq. 2.96 is valid in the case of TAMRs being generated by two optical tones. In the case of TAMRs generated by an optical pulse, the variation in the dielectric tensor can be expressed using the attenuated amplitude $B_{n,m}(t)$ of Eq. 2.94.

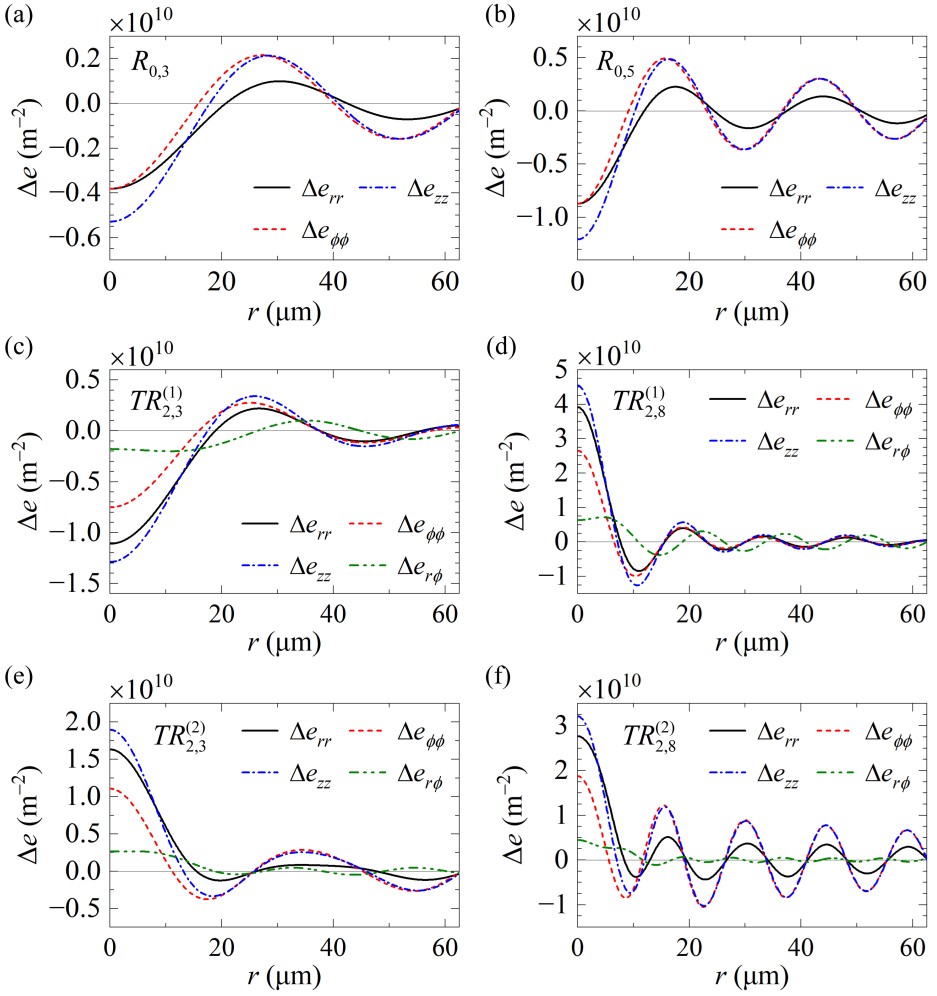

Figure 2.12: Radial profile of normalized variation of dielectric tensor $\Delta\bar{\boldsymbol{e}}^{(n,m)}$ of resonances (a) $R_{0,3}$, (b) $R_{0,5}$, (c) $TR^{(1)}_{2,3}$, (d) $TR^{(1)}_{2,8}$, (e) $TR^{(2)}_{2,3}$ and (f) $TR^{(2)}_{2,8}$.

Fig. 2.12 illustrates the radial dependence of $\Delta\bar{\boldsymbol{e}}^{(n,m)}$ for various TAMRs, calculated using the upper set of trigonometric functions of $TR_{2,m}$ modes at $\phi = 0$ for Δe_{rr} $\Delta e_{\phi\phi}$ and Δe_{zz}, and $\phi = \pi/4$ for $\Delta e_{r\phi}$. It can be observed that the variations in the dielectric tensor reach maximum amplitude at the core of the fiber or close to it, as in some cases of $\Delta e_{r\phi}$. At $r = a$ the dielectric perturbation is very small but non-zero. It should also be noted that, although TAMRs do not contain strain components in the z coordinate, a perturbation in $\Delta\varepsilon_{zz}$ appears due to Eq. 2.95.

2.5 Perturbation of optical fiber modes by TAMRs

The presence of TAMRs in an optical fiber affects the propagation properties of optical guided modes in two different ways. Firstly, the strain field associated with TAMRs induces a perturbation in the refractive index across the optical fiber due to the photo-elastic effect. This perturbation is expressed by the variation of the dielectric tensor, as shown in Eq. 2.95. Secondly, the displacement field of TAMRs introduces changes to the geometry of the fiber, which affects the propagation properties of the guided modes. Both contributions can be addressed in a similar way using perturbation theory [13]. In the first case, the fiber perturbation is given directly by the variation of the dielectric tensor. In the second case, the geometry of the fiber changes, which is equivalent to introducing a change of the refractive profile in the perturbation region.

The electric and magnetic fields of a guided mode in the pristine fiber are given by $\mathbf{E}_0$ and $\mathbf{H}_0$. For a small perturbation of the dielectric tensor given by $\bar{\boldsymbol{\varepsilon}} = \bar{\boldsymbol{\varepsilon}}_0 + \Delta\bar{\boldsymbol{\varepsilon}}$, the propagation factor of the guided wave will change in $\beta = \beta_0 + \Delta\beta$ considering a first-order perturbation. We can also approximate the fields in the presence of perturbation by the original ones, thus we have [13–15],

$$\Delta\beta^{(n,m)} \approx k_0 \sqrt{\frac{\varepsilon_0}{\mu_0}} \frac{\int_S \mathbf{E}_0^* \cdot \Delta\bar{\boldsymbol{\varepsilon}}^{(n,m)} \cdot \mathbf{E}_0 \, dS}{\int_S (\mathbf{E}_0 \times \mathbf{H}_0^* + \mathbf{E}_0^* \times \mathbf{H}_0) \cdot \hat{\mathbf{z}} \, dS}, \tag{2.97}$$

where ε_0 and μ_0 are the dielectric permittivity and magnetic permeability in vacuum, and the surface integral extends over the infinite cross section. In the next

chapter we will discuss this in more detail, applied to specific cases of guided modes.

References

[1] B. A. Auld, *Acoustic fields and waves in solids I*. New York: Wiley, 1973.

[2] J.-C. Beugnot and V. Laude, "Electrostriction and guidance of acoustic phonons in optical fibers", *Phys. Rev. B*, vol. 86, p. 224 304, 2012.

[3] M. Abramowitz and I. A. Stegun, *Handbook of Mathematical Functions with Formulas, Graphs, and Mathematical Tables*. New York: Dover, 1964.

[4] R. N. Thurston, "Elastic waves in rods and clad rods", *The Journal of the Acoustical Society of America*, vol. 64, no. 1, pp. 1–37, 1978.

[5] D. Royer, D. Morgan, and E. Dieulesaint, *Elastic Waves in Solids I: Free and Guided Propagation* (Advanced Texts in Physics). New York: Springer Berlin Heidelberg, 1999.

[6] R. M. Shelby, M. D. Levenson, and P. W. Bayer, "Guided acoustic-wave Brillouin scattering", *Phys. Rev. B*, vol. 31, pp. 5244–5252, 8 1985.

[7] A. S. Biryukov, M. E. Sukharev, and E. M. Dianov, "Excitation of sound waves upon propagation of laser pulses in optical fibres", *Quantum Electronics*, vol. 32, no. 9, pp. 765–775, 2002.

[8] J. Wang, Y. Zhu, R. Zhang, and D. J. Gauthier, "FSBS resonances observed in a standard highly nonlinear fiber", *Optics express*, vol. 19, no. 6, pp. 5339–5349, 2011.

[9] D. M. Chow, Z. Yang, M. A. Soto, and L. Thévenaz, "Distributed forward Brillouin sensor based on local light phase recovery", *Nature communications*, vol. 9, no. 1, pp. 1–9, 2018.

[10] E. P. Alcusa-Sáez, A. Díez, M. González-Herráez, and M. V. Andrés, "Improved time-resolved acousto-optic technique for optical fiber analysis of axial non-uniformities by using edge interrogation", *Optics Express*, vol. 23, no. 6, pp. 7345–7350, 2015.

[11] M. Artiglia, G. Coppa, P. Di Vita, M. Potenza, and A. Sharma, "Mode field diameter measurements in single-mode optical fibers", *Journal of Lightwave Technology*, vol. 7, no. 8, pp. 1139–1152, 1989.

[12] A. Zadok, H. H. Diamandi, Y. London, and G. Bashan, *Forward Brillouin Scattering in Standard Optical Fibers: Single-Mode, Polarization-Maintaining, and Multi-Core* (Springer Series in Optical Sciences). Springer International Publishing, 2022, vol. 240.

[13] A. W. Snyder and J. D. Love, *Optical Waveguide Theory*. Boston, MA: Springer US, 1984.

[14] S. G. Johnson, M. Ibanescu, M. A. Skorobogatiy, O. Weisberg, J. D. Joannopoulos, and Y. Fink, "Perturbation theory for Maxwell's equations with shifting material boundaries", en, *Physical Review E*, vol. 65, no. 6, p. 066 611, 2002.

[15] M. Saadoun and N. Engheta, "Theoretical study of variation of propagation constant in a cylindrical waveguide due to chirality: Chiro-phase shifting", en, *IEEE Transactions on Microwave Theory and Techniques*, vol. 42, no. 9, pp. 1690–1694, 1994.

3 | Novel optical methods for the detection of FBS in optical fibers

In the previous chapter, we studied the theoretical fundamentals of electrostriction and photo-elasticity of forward Brillouin scattering in optical fibers. Most of the FBS detection experiments carried out to date are based on pump and probe techniques, in which TAMRs are generated by an intense optical pulse and the phase modulation in a probe wave is measured. Due to the small scattering efficiencies associated to this interaction, the detection of this phase modulation is not straightforward and usually requires interferometric techniques using tens of meters of fiber.

In this chapter, we will introduce new characterization techniques of FBS in optical fibers developed during the course of this thesis. Following a pump and probe scheme, the mechanical stresses generated in the optical fiber by transverse acoustic mode resonances were converted into an optical power modulation that can be detected using a fast photodetector. We followed two different strategies. The first is based on the use of a fiber device acting as a transducer, in particular, we investigated the use of fiber Bragg gratings and long-period fiber gratings. The second strategy relies on the physical characteristic of an optical fiber of being also an optical microresonator that supports whispering-gallery modes. In this chapter, we describe in detail both methods, showing the different experimental setups used for their implementation, along with the results obtained. A complete discussion of the experimental results and detailed comparative with the theoretical models developed in the thesis is included.

3.1 Fiber diffraction gratings

Optical fibers typically guide light along its axis, due to the slightly higher refractive index of the core (n_{co}) with respect to the cladding (n_{cl}). The electromagnetic fields of modes guided by the fiber are confined around the core area. For single-mode fibers this occurs in a single fundamental mode, with an effective index $n_{co} > n_{eff} > n_{cl}$, known as LP_{01} mode in the approximation of weak guidance. When the fiber is surrounded by a medium with a lower refractive index than the cladding, in addition to the fundamental core mode, a large number of modes whose fields extend across the entire fiber, known as cladding modes, are also supported. Cladding modes have effective refractive indexes that lies between those of the cladding and the surrounding medium.

In a pristine optical fiber, the core mode and the cladding modes are orthogonal and do not exhibit any coupling among themselves in normal conditions due to the different propagation factors and fields' structure. However, a perturbation in the core or cladding may result in a power transfer between different modes. Fiber diffraction gratings, based on periodic perturbations in the refractive index of the core, take advantage of this phenomenon. Fiber gratings are characterized mainly by three parameters: the period of the perturbation Λ, the strength of the index modulation Δn, and the length of the grating L, as shown in Fig. 3.1. Fiber gratings can be classified into two groups according to the magnitude of their period: long-period gratings (LPGs), with periods around tens or hundreds of micrometers; and fiber Bragg gratings (FBGs), with periods around hundreds of nanometers.

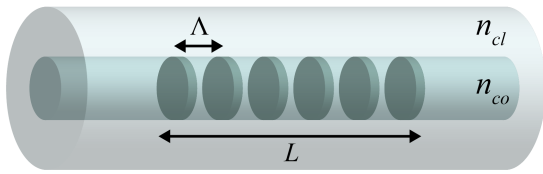

Figure 3.1: Scheme of a fiber diffraction grating.

In single-mode fibers, LPGs are characterized for coupling the fundamental core mode to copropagating cladding modes. In conventional optical fibers, the light coupled to the cladding mode is absorbed by the polymeric jacket. The result is a series of attenuation notches in the transmission spectrum of the fundamental mode. Each notch is located at the optical wavelength at which the core mode and a given cladding mode is coupled. The resonant wavelengths at which this occurs are given by [1],

$$\lambda_{LPG} = (n_{eff,co} - n_{eff,cl})\Lambda, \tag{3.1}$$

where $n_{eff,co}$ and $n_{eff,cl}$ are the effective indexes of the core and the cladding mode, respectively.

The short period of the refractive index modulation in FBGs enables coupling light between the forward-propagating fundamental core mode to the same mode propagating in the backward direction. As a result, FBGs behave as narrowband reflectors. Coupling to counter-propagating cladding modes is also achieved using FBGs [2], however this feature is not significant for this work, thus, we will only focus on the effects given by the coupling between the fundamental mode. For such coupling, the resonance wavelength is given by [1],

$$\lambda_{FBG} = 2\, n_{eff,co}\, \Lambda. \tag{3.2}$$

3.1.1 Interaction of fiber gratings with TAMRs

Due to the transverse nature of TAMRs, diffraction gratings do not experience a change in the period Λ in their presence. Therefore, any change in their resonance wavelength is caused by a variation in the effective indices. The change produced in $n_{eff,cl}$ by the oscillation of a TAMR is much shorter than that produced in $n_{eff,co}$. The origin is the radial distribution of the displacement and strain fields of TAMRs, which leads to stronger perturbation of the refractive index in the fiber core area (see, for example, Figs. 2.5 and 2.12). Thus, in the

following analysis, changes of $n_{eff,cl}$ caused by the TAMR were neglected.

Hence, we will study how TAMRs affect the propagation properties of the fundamental mode and the change in $n_{eff,co}$ that it experiences. As discussed in Section 2.5, the optical fiber, and therefore the propagation factor of the core mode, is perturbed in two ways, through the photo-elastic and the geometrical contributions. Assuming linear polarization along the x axis of the optical fiber, the fields of a LP_{01} mode in the unperturbed fiber are given by [3],

$$\mathbf{E}_0 = E_x\,\hat{\mathbf{x}} = E_{0,T}(x,y)\,e^{j(\omega t-\beta_0 z)}\,\hat{\mathbf{x}}, \tag{3.3}$$

$$\mathbf{H}_0 = H_y\,\hat{\mathbf{y}} = \sqrt{\frac{\varepsilon_0}{\mu_0}}\,n\,E_{0,T}(x,y)\,e^{j(\omega t-\beta_0 z)}\,\hat{\mathbf{y}}, \tag{3.4}$$

where $E_{0,T}$ is the normalized Gaussian transverse profile as expressed in Eq. 2.67.

In the experiments included in this thesis, TAMRs were excited by an optical pump pulse. Therefore, we will focus this study on this particular case. When TAMRs are generated by an optical pulse the total displacement field is given by $\mathbf{U}(r,\phi,t) = \sum_{n,m} B_{n,m}(t)\,\mathbf{u}^{(n,m)}(r,\phi)$, where the amplitudes $B_{n,m}(t)$ are defined in Eq. 2.94.

(I). Photo-elastic contribution

The perturbation in the propagation factor of the fundamental mode given by Eq. 2.97 can be expressed as,

$$\begin{aligned}\Delta\beta^{(n,m)}(t) &\approx k_0\sqrt{\frac{\varepsilon_0}{\mu_0}}\,\frac{\int_S \mathbf{E}_0^*\cdot\Delta\bar{\boldsymbol{\varepsilon}}^{(n,m)}(t)\cdot\mathbf{E}_0\,dS}{\int_S(\mathbf{E}_0\times\mathbf{H}_0^*+\mathbf{E}_0^*\times\mathbf{H}_0)\cdot\hat{\mathbf{z}}\,dS}\\ &\approx \frac{k_0}{2n}\,B_{n,m}(t)\,Q_{n,m}^{PE},\end{aligned} \tag{3.5}$$

where we have taken into account that $\omega = c\,k_0$, $d\beta/d\omega = n_g/c$ where n_g is the group index, and $n_g \approx n$. $Q_{n,m}^{PE}$ [m^{-2}] is the photo-elastic overlap integral and accounts for the efficiency of the photo-elastic perturbation for each TAMR.

It is defined in terms of the normalized magnitude of the dielectric permittivity perturbation $\Delta\bar{\boldsymbol{e}}^{(n,m)}$ as,

$$\begin{aligned} Q_{n,m}^{PE} &\equiv \int_S \mathbf{E}_0^* \cdot \Delta\bar{\boldsymbol{e}}^{(n,m)} \cdot \mathbf{E}_0 \, dS \\ &= \int_S \{\Delta e_{rr}^{(n,m)} |E_r|^2 + \Delta e_{r\phi}^{(n,m)} (E_r E_\phi^* + E_r^* E_\phi) + \Delta e_{\phi\phi}^{(n,m)} \left|E_\phi\right|^2\} \, dS, \end{aligned} \tag{3.6}$$

where $E_r = E_x \cos(\phi)$, $E_\phi = -E_x \sin(\phi)$ are the components of the electric field in cylindrical coordinates. If we express $\Delta\bar{\boldsymbol{e}}^{(n,m)}$ as a function of the normalized displacement field $\mathbf{u}^{(n,m)}$, and after performing the integral over the azimuthal coordinate, we obtain for each family of TAMRs [4],

$$Q_{0,m}^{PE} = \pi(a_1 + 2a_2) \int_0^a \left[\frac{\partial u_r^{(0,m)}}{\partial r} + \frac{u_r^{(0,m)}}{r} \right] |E_{0,T}(r)|^2 \, r \, dr, \tag{3.7}$$

$$Q_{2,m}^{PE} = \frac{\pi}{2} a_1 \int_0^a \left[\frac{\partial u_r^{(2,m)}}{\partial r} + \frac{\partial u_\phi^{(2,m)}}{\partial r} + \frac{u_r^{(2,m)}}{r} + \frac{u_\phi^{(2,m)}}{r} \right] |E_{0,T}(r)|^2 \, r \, dr. \tag{3.8}$$

Figure 3.2 shows the calculated $Q_{n,m}^{PE}$ for the $R_{0,m}$ and $TR_{2,m}$ resonances in a single-mode optical fiber. A mode field diameter of 4.5 µm, which corresponds to the mode field diameter of the fiber at the probe signal wavelength of the experiments, has been used for the calculation. It should be noted that the overlapping integrals $Q_{n,m}^{ES}$ and $Q_{n,m}^{PE}$ are identical [4] when evaluated for optical beams with the same mode field diameter.

(II). Geometrical contribution

For $R_{0,m}$ modes the displacement is given by $U_r^{(0,m)}(r)$, and the geometrical perturbation produced it the fiber core can be depicted as a variation of the core radius [3], whose amplitude δa_{co} is determined by the amplitude of the displacement vector at $r = a_{co}$. Thus, $\delta a_{co}(t) \equiv U_r^{(0,m)}(r,t)|_{r=a_{co}} = B_{0,m}(t)\, u_r^{(0,m)}(r)|_{r=a_{co}}$. Assuming that the perturbed and unperturbed fibers are weakly guiding, and a Gaussian approximation for the fundamental mode, the perturbation in the prop-

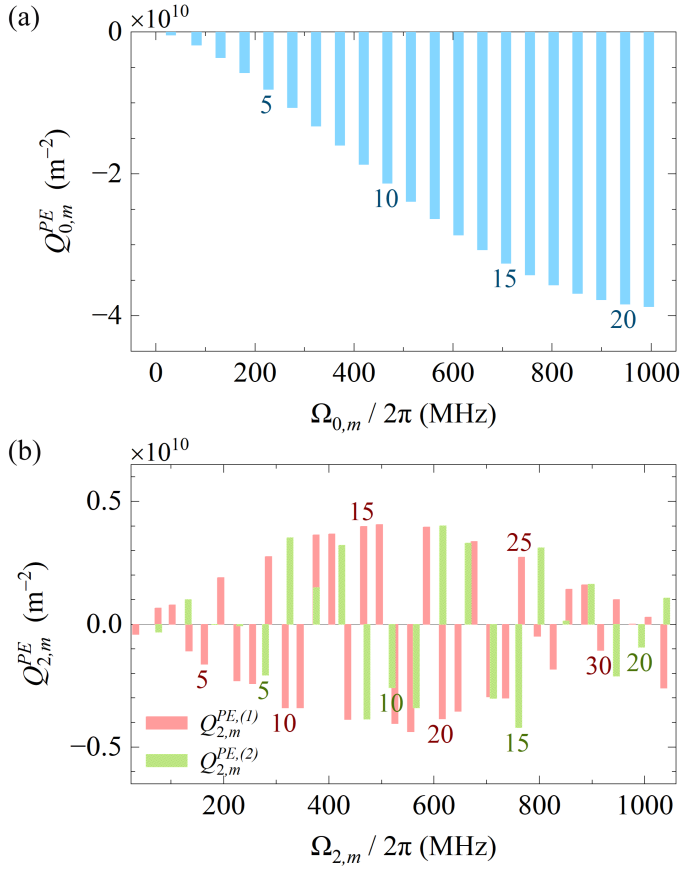

Figure 3.2: Photo-elastic overlap integral $Q^{PE}_{n,m}$ for (a) $R_{0,m}$ resonances, (b) $TR^{(1,2)}_{2,m}$ resonances. The mode field diameter of the probe optical wave was 4.5 µm. The order m of some $R_{0,m}$ / $TR_{2,m}$ modes is indicated.

agation constant of the fundamental mode due to the geometrical contribution of radial modes can be expressed as [3],

$$\Delta\beta^{(0,m)}(t) \approx \frac{\delta a_{co}(t)\log\left(a_{co}\,k_0\,NA\right)^2}{a_{co}^3 k_0 n} = \frac{k_0}{2n}\,B_{0,m}(t)\,Q^{GE}_{0,m}, \tag{3.9}$$

where NA is the numerical aperture of the optical fiber, and we have defined,

$$Q^{GE}_{0,m} = \frac{2u_r^{(n,m)}(a_{co})}{k_0^2\,a_{co}^3}\log\left(a_{co}\,k_0\,NA\right)^2. \tag{3.10}$$

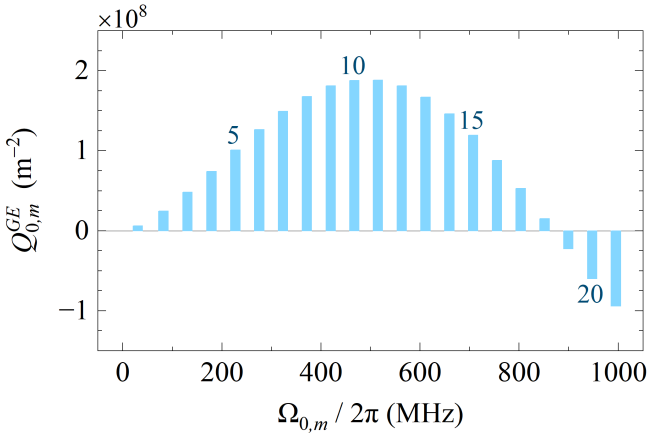

Figure 3.3: Geometrical contribution $Q^{GE}_{0,m}$ for $R_{0,m}$ resonances. The parameters of the calculation were $NA = 0.29$, $a_{co} = 4.2$ µm and $\lambda_{co} = 1.55$. The order m of some $R_{0,m}$ modes is indicated.

Although $Q^{GE}_{0,m}$ [m^{-2}] is not an overlap integral as such, the comparison against $Q^{PE}_{0,m}$ is of interest. Figure 3.3 shows $Q^{GE}_{0,m}$ for $NA = 0.29$, $a_{co} = 4.2$ µm and $\lambda_{co} = 1.55$ µm. It can be observed that $Q^{GE}_{0,m}$ is of opposite sign to that of $Q^{PE}_{0,m}$, except for high order modes. Additionally, $Q^{GE}_{0,m}$ values are two orders of magnitude smaller than $Q^{PE}_{0,m}$ values, so we can conclude that the geometrical contribution can be neglected in this case. For $TR_{2,m}$ modes, the geometrical perturbation is more complex as it introduces anisotropy in the core size by $U_r^{(2,m)}(r,\phi)$. Again, the strength of such perturbation is much smaller than the material perturbation contribution, and then it will not be discussed in this thesis.

3.1.2 Experimental results and discussion

The experimental setup for the pump-and-probe technique used to detect and characterized TAMRs with fiber diffraction gratings is shown in Fig. 3.4. TAMRs were excited through optical electrostriction using pump pulses emitted by a Q-switch microchip laser (TEEM Photonics SNP-20F-100, 700 ps pulse duration, 1064 nm wavelength, 19.9 kHz repetition rate). The inset in Fig. 3.4 shows the temporal profile of the pulses. The pump pulses were delivered into

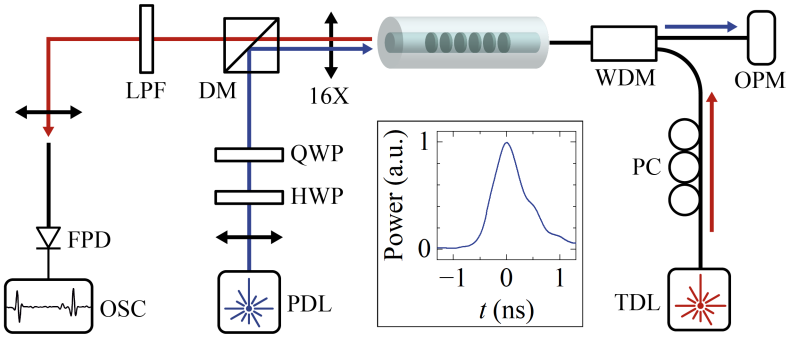

Figure 3.4: Scheme of the experimental setup employed with fiber diffraction gratings. OSC: oscilloscope; FPD: fast photodetector; LPF: long-pass filter; DM: dichroic mirror; PDL: pulsed diode laser (@1064nm); HWP: half-wave plate; QWP: quarter-wave plate; WDM: wavelength division multiplexer; OPM: optical power meter; PC: polarization controller; TDL: tunable continuous wave diode laser (@1550nm); Blue line: pump laser path; Red line: probe laser path. The inset shows the temporal profile of the pump pulse.

the fiber under test (FUT) using a 16x aspheric lens and a 3-axis stage. A half-wave plate and a quarter-wave plate were used to adjust the polarization of the linearly polarized pulses provided by the pump laser. The average pump power was monitored at the output of a wavelength division multiplexer using an optical power meter.

The diffraction gratings were written in the core of the FUT (SM1500-4.2/125, 0.29 NA, Fibercore). The choice of this fiber was due to two reasons: (i) the high concentration of germanium in the core of the fiber enables writing the gratings by UV exposure without hydrogen loading; and (ii) the narrow core generates a great confinement of light, increasing the efficiency of electrostriction. The FUT was stripped from its polymer coating for the writing process and to improve the quality factor of the acoustic resonances. A narrow-linewidth continuous wave tunable laser (Keysight 81940 A) emitting at 1550 nm was used as probe wave to interrogate the transmission of the grating, tuned at one side of the notch.

There are two possible sources of intensity modulation of the probe signal provided by the grating, one due to the local modulation of the fiber grating itself,

and another due to the fiber grating transfer function that converts the accumulated phase modulation of the probe signal in the fiber section prior to the fiber grating into an amplitude-modulated signal [5]. In a pump-and-probe copropagating configuration and for lengths of the order of the acoustic wavelength of TAMRs, the accumulated contribution dominates over the local modulation of the grating due to the existence of phase matching between the acoustic and optical waves. In our experimental setup, the probe laser was delivered into the FUT in a counter-propagating configuration with respect to the pump wave. This configuration allowed to detect only the local perturbation of TAMRs in the grating due to the lack of phase-matching between the probe wave and the acoustic wave. The probe signal was detected using a fast photodetector (Thorlabs DET01CFC) and a 1 GHz bandwidth oscilloscope (Keysight DSOS104A).

(I). Long-period gratings

LPGs are sensitive to changes in both the effective index of the core and the cladding modes. They can be designed to exhibit narrow-band notches with large sensitivities to small changes of the refractive index. The LPG employed in the experiments of this thesis was written in the fiber following the method shown in [6], using a point-by-point technique irradiating the fiber with a UV beam. The polarization controller in Fig. 3.4 was used to adjust the polarization state of the probe laser to one of the principal axis of the LPG, since the residual birefringence of the fiber produces noticeable splitting of the narrow-band LPG spectrum. The period of the LPG was 52.3 μm and its length was 11 cm. Its transmission spectrum along the slow axis of the fiber is shown in Fig. 3.5. The LPG exhibited a notch at 1552 nm with a 3 dB bandwidth of 1.3 nm and a depth of -9 dB.

In the following analysis, we will assume that the major perturbation caused by the TAMRs wave packet affects the core effective index. When the probe laser is tuned to one of the edges of the LPG spectrum, the variation in the transmittance is proportional to the displacement of the resonant wavelength, as long as the

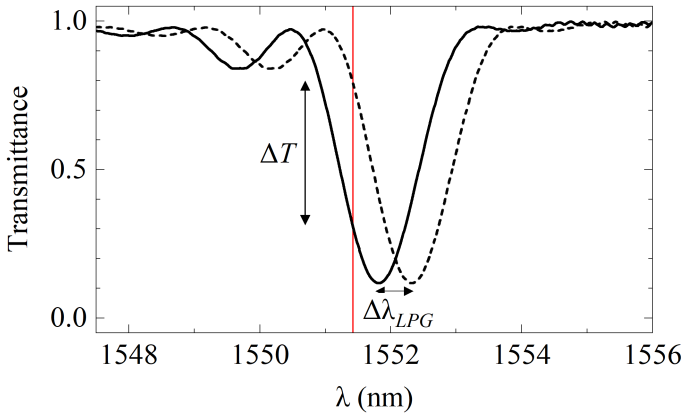

Figure 3.5: LPG transmittance spectrum ($\Lambda = 52.3$ µm, $L = 11$ cm). The operation principle of the detection technique is shown. Dashed line: shifted LPG; red line: wavelength of the probe wave; ΔT: transmittance variation; $\Delta\lambda_{LPG}$: resonant wavelength variation.

perturbation caused by the acoustic waves is small enough to remain in the linear region (Fig. 3.5). Thus, the core effective index change is given by:

$$\Delta n_{eff,co} \approx -\frac{\Delta T}{s\,\Lambda}, \tag{3.11}$$

where s is the slope of notch edges, negative at the left side and positive at the right side. For the LPG whose transmission spectrum is shown in Fig. 3.5, the slopes were -0.98 nm^{-1} and 0.90 nm^{-1}, respectively. Figure 3.6(a) shows the temporal response in the transmittance of the LPG for a probe wave tuned to the left side, and a pump peak power of 7 kW. The trace shows a sequence of oscillations with an amplitude decaying in time due to the combined action of attenuation and dispersion of the acoustic wave packet. The estimated decay time was 780 ns and the period of the pump laser was 50.25 µs, so overlap between consecutive acoustic responses was minimal. The effective core index variation calculated from Eq. 3.11 is also indicated. A zoom of the first 120 ns of the temporal trace is shown in the upper part of Fig. 3.6(b). The polarization of the pump pulses was adjusted to maximize the stimulation of both $R_{0,m}$ and $TR_{2,m}$

resonances. At $t = 0$ we can observe the combined effect on the LPG of the acoustic interaction and the optical nonlinear Kerr effect [7] caused by the pump pulse, which remains while the pump pulse propagates through it. Thereafter, we observe two patterns of periodic beats. The most intense one results from the combination of purely radial resonances $R_{0,m}$ oscillating in phase. These beats are separated by ∼21 ns, corresponding to the round-trip time of an acoustic pulse traveling in the radial direction of the 125 µm diameter silica fiber at the longitudinal acoustic velocity V_L. The second beat pattern corresponds to the oscillation of a packet of torsional-radial resonances $TR_{2,m}$. The periodicity is ∼33 ns, which corresponds to an acoustic pulse traveling in the radial direction of the fiber at the shear acoustic velocity V_S. It is worth to note that no appreciable modulation is observed apart from the two patterns described. This implies that the acoustic wave packet does not affect the transmittance of the LPG as it travels through the cladding of the fiber. Figure 3.6(b) also shows a theoretical calculation of $\Delta n_{eff,co}(t) = \sum \Delta n_{eff,co}^{(n,m)}(t)$ from Eq. 3.5, and considering that $\Delta n_{eff,co} = \Delta\beta/k_0$. The agreement with the experimental result shown in the upper part of Fig. 3.6(b) is remarkable, except at around $t = 0$ since the model does not take into account the Kerr effect.

The radio-frequency (RF) spectrum obtained through fast Fourier transform (FFT) of the temporal trace is shown in 3.6(c). The FFT was performed from $t = 10$ ns to avoid asymmetries in the Lorentzian shape of the resonances due to cross-phase modulation by Kerr nonlinearity [8]. The RF spectrum consists of a series of peaks located at the resonance frequencies of the different TAMRs excited by the pump. Highest intensity peaks correspond to $R_{0,m}$ resonances and they are quasi-evenly spaced by 47.6 MHz, while the secondary peaks located between the radial resonances corresponds to $TR_{2,m}$ resonances. The difference of resonance frequency between the measured acoustic resonances with respect to the theoretical ones from Tabs. 2.1 and 2.2 was in the order of 1%. Such deviation, if nominal values of acoustic velocities are assumed, corresponds to a deviation in the radius of the fiber of ∼0.7 µm, that can be considered to be within the fiber specifications. The excitation efficiency of $TR_{2,m}$ resonances could be

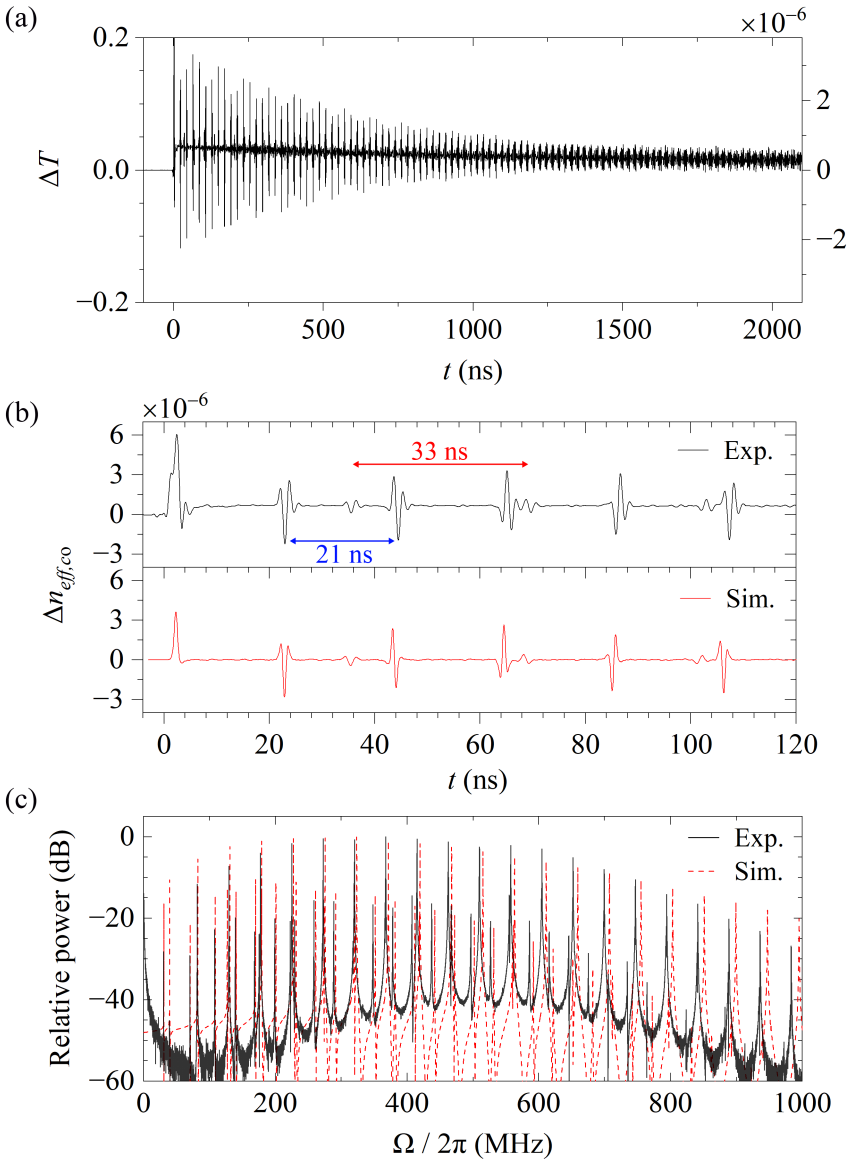

Figure 3.6: (a) Transmittance variation and core effective index modulation of the LPG, after a pump pulse with peak power of 7 kW. The trace was the result of 1064 averages. (b) Experimental and simulated plot of the first 120 ns. (c) Experimental and simulated frequency spectrum of the probe wave obtained through Fourier transform of the temporal trace.

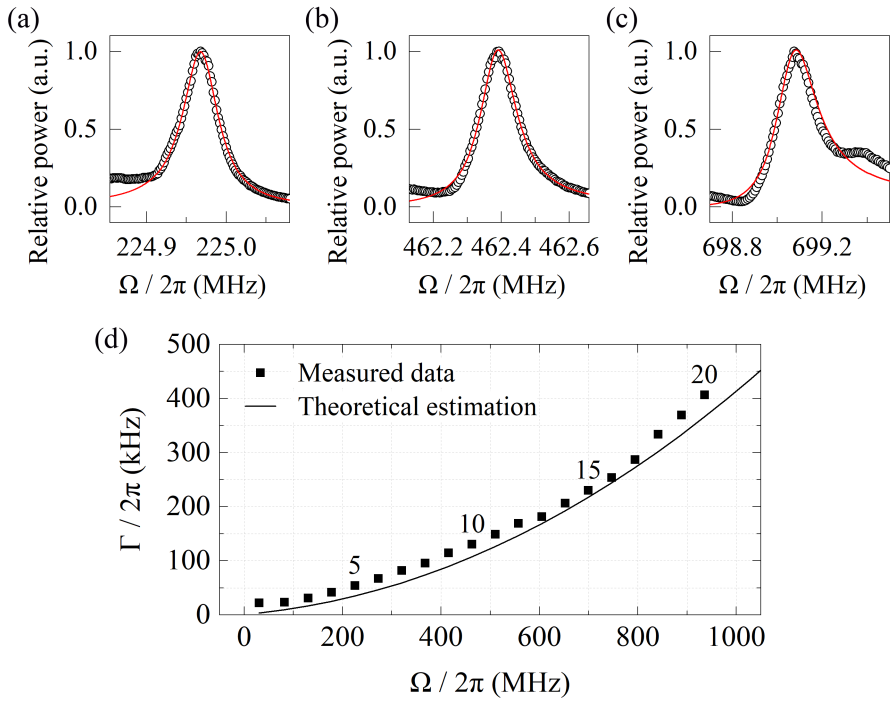

Figure 3.7: RF spectrum corresponding to acoustic resonances (a) $R_{0,5}$, (b) $R_{0,10}$ and (c) $R_{0,15}$; dots: experimental data; red line: Breit-Wigner-Fano fit. (d) Measured linewidth of $R_{0,m}$ resonances and theoretical estimation from Section 2.2.3 for a radius fluctuation of $\Delta a = 5$ nm. The order m of some $R_{0,m}$ modes is indicated.

reduced experimentally by adjusting the polarization of the pump wave. Notice that for a circular polarized pump, excitation of $TR_{2,m}$ modes is not done. With our experimental setup, the amplitude of the $TR_{2,m}$ peaks in the RF spectrum were reduced in more than $\sim$15 dB by adjusting the pump polarization.

High resolution spectra of $R_{0,m}$ resonances were obtained from a signal analyzer (Keysight N9010A) with a resolution bandwidth of 1.8 kHz and a video bandwidth of 18 Hz. Temporal gating was not applied in these measurements, so the resonances exhibited a Fano asymmetry due to interference with Kerr nonlinearities [8]. Full-width half maximum values of radial resonances were obtained from fitting the measured spectrum of each resonance to a Breit-Wigner-Fano

function, as shown in Figs. 3.7(a)-(c). Increasing values of linewidths with the mode number m were obtained with an exponential-like behaviour, ranging from 22.5 kHz for the $R_{0,1}$ resonances to 406.8 kHz for the $R_{0,20}$ one, which translates into quality factors in the range $3-4\times10^3$. Figure 3.7(d) shows the comparison between the measured linewidths with the estimated ones obtained following Section 2.2.3, considering a section of fiber of similar characteristics to the one used in the experiment. Good agreement was observed between the two, with results very close to the theoretical ones. In particular, thanks to the short section of fiber employed, there is a dominant contribution to attenuation due to viscosity over fiber inhomogenities, that can be inferred from the exponential behavior against frequency (see Section 2.2.3). We can compare these results with those obtained in other experiments like [9], where a 100-m long uncoated fiber in air yielded a linewidth of 1.1 MHz for the $R_{0,7}$ resonance ($Q\sim300$); or [10], where a 25-m long uncoated fiber in air resulted in 0.45 MHz for the same resonance ($Q\sim700$).

The dependence of the resonances' amplitude on the input pump power was also studied using neutral density filters. The results for the $R_{0,10}$ resonance are shown in Fig. 3.8(a). Similar results were obtained for other modes. A linear dependence was found between both magnitudes as expected from Eqs. 2.91-2.92. This in turn confirms that the wavelength shift of the LPG's notch is small enough to be proportional to the transmittance change over the entire power range. The smallest reliable perturbation was observed at a peak power of 10 W, corresponding to a transmittance variation of the probe signal $\sim0.01\%$ and a core effective index modulation of $\sim10^{-9}$, as shown in Fig. 3.8(b). For lower pump peak powers, modulation of the probe signal was observed but accurate calibration of the response could not be performed due to limitations of the experimental equipment. The Fourier transform of the temporal trace at 10 W is plotted in Fig. 3.8(c), yielding a signal-to-noise ratio (SNR) of >15 dB for most of the radial resonances. Within our experimental conditions, SNR >40 dB was achieved for large pump power [Fig. 3.6(c)], which makes this method a highly efficient and sensitive technique for measuring TAMRs in short fiber sections.

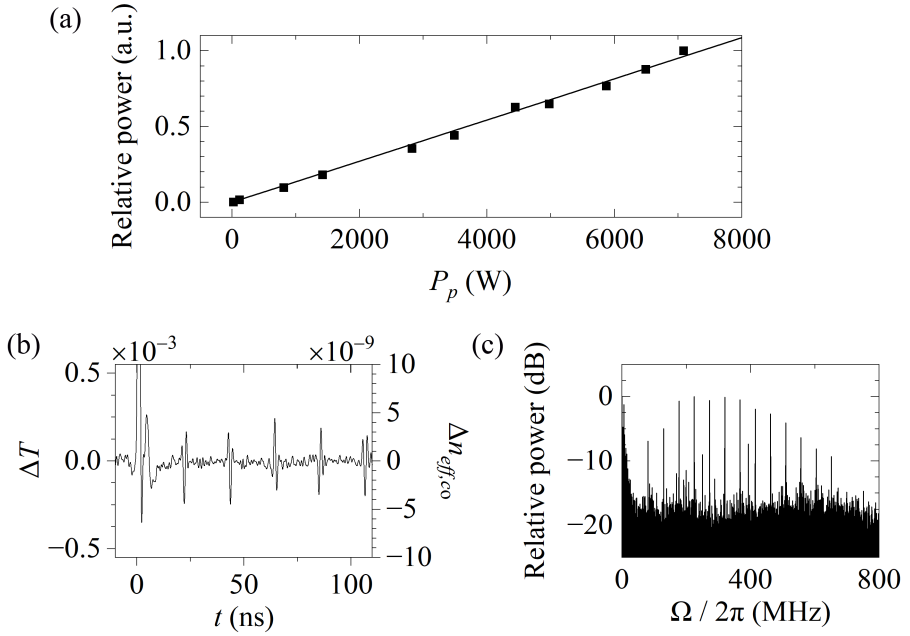

Figure 3.8: (a) $R_{0,10}$ amplitude as a function of the pump peak power, from 10 W to 7.1 kW. (b) Transmittance variation and core effective index modulation for a pump pulse peak power of 10 W. (c) Frequency response for a pump pulse peak power of 10 W.

(II). Fiber Bragg gratings

FBGs are designed to have periods of hundreds of nanometers, so point-by-point writing techniques become challenging. Instead, a phase mask is normally used. Diffraction of the UV laser on the phase mask produce a periodic intensity pattern with which the fiber is illuminated. The period of the written grating is equal to half the period of the phase mask. In this experiment, a phase mask with a period of 1047 nm was employed to write a 1-cm long FBG on the FUT. In this case, the polarization of the probe signal turned out to be much less critical than with the LPG, yet it was optimized to obtain the best possible contrast in the FBG. The transmission spectrum of an FBG used in the experiments is shown in Fig. 3.9. The reflection band was centered at 1556 nm with a 3 dB bandwidth of 125 pm and a depth of −10 dB. The slope of the linear part of the edges was

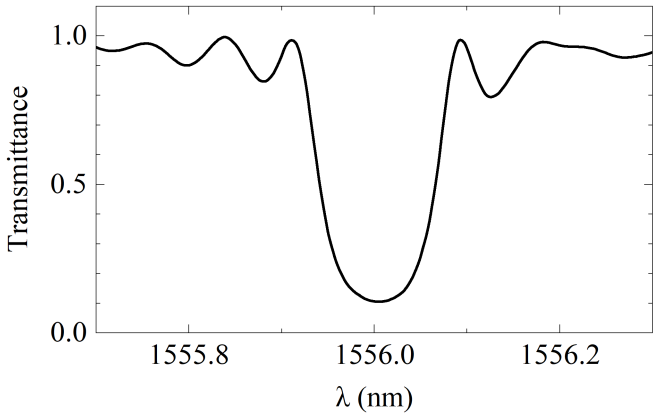

Figure 3.9: FBG transmittance spectrum ($\Lambda = 523.5$ nm, $L = 1$ cm). The operation principle is similar to the one shown in Fig 3.5.

-22.11 nm^{-1} and 23.62 nm^{-1} for left side and right side, respectively.

As with the LPG, we can obtain the modulation of the core effective from the variation in the transmittance of the FBG when the probe laser is tuned to one of the slopes. In this case, and taking into account the resonant wavelength expression for a FBG (3.2), we have that:

$$\Delta n_{eff,co} = -\frac{\Delta T}{2\,s\,\Lambda}. \tag{3.12}$$

The slope of the FBG's spectrum edges is about 20 times greater than those of the LPG, so one would expect to have a higher sensitivity to variations of core refractive index. However, this is countered by a grating period 100 times smaller than that of the LPG, and by the factor 2 of the denominator of Eq. 3.12. The result is that the FBG exhibited a sensitivity of about 2.5 times lower than the LPG. Such conclusion was confirmed experimentally. Figure 3.10(a)-(b) shows an example of experimental temporal trace recorded. The trace shows a more complex pattern than in the LPG scenario, with echoes of the main oscillations appearing at about 4.5 ns from them. Cross-phase modulation due to Kerr effect is also present at $t = 0$. The Fourier transform of the temporal trace after filtering

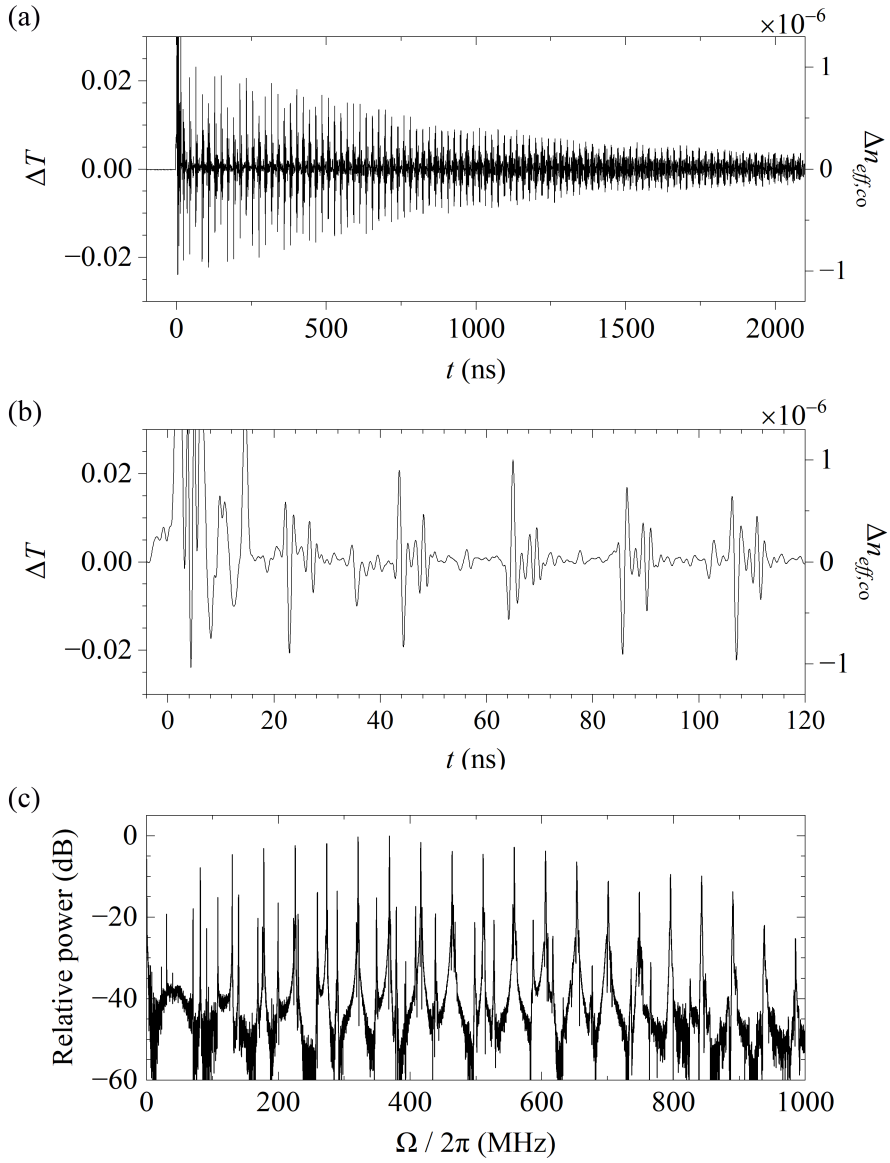

Figure 3.10: (a) Transmittance variation and core effective index modulation of the FBG due to TAMRs for a pump peak power of 4.5 kW. (b) Detailed plot of the first 120 ns. (c) Frequency response of the FBG obtained through fast Fourier transform of the temporal trace.

the Kerr response is shown in Fig. 3.10(c). Once again, both $R_{0,m}$ and $TR_{2,m}$ resonances are observed for a linear polarization of the pump wave.

Despite the lower sensitivity and more complex response of the FBG, it presents some advantages over the LPG in certain situations. For example, one of the most studied applications of forward Brillouin scattering is the external detection of liquids based on the acoustic impedance difference [5, 11, 12]. Under these circumstances, an LPG would require an additional wavelength tuning when changing the media outside the fiber, as it is sensitive to external changes by itself. FBGs, however, are not sensitive to changes of the outside material, so its resonance wavelength in the absence of pumping does not vary.

3.2 Whispering-gallery modes

Optical whispering-gallery modes (WGMs) are electromagnetic resonances that are confined within microcavities possessing rotational symmetry [13]. These cavities, which are typically made of a dielectric material, can be spherical, cylindrical or toroidal shaped. WGMs are resonance modes in which light circulates in the azimuthal direction, with its fields tightly confined near the resonator's surface through total internal reflection. The wavelengths at which WGMs oscillate are dependent on the cavity size, the type of geometry, shape, and material, and they can exhibit very high Q-factors. WGMs' exceptional properties have served as the basis for significant advances in several areas, including nonlinear optics [14], laser technologies [15, 16], and sensing [17]. In particular, optical fibers are cylindrical microresonators that support WGMs. In standard optical fibers, the Q factors of WGM resonances can be in the order of 10^7, with spectral bandwidths in the order of few tens of fm in the C-band.

The resonance wavelengths of WGMs can be determined by solving the characteristic equations that arise from applying the boundary conditions to the electromagnetic field [18]. WGMs in a cylindrical microresonator are classified according to the field in the axial direction into two families: transverse electric (TE^z) modes and transverse magnetic (TM^z) modes, each with its corresponding

characteristic equation. WGMs solutions are quantified by two integer numbers. The first one, p, is related with the angular variation of the fields, and the second, l, is related to their profile in the radial direction.

The fields of WGMs in a cylindrical microresonator for a TE polarization are given by

$r < a$	$r > a$
$H_z = A_1 J_p(k_0 n r)\, e^{-jp\phi}\, e^{j\omega t}$	$H_z = A_2 H_p^{(2)}(k_0 n_2 r)\, e^{-jp\phi}\, e^{j\omega t}$
$E_r = -\frac{p}{\omega\varepsilon_0\varepsilon}\frac{1}{r} A_1 J_p(k_0 n r)\, e^{-jp\phi}\, e^{j\omega t}$	$E_r = -\frac{p}{\omega\varepsilon_0\varepsilon_2}\frac{1}{r} A_2 H_p^{(2)}(k_0 n_2 r)\, e^{-jp\phi}\, e^{j\omega t}$
$E_\phi = -\frac{k_0 n}{j\omega\varepsilon_0\varepsilon} A_1 J_p'(k_0 n r)\, e^{-jp\phi}\, e^{j\omega t}$	$E_\phi = -\frac{k_0 n_2}{j\omega\varepsilon_0\varepsilon_2} A_2 H_p^{(2)'}(k_0 n_2 r)\, e^{-jp\phi}\, e^{j\omega t}$
$H_r = H_\phi = E_z = 0$	$H_r = H_\phi = E_z = 0$

(3.13)

while the fields for a TM polarization are,

$r < a$	$r > a$
$E_z = B_1 J_p(k_0 n r)\, e^{-jp\phi}\, e^{j\omega t}$	$E_z = B_2 H_p^{(2)}(k_0 n_2 r)\, e^{-jp\phi}\, e^{j\omega t}$
$H_r = \frac{p}{\omega\mu_0}\frac{1}{r} B_1 J_p(k_0 n r)\, e^{-jp\phi}\, e^{j\omega t}$	$H_r = \frac{p}{\omega\mu_0}\frac{1}{r} B_2 H_p^{(2)}(k_0 n_2 r)\, e^{-jp\phi}\, e^{j\omega t}$
$H_\phi = \frac{k_0 n}{j\omega\mu_0} B_1 J_p'(k_0 n r)\, e^{-jp\phi}\, e^{j\omega t}$	$H_\phi = \frac{k_0 n_2}{j\omega\mu_0} B_2 H_p^{(2)'}(k_0 n_2 r)\, e^{-jp\phi}\, e^{j\omega t}$
$E_r = E_\phi = H_z = 0$	$E_r = E_\phi = H_z = 0.$

(3.14)

The characteristic equations obtained after forcing the continuity of the tangential components of the electromagnetic field at the interface are,

$$n\frac{J_p'(k_0 n a)}{J_p(k_0 n a)} = n_2 \frac{H_p^{(2)'}(k_0 n_2 a)}{H_p^{(2)}(k_0 n_2 a)} \quad \text{(TE)}, \tag{3.15}$$

$$\frac{1}{n}\frac{J_p'(k_0 n a)}{J_p(k_0 n a)} = \frac{1}{n_2} \frac{H_p^{(2)'}(k_0 n_2 a)}{H_p^{(2)}(k_0 n_2 a)} \quad \text{(TM)}, \tag{3.16}$$

where n_2 is the refractive index of the external medium and $H_p^{(2)}$ is the Hankel function of the second kind. Figure 3.11(a) shows the resonance wavelengths of TE and TM WGMs for $l = 1$ in an optical fiber in the range of wavelength from $1530 - 1560$ nm. Figure 3.11(b)-(c) shows the electric field amplitude for a TM-polarized WGM of a silica optical fiber of 125 µm diameter, in particular, it corresponds to $p = 358$ and $l = 1$, whose resonance wavelength is $\lambda_{WGM} = 1536.31$ nm.

The resonance wavelength of WGMs can be expressed as a function of the effective index, n_{eff}. Since WGMs propagate in the azimuthal directions, the optical

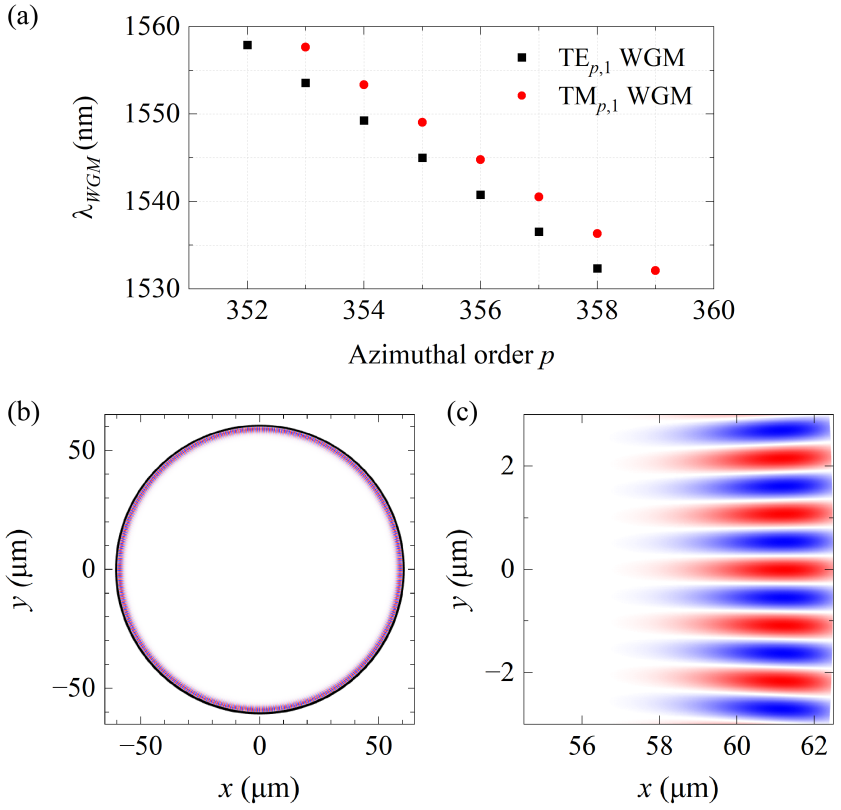

Figure 3.11: (a) Resonance wavelengths of TE and TM WGMs for $l = 1$ as a function of the azimuthal order p. (b) Electric field amplitude of the TM$_{358,1}$ WGM in a conventional optical fiber. (c) Close up of the field. Red and blue colors indicate positive and negative sign of the field, respectively.

wave undergoes self-interference after a complete round trip around the circular resonator. Constructive interference occurs, then the phase of the confined wave is the same with a difference of a multiple of 2π after a round trip. The resonant wavelength condition can be written then by [19],

$$\lambda_{WGM} = \frac{2\pi}{p} n_{eff}\, a, \tag{3.17}$$

where a is the radius of the microresonator. Eq. 3.17 shows in a clear way that λ_{WGM} will be sensitive to changes of the fiber radius and refractive index.

3.2.1 Interaction of WGMs with TAMRs

As in the case of fiber gratings, WGMs also experience a perturbation in their propagation properties due to the photo-elastic and geometrical contributions that result from the oscillation of TAMRs discussed earlier. In the following sections, we analyze the details of such perturbation.

(I). Photo-elastic contribution

For resonant waves, perturbations are usually expressed in terms of the resonant wavelength instead of the propagation factor. Therefore, the relative resonance wavelength shift of a WGM due to the change of permittivity caused by a TAMRs can be expressed as [20],

$$\frac{\Delta\lambda^{(n,m)}(t)}{\lambda_0} \approx \frac{\varepsilon_0 \int_S \mathbf{E}_0^* \cdot \Delta\bar{\boldsymbol{\varepsilon}}^{(n,m)}(t) \cdot \mathbf{E}_0\, dS}{\int_S (\varepsilon_0 \varepsilon \mathbf{E}_0 \cdot \mathbf{E}_0^* + \mu_0 \mathbf{H}_0 \cdot \mathbf{H}_0^*)\, dS}. \tag{3.18}$$

The numerator represents the overlap integral between the WGM and the perturbation. The integrand is given by,

$$\begin{aligned} \mathbf{E}_0^* \cdot \Delta\bar{\boldsymbol{\varepsilon}}^{(n,m)} \cdot \mathbf{E}_0 = {} & \Delta\varepsilon_{rr}^{(n,m)} |E_{0,r}|^2 + \Delta\varepsilon_{\phi\phi}^{(n,m)} \left|E_{0,\phi}\right|^2 + \Delta\varepsilon_{zz}^{(n,m)} |E_{0,z}|^2 \\ & + \Delta\varepsilon_{r\phi}^{(n,m)} (E_{0,r} E_{0,\phi}^* + E_{0,r}^* E_{0,\phi}). \end{aligned} \tag{3.19}$$

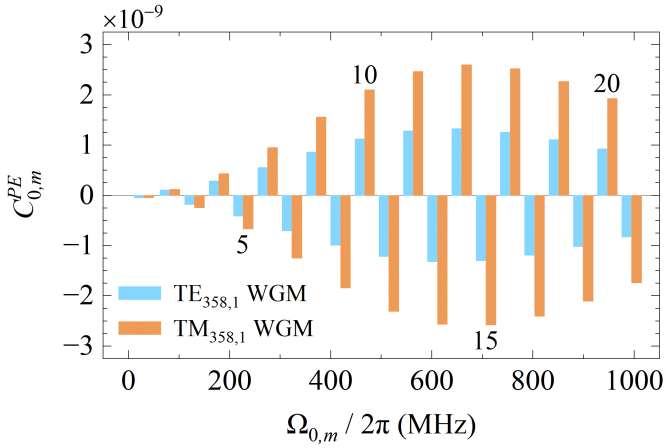

Figure 3.12: Amplitude $C_{PE}^{(0,m)}$ of the relative wavelength shift for $TE_{358,1}$ and $TM_{358,1}$ WGMs from the photo-elastic contribution of $R_{0,m}$ modes, excited by an optical pump pulse of 700 ps and 6 kW peak power. The order m of some $R_{0,m}$ modes is indicated.

For $R_{0,m}$ modes, both TE- and TM- polarized WGMs respond to perturbations in the dielectric permittivity, but in different ways. The electric field of TM-polarized WGMs involves only the axial component $E_{0,z}$, while the electric field of TE-polarized WGMs involves $E_{0,r}$ and $E_{0,\phi}$. As $\Delta\varepsilon_{r\phi}^{(n,m)} = 0$ for $R_{0,m}$ modes, the wavelength shift of TM-WGMs depends only on $\Delta\varepsilon_{zz}^{(n,m)}$, while the shift of TE-WGMs is determined by $\Delta\varepsilon_{rr}^{(n,m)}$ and $\Delta\varepsilon_{\phi\phi}^{(n,m)}$. For $TR_{2,m}$ modes, the dependence of the elements of the perturbed dielectric tensor with the azimuthal coordinate are either $\cos(2\phi)$ or $\sin(2\phi)$, and the integral with respect to ϕ in the numerator of Eq. 3.18 vanishes in both cases. Therefore, the perturbation of the dielectric tensor due to $TR_{2,m}$ modes does not yield any wavelength shift of the WGMs.

For $R_{0,m}$ modes generated by an optical pulse, we can follow the same notation in Eq. 2.94 to express the time evolution of the wavelength shift of the WGM. Thus,

$$\frac{\Delta\lambda^{(0,m)}(t)}{\lambda_0} \equiv C_{PE}^{(0,m)}\, e^{-(\Gamma_{0,m}/2)\,t}\, e^{j\Omega_{0,m}\,t}\, H(t). \tag{3.20}$$

where $C_{PE}^{(0,m)}$ is the amplitude of the relative wavelength shift owing to the photoelastic contribution of $R_{0,m}$ modes. Figure 3.12 shows $C_{PE}^{(0,m)}$ for $TE_{358,1}$ and $TM_{358,1}$ WGMs for the different $R_{0,m}$ modes excited by an optical pump pulse of 700 ps and 6 kW peak power. The wavelength shift produced by $R_{0,m}$ modes with even order m is π phase-shifted with respect to that produced by those with odd m order. The magnitude of the shift increases with the mode order up to the $R_{0,14}$ mode, and then it decreases with the mode order. For all radial modes, the effect on the TM-polarized WGMs is stronger. It is worth noting that the overlap between the acoustic and WGM fields does not strongly depend on the azimuthal order p, at least for our experimental conditions that involve large values of p. However, it does depend significantly with the radial order l of the WGM.

(I). Geometrical contribution

The geometrical perturbation of $R_{0,m}$ modes to the WGM resonance wavelength can be modelled by assuming a change in the total fiber radius given by $\delta a(t) \equiv U_r^{(0,m)}(r,t)|_{r=a_0} = B_{0,m}(t)\, u_r^{(0,m)}(r)|_{r=a_0}$, where a_0 is the radius of the unperturbed fiber. For $R_{0,m}$ modes generated by an optical pulse, we can express the relative wavelength shift as,

$$\frac{\Delta\lambda^{(0,m)}(t)}{\lambda_0} \equiv C_{GE}^{(0,m)}\, e^{-(\Gamma_{0,m}/2)\,t}\, e^{j\Omega_{0,m}\,t}\, H(t). \tag{3.21}$$

The calculation of the amplitude of the relative wavelength shift $C_{GE}^{(0,m)}$ was performed by numerically solving the corresponding characteristic equation for TE- and TM-polarized WGM resonances of a dielectric silica cylinder immersed in air [21]. First, for a cylinder of radius a_0, and then for a cylinder of radius $a_0 + \delta a$, here $\delta a = B_{n,m}^{(0)}\, u_r^{(0,m)}(r)|_{r=a_0}$ is the amplitude of the radius perturbation induced by $R_{0,m}$ modes. Figure 3.13 shows $C_{GE}^{(0,m)}$ for $TE_{358,1}$ and $TM_{358,1}$ WGMs, and acoustic modes excited by an optical pump pulse of 700 ps and 6 kW peak power. Once again, the modes with even and odd m order produce a WGM resonance wavelength shift with opposite sign. However, nearly identical results are obtained for both polarizations of the WGM on this occasion. The

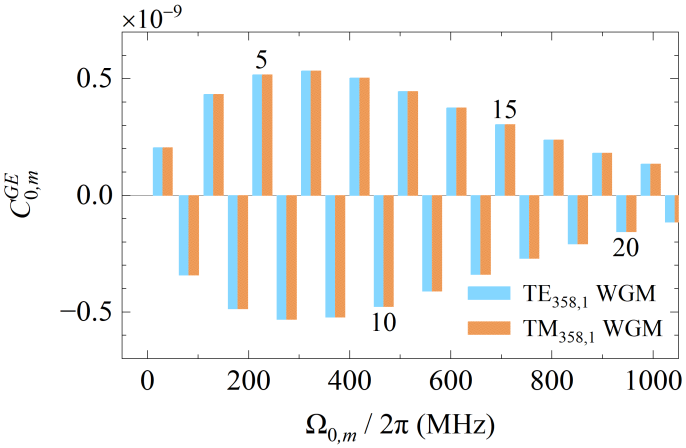

Figure 3.13: Amplitude $C_{GE}^{(0,m)}$ of the relative wavelength shift for $TE_{358,1}$ and $TM_{358,1}$ WGMs from the geometrical contribution of $R_{0,m}$ modes, excited by an optical pump pulse of 700 ps and 6 kW peak power. The order m of some $R_{0,m}$ modes is indicated.

amplitude of the WGM wavelength shift produced by the geometrical contribution of lower order $R_{0,m}$ modes is significantly large, in comparison to their photo-elastic contribution counterpart (Fig. 3.12).

Figure 3.14 shows the overall amplitude of the relative wavelength shift taking into account the two contributions of $R_{0,m}$ modes. As, for each m, the contributions are of opposite sign, they can partially counteract each other. The relative wavelength shift caused by radial acoustic modes with low order m is driven essentially by the geometrical contribution, while for large m values is the photo-elastic effect that dominates. For radial modes for which the two contributions are of similar magnitude, the net effect on the WGM is minimum.

The geometrical perturbation caused by the oscillation of $TR_{2,m}$ modes can be expressed as $a_0 + \delta a \Phi(\phi)$, where $\Phi(\phi) \propto \left\{ \begin{smallmatrix} \cos(2\phi) \\ \sin(2\phi) \end{smallmatrix} \right\}$ is the function that describes the azimuthal dependence of the perturbation. The resonance wavelength of a WGM under such a shape perturbation can be approximated by the following series [22],

$$\frac{1}{\lambda} = \frac{1}{\lambda_0}(1 - \delta a A_{pp}) + O(\lambda^2), \tag{3.22}$$

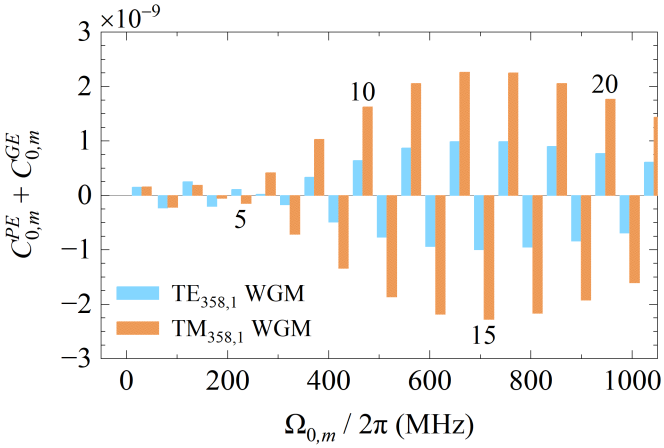

Figure 3.14: Overall amplitude $C^{(0,m)}_{PE} + C^{(0,m)}_{GE}$ for $TE_{358,1}$ and $TM_{358,1}$ WGMs, excited by an optical pump pulse of 700 ps and 6 kW peak power. The order m of some $R_{0,m}$ modes is indicated.

where the coefficient A_{pp} is given by,

$$A_{pp} = \frac{2}{\pi a} \int_0^{\pi} \Phi(\phi) \cos^2(p\phi)\, d\phi, \tag{3.23}$$

where p is the azimuthal order of the WGM. The integral in Eq. 3.23 vanishes when p is an integer and $\Phi(\phi) \propto \left\{ \begin{smallmatrix} \cos(2\phi) \\ \sin(2\phi) \end{smallmatrix} \right\}$. Therefore, the perturbation induced by the $TR_{2,m}$ modes does not produce a shift of the WGM wavelength, at least to a first order approximation.

3.2.2 Coupling to an oscillating cavity

The typical method employed for exciting and detecting WGM resonances in an optical microresonator involves the use of an evanescent field, usually from an auxiliary waveguide, such as a thin fiber taper. The amplitudes of the signal within the microresonator and the transmitted signal through the auxiliary waveguide are influenced by the characteristics of both the microresonator and the auxiliary waveguide, as well as their coupling efficiency. The oscillation of a $R_{0,m}$ mode in the fiber leads to oscillations in the resonance wavelength of the

fiber's WGMs. This temporal variation in the resonance frequency of the WGMs has implications for their excitation and detection.

When a $R_{0,m}$ mode oscillates in the fiber, the frequency difference between the optical field and the WGM resonance frequency can be expressed as $\Delta\omega(t) = \Delta\omega_{DC} + \Delta\omega_{AC}\cos(\Omega t)$, where $\Delta\omega_{DC}$ represents the detuning in the absence of oscillation, $\Delta\omega_{AC}$ is the amplitude of oscillation caused by the radial mode, and Ω is the oscillation frequency. The temporal oscillation of the WGM resonance frequency introduces an oscillation in the amplitude of the wave transmitted through the fiber taper, compared to a static coupled system. In the steady state, when the cavity perturbation is small and the optical field is tuned to the slope of the WGM resonance, the power of the transmitted signal can be described as

$$T_{st}(t) \approx T_{DC} + \Delta T_{AC}\cos(\Omega t + \theta), \tag{3.24}$$

where T_{st} represents the steady-state transmittance, T_{DC} is the transmittance in

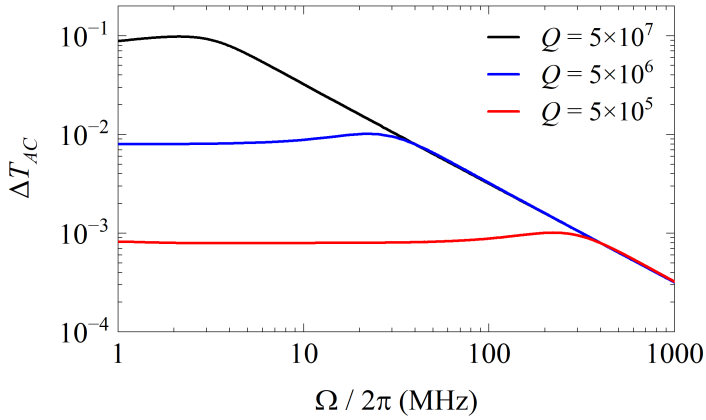

Figure 3.15: Modulation amplitude of the power transmittance ΔT_{AC} as a function of the cavity vibration frequency Ω. Three representative values of Q used in the calculations correspond to linewitdhs of 30 fm, 300 fm and 3 pm, respectively, at the optical wavelength of 1.5 µm. An oscillation amplitude of $\Delta\omega_{AC} = 1\times10^6\ \mathrm{rad\,s^{-1}}$, which corresponds to a wavelength shift amplitude of 1.2 fm, was considered for the three cases.

the absence of cavity frequency modulation, and ΔT_{AC} is the amplitude of output power modulation due to the cavity perturbation. ΔT_{AC} depends on the strength of the cavity frequency modulation $\Delta\omega_{AC}$, thus it provides information about the amplitude of the acoustic oscillation inside the cavity. Further details on this analysis can be found in Appendix B.

It is important to note that ΔT_{AC} depends on the optical frequency ω, the Q factor of the WGM resonance, and the frequency Ω at which the cavity oscillates. The dependence on Ω is particularly interesting as it reveals the role of the Q factor. Figure 3.15 illustrates ΔT_{AC}, computed for a constant $\Delta\omega_{AC}$, as a function of frequency within the relevant range for three different values of Q. We observe that $\Delta T_{AC}(\Omega)$ exhibits a low-pass filter response, where the transmittance at low frequencies is proportional to the Q factor, while the cut-off frequency is inversely proportional to Q. This effect becomes significant when using ultra-narrowband WGMs, i.e., resonances with ultra-high Q factors. In other words, the sensitivity of the probing technique based on the transmittance of a WGM resonance significantly increases with the Q factor, enabling optimized detection of lower order $R_{0,m}$ modes. However, if high bandwidth is required, WGM resonances with lower Q factors provide a flatter response over a wider frequency range.

3.2.3 Experimental results and discussion

Figure 3.16(a) shows a schematic of the experimental setup. The FUT used in this study was again a section of Fibercore SM1500-4.2/125, selected for comparative purposes with the results obtained with methods presented in the previous section. WGMs of the FUT were excited and probed by evanescence-field coupling from a thin tapered optical fiber with a diameter of approximately 3 µm. The tapered fiber was fabricated from Corning SMF-28 using a fusion-and-pulling technique [23, 24]. It was positioned perpendicular to the FUT in contact with it. The probe light source used in this study was a tunable diode laser (New Focus 6326 Velocity) with a linewidth < 30 kHz, and its polarization state was adjusted using a polarization controller to excite either TE- or TM-polarized

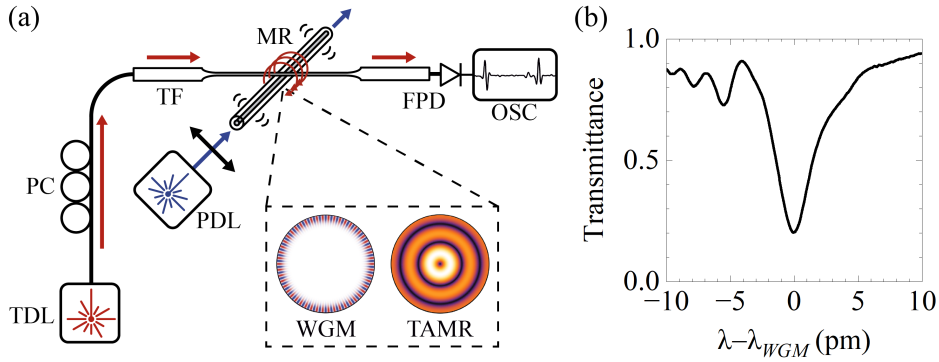

Figure 3.16: (a) Scheme of the experimental setup employed with WGM resonances. TF: tapered fiber; MR: microresonator. The remaining acronyms are the same as in Fig. 3.4. (b) Example of a WGM spectrum ($\lambda_{WGM} = 1535.9$ nm, $\Delta\lambda_{3dB} = 2.8$ pm, $Q = 5.5 \times 10^5$).

WGMs of the FUT. The pulsed pump laser employed to generate the TAMRs inside the FUT was the same as described in Section 3.1.

The spectra of the WGMs were obtained by fine-frequency sweeping of the tunable laser using a built-in piezoelectric-tuning option, which allowed for continuous scanning around a central wavelength. Excitation of a WGM in the microresonator resulted in a notch in the spectrum of the light transmitted through the fiber taper, as shown in Fig. 3.16(b). To interrogate the FUT vibration, the laser was precisely adjusted to match the spectral slope of the WGM notch. Then, wavelength modulations due to the presence of TAMRs are converted into an intensity modulated signal, which was detected and recorded using an amplified fast photodetector (New Focus 1611) and an oscilloscope. To counteract low-frequency fluctuations resulting from the environmental noise, an active locking technique relying on an electronic feedback control system was employed to stabilize the probe signal [25].

Firstly, we focused on low-Q factor WGMs to ensure a broad frequency response consistent with the calculations in Fig. 3.15. One of the WGMs used in the experiments is shown in Fig. 3.16(b), with a notch located at 1535.9 nm, exhibiting a 3 dB-bandwidth of 2.8 pm and a Q factor of 5.5×10^5. This notch

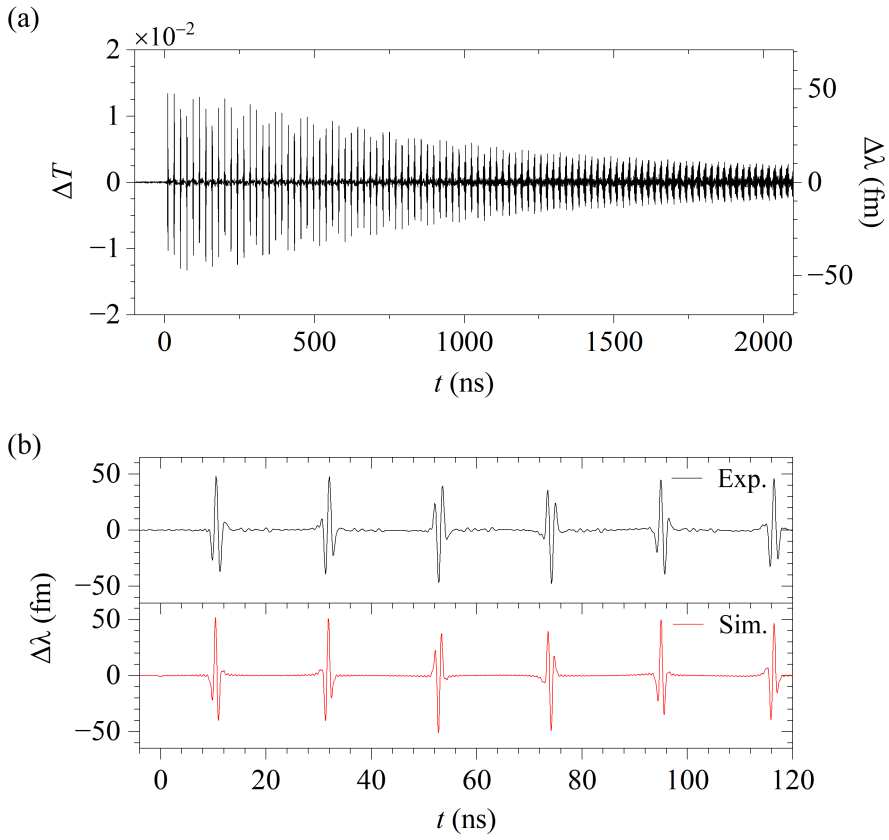

Figure 3.17: (a) Transmittance variation and wavelength shift of the WGM due to $R_{0,m}$ modes for a pump peak power of 6 kW. The trace was the result of 1064 averages. (b) Experimental and simulated plot of the first 120 ns.

corresponds to the excitation of the $TM_{358,1}$ WGM. Figure 3.17(a) shows an example of the probe signal's transmittance oscillation recorded after one pump pulse propagated along the fiber at $t = 0$. The probe laser was tuned to the left slope ($s = -0.28$ pm^{-1}). Changes in the polarization of the pump wave did not produce any modification in the trace. It can be observed that, in this scenario, only oscillations resulting from the presence of $R_{0,m}$ resonances are observed. The transmittance variation can be correlated with the wavelength shift of the WGM through the slope of the notch. For example, for a pump power of 6 kW, the wavelength shift corresponding to the peak amplitude of the first oscillation is

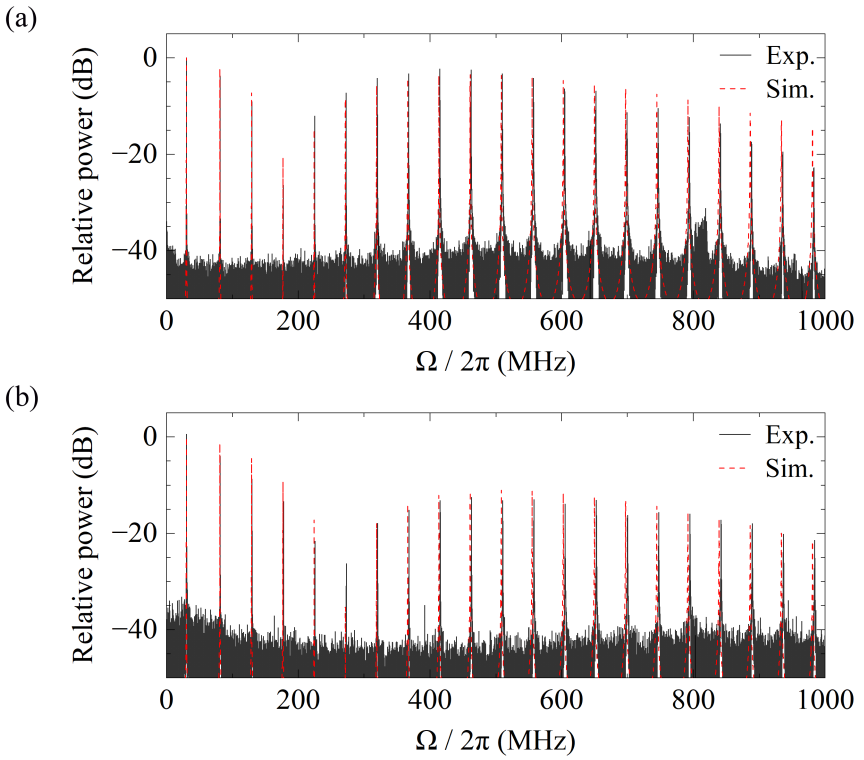

Figure 3.18: Experimental and simulated frequency response of the microresonator due to $R_{0,m}$ modes when probing with (a) $TM_{358,1}$ and (b) $TE_{358,1}$ WGM.

$\sim$48 fm. It must be noticed the absence of the instantaneous Kerr effect-induced XPM at $t = 0$ in Fig. 3.17(b). A simulation of $\Delta\lambda(t) = \sum \Delta\lambda^{(0,m)}(t)$ calculated from Eq. 3.20 and 3.21 is also included, considering both photo-elastic and geometrical contributions of the $R_{0,m}$ modes.

The radio-frequency spectra of the probe signals obtained using $TM_{358,1}$ and $TE_{358,1}$ WGMs are presented in Fig. 3.18. A series of peaks, each one resulting from the interaction between a radial mode and the WGM is shown. In both cases, the peak with the highest intensity corresponds to the $R_{0,1}$ mode, which is a notable difference compared to methods of TAMR probing at the core of the fiber. It is worth noting that the contribution of the dielectric tensor perturbation induced by the $R_{0,1}$ mode is relatively small, as shown in Fig.

3.12. This result demonstrates the impact of the fiber's geometrical perturbation caused by TAMRs on the WGM resonance. Frequency components related to $TR_{2,m}$ modes were not observed in any case, in agreement with the theoretical discussion of Section 3.2.1. The envelope of the RF spectra shows a minimum in amplitude which arises from the opposing signs of the two contributions to the WGM wavelength shift. When the geometrical and refractive index contributions are of comparable magnitude, they can partially cancel each other out. For the specific WGMs utilized in this study, the peaks with the lowest amplitude were $R_{0,4}$ mode for $TM_{358,1}$ and $R_{0,6}$ mode for $TE_{358,1}$, consistent with Fig. 3.13(b).

High-resolution spectra of individual radial modes were obtained using a signal analyzer, and their linewidth was determined by fitting a Lorentzian function, as

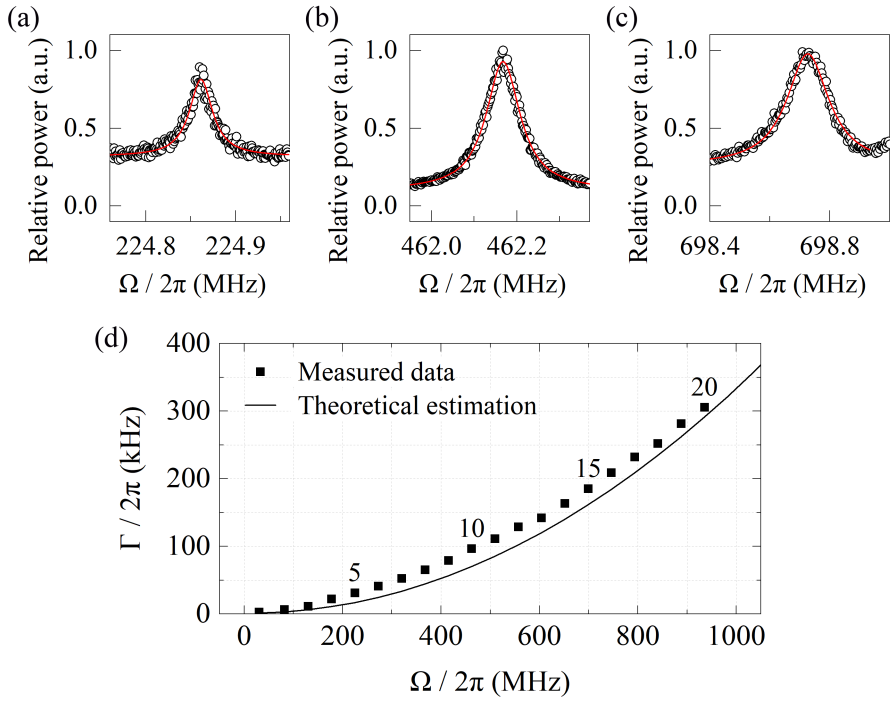

Figure 3.19: RF spectrum showing acoustic resonances (a) $R_{0,5}$, (b) $R_{0,10}$ and (c) $R_{0,15}$; dots: experimental data; red line: Lorentzian fit. (d) Measured linewidth of $R_{0,m}$ resonances and theoretical estimation from 2.2.3 for a point measurement.

shown in Figs. 3.19(a)-(c). No asymmetries were observed due to XPM caused by Kerr effect. Fig. 3.19(d) shows the measured linewidths and the estimated ones considering linewidth broadening due to viscous and surface damping only. The experimental values are just slightly above the theoretical calculation, which corroborates that the contribution to linewidth broadening due to the fiber inhomogeneties is very small and it could eventually be neglected. The linewidth values measured by this method were about 25% smaller than those obtained through an LPG (Fig. 3.7). We explain such improvement due to the small extension of the probe light beam along the axis of the fiber under test ($\sim$ 200 µm [26])

WGMs with higher quality factors were also tested for the measurement of TAMRs. To enhance the Q factor of the WGMs, the fiber underwent a thermal treatment to reduce surface roughness and contaminants [27]. Figure 3.20 presents measurements obtained with TM-WGMs of higher Q factors, 3.3×10^6

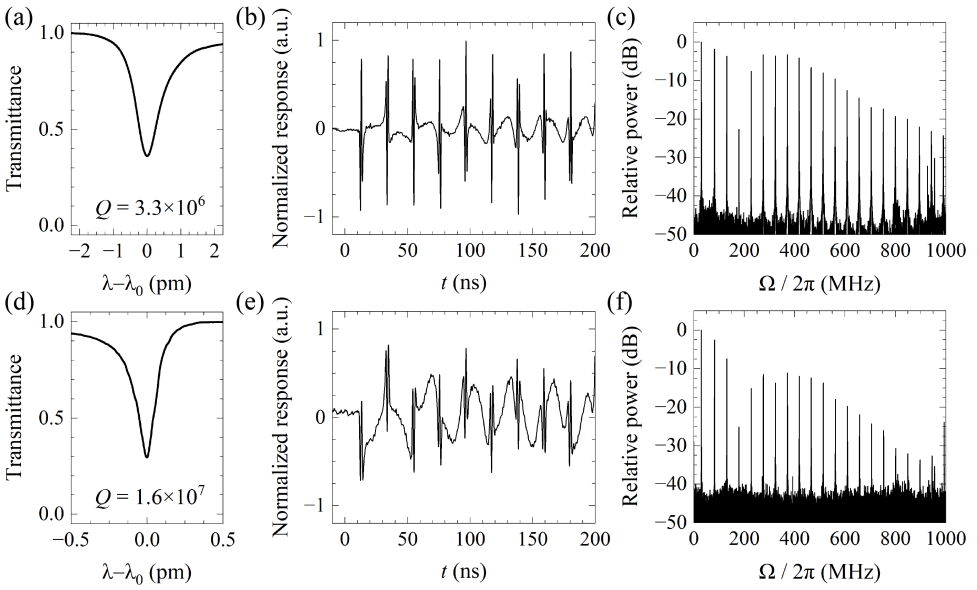

Figure 3.20: Experimental results for the $TM_{358,1}$ WGM with different Q factor. (Left) WGM spectrum, (center) Temporal trace of the probe signal, and (right) radio-frequency spectrum of the probe signal.

and 1.6×10^7, corresponding to bandwidths of 465 fm and 92 fm, respectively. For each measurement, it is shown the WGM spectrum, a temporal trace of the probe signal just after a pump pulse propagated through the fiber, and the radio-frequency spectrum. The experimental conditions were similar in all the measurements, including pump power. As the Q factor of the WGM used for the measurement increases, the contribution of low-frequency harmonics to the temporal trace becomes more noticeable due to the increase of the slope of the WGM notch. The oscilloscope traces depicted in Figs. 3.20(b) and (e) show a clear modulation of ~ 30 MHz caused by the $R_{0,1}$ mode. Additionally, as the Q factor increases, the amplitude of high-order resonances fades away due to the low-pass filtering response described in Section 3.2.2, as observed in the radio-frequency spectra.

References

[1] T. Erdogan, "Fiber grating spectra", *Journal of Lightwave Technology*, vol. 15, no. 8, pp. 1277–1294, 1997.

[2] T. Erdogan, "Cladding-mode resonances in short- and long-period fiber grating filters", *Journal of the Optical Society of America A*, vol. 14, no. 8, p. 1760, 1997.

[3] A. W. Snyder and J. D. Love, *Optical Waveguide Theory*. Boston, MA: Springer US, 1984.

[4] A. Zadok, H. H. Diamandi, Y. London, and G. Bashan, *Forward Brillouin Scattering in Standard Optical Fibers: Single-Mode, Polarization-Maintaining, and Multi-Core* (Springer Series in Optical Sciences). Springer International Publishing, 2022, vol. 240.

[5] H. H. Diamandi *et al.*, "Opto-mechanical interactions in multi-core optical fibers and their applications", *IEEE Journal of Selected Topics in Quantum Electronics*, vol. 26, no. 4, 2020.

[6] L. Poveda-Wong, J. L. Cruz, M. Delgado-Pinar, X. Roselló-Mechó, A. Díez, and M. V. Andrés, "Fabrication of long period fiber gratings of sub-nanometric bandwidth", *Optics Letters*, vol. 42, no. 7, p. 1265, 2017.

[7] E. Rivera-Pérez, A. Carrascosa, A. Díez, E. P. Alcusa-Sáez, and M. V. Andrés, "An approach to the measurement of the nonlinear refractive index of very short lengths of optical fibers", *Applied Physics Letters*, vol. 113, no. 1, pp. 1–4, 2018.

[8] J. Wang, Y. Zhu, R. Zhang, and D. J. Gauthier, "FSBS resonances observed in a standard highly nonlinear fiber", *Optics Express*, vol. 19, no. 6, p. 5339, 2011.

[9] G. Bashan, H. H. Diamandi, Y. London, E. Preter, and A. Zadok, "Optomechanical time-domain reflectometry", en, *Nature Communications*, vol. 9, no. 1, p. 2991, 2018.

[10] C. Pang *et al.*, "Opto-mechanical time-domain analysis based on coherent forward stimulated Brillouin scattering probing", en, *Optica*, vol. 7, no. 2, p. 176, 2020.

[11] H. H. Diamandi, Y. London, G. Bashan, and A. Zadok, "Distributed opto-mechanical analysis of liquids outside standard fibers coated with polyimide", *APL Photonics*, vol. 4, no. 1, p. 016 105, 2019.

[12] D. M. Chow and L. Thévenaz, "Forward Brillouin scattering acoustic impedance sensor using thin polyimide-coated fiber", *Optics Letters*, vol. 43, no. 21, p. 5467, 2018.

[13] V. B. Braginsky, M. L. Gorodetsky, and V. S. Ilchenko, "Quality-factor and nonlinear properties of optical whispering-gallery modes", *Physics Letters A*, vol. 137, no. 7, pp. 393–397, 1989.

[14] T. J. Kippenberg, R. Holzwarth, and S. A. Diddams, "Microresonator-based optical frequency combs", *Science*, vol. 332, pp. 555–559, 2011.

[15] M. Humar and S. H. Yun, "Intracellular microlasers", *Nature Photonics*, vol. 9, pp. 572–576, 2015.

[16] S. Spillane, T. Kippenberg, and K. Vahala, "Ultralow-threshold Raman laser using a spherical dielectric microcavity", *Nature*, vol. 415, pp. 621–623, 2002.

[17] J. Zhu *et al.*, "On-chip single nanoparticle detection and sizing by mode splitting in an ultrahigh-Q microresonator.", *Nature Photonics*, vol. 4, no. 1, pp. 46–49, 2009.

[18] J. R. Wait, "Electromagnetic whispering gallery modes in a dielectric rod", *Radio Science*, vol. 2, no. 9, pp. 1005–1017, 1967.

[19] T. Birks, J. Knight, and T. Dimmick, "High-resolution measurement of the fiber diameter variations using whispering gallery modes and no optical alignment", en, *IEEE Photonics Technology Letters*, vol. 12, no. 2, pp. 182–183, 2000.

[20] D. M. Pozar, *Microwave Engineering, 4th Edition*. Wiley, 2011.

[21] G. Annino, M. Cassettari, I. Longo, and M. Martinelli, "Whispering gallery modes in a dielectric resonator: Characterization at millimeter

wavelength", *IEEE Transactions on Microwave Theory and Techniques*, vol. 45, no. 11, pp. 2025–2034, 1997.

[22] R. Dubertrand, E. Bogomolny, N. Djellali, M. Lebental, and C. Schmit, "Circular dielectric cavity and its deformations", vol. 77, p. 013 804, 2008.

[23] R. P. Kenny, T. A. Birks, and K. P. Oakley, "Control of optical fibre taper shape", en, *Electronics Letters*, vol. 27, no. 18, pp. 1654–1656, 1991.

[24] T. Birks and Y. Li, "The shape of fiber tapers", en, *Journal of Lightwave Technology*, vol. 10, no. 4, pp. 432–438, 1992.

[25] T. Carmon, T. J. Kippenberg, L. Yang, H. Rokhsari, S. Spillane, and K. J. Vahala, "Feedback control of ultra-high-Q microcavities: Application to micro-Raman lasers and micro-parametric oscillators", *Optics Express*, vol. 13, no. 9, pp. 3558–3566, 2005.

[26] M. Sumetsky, "Mode localization and the Q-factor of a cylindrical microresonator", *Optics Letters*, vol. 35, no. 14, pp. 2385–2387, 2010.

[27] M. L. Gorodetsky, A. A. Savchenkov, and V. S. Ilchenko, "Ultimate Q of optical microsphere resonators", *Optics Letters*, vol. 21, no. 7, pp. 453–455, 1996.

4 | Novel applications of FBS

In this chapter, we will present our contribution in relation to applications based on FBS in optical fibers. On the one hand, we have applied the FBS concepts developed in previous chapters in the field of fiber optic sensing. Secondly, FBS has allowed us to implement new techniques for characterizing the mechanical properties of optical fibers. While previous applications of TAMRs and FBS have mainly based on the properties of either $R_{0,m}$ or $TR_{2,m}$ acoustic resonances, we demonstrate here that the capabilities of TAMRs can be further expanded by considering and combining the characteristics and response of both type of acoustic modes. In addition, the detection of these modes using fiber gratings allows for point-measurements with a very high accuracy. In particular, we will show the simultaneous and discriminative sensing of strain and temperature and the characterization of the Poisson's ratio of the optical fiber with unprecedented accuracy, as well as its dependence on the above mentioned magnitudes.

4.1 Fundamentals

As we have seen in Section 2.2, the resonance frequencies of the acoustic modes $R_{0,m}$ and $TR_{2,m}$ can be approximated by the following expressions,

$$\Omega_{0,m} \approx \frac{V_L}{a}\left(c_m - \frac{16\alpha^2 - 1}{8c_m}\right), \tag{4.1}$$

$$\Omega^{(1)}_{2,m} \approx \frac{V_S}{a}\left(c_{m+1} - \frac{15}{8c_{m+1}}\right), \tag{4.2}$$

$$\Omega^{(2)}_{2,m} \approx \frac{V_L}{a}\left(c_{m+1} - \frac{15}{8c_{m+1}}\right), \tag{4.3}$$

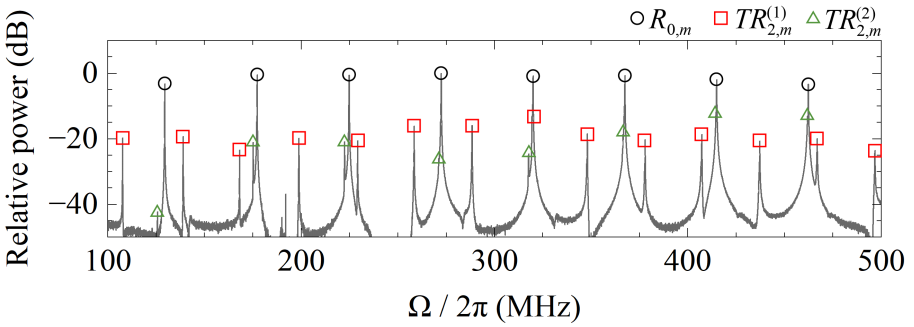

Figure 4.1: TAMRs spectrum from 100 MHz to 500 MHz at room temperature obtained from the response of an LPG. $R_{0,m}$ modes are denoted by circles while $TR^{(1)}_{2,m}$ and $TR^{(2)}_{2,m}$ are denoted by squares and triangles, respectively.

where $c_m = m\pi - \pi/4$, $m = 1,2,3,\ldots$. Equations 4.1-4.3 reveal a fundamental feature, i.e., the splitting of torsional-radial resonances into two distinct series, referred to as $TR^{(1)}_{2,m}$ and $TR^{(2)}_{2,m}$. The asymptotic cutoff frequency values of series $TR^{(1)}_{2,m}$ are primarily determined by V_S, while those values of series $TR^{(2)}_{2,m}$ are determined by V_L. Furthermore, the $TR^{(2)}_{2,m}$ and $R_{0,m}$ series are nearly degenerate. By using this asymptotic expressions, we can easily distinguish in an experimental spectrum to which series each resonance belongs and its order m, as depicted in the example shown in Fig. 4.1. The series $TR^{(2)}_{2,m}$ of torsional-radial resonances presents a similar behavior than the radial mode series, and they do not add much additional information compared to that provided by radial modes. The amplitude of radial modes in the spectrum are generally much larger, thus, from the practical point of view they are more useful than $TR^{(2)}_{2,m}$. The applications that follows rely on the properties of the $R_{0,m}$ modes and the $TR^{(1)}_{2,m}$.

Following Eqs. 4.1 and 4.2, we can fit the experimental resonance frequencies of $R_{0,m}$ modes and the $TR^{(1)}_{2,m}$ modes to,

$$\frac{\Omega_{0,m}}{2\pi} = A\left(c_m - \frac{B}{8c_m}\right), \tag{4.4}$$

$$\frac{\Omega^{(1)}_{2,m}}{2\pi} = C\left(c_{m+1} - \frac{15}{8c_{m+1}}\right), \tag{4.5}$$

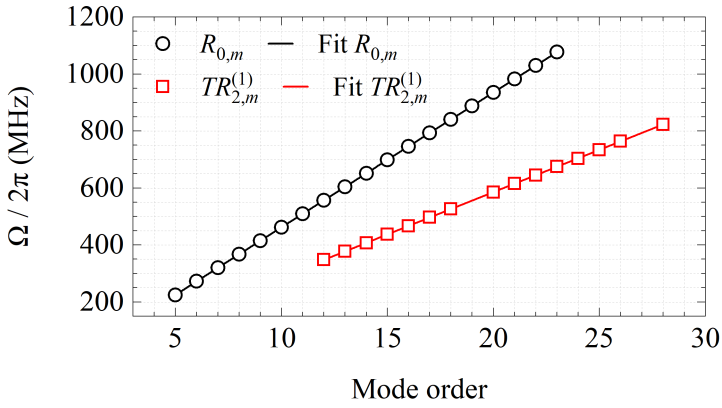

Figure 4.2: Experimental resonance frequencies for $R_{0,m}$ and $TR^{(1)}_{2,m}$ modes recorded at room temperature, along with their fits.

where A, B and C are fitting parameters. Figure 4.2 shows an example. The experimental resonance frequencies for both series of modes recorded at room temperature, along with the best least squares fits, are presented. As the error introduced by Eqs. 4.1-4.3 decreases with the mode order (see Appendix A), the lower order modes were removed from the fit. In particular, radial resonances from $m = 5$ to $m = 23$, and torsional-radial resonances from $m = 12$ to $m = 28$ were included in the fitting. Missing points in the $TR^{(1)}_{2,m}$ family correspond to resonances overlapping with a $R_{0,m}$ resonance, which may cause a significant error when determining the resonant frequency (see Fig. 4.1 at around 320 MHz, as an example).

Comparing Eqs. 4.1-4.2 and Eqs. 4.4-4.5, the fitting parameters A and C correspond to $V_L/(2\pi a)$ and $V_S/(2\pi a)$, respectively. For the experimental measurements shown in Fig. 4.2, we obtained the values $V_L/a = (94\,463 \pm 6) \times 10^3$ s^{-1} and $V_S/a = (59\,345 \pm 9) \times 10^3$ s^{-1}. Then, the acoustic velocities can be determined if the radius of the fiber is measured. Considering the error values of V_L/a and V_S/a, the precision with which the velocities can be obtained is mainly determined by the accuracy of the fiber radius measurement, particularly for radius uncertainties larger than 1 nm.

4.2 Simultaneous strain and temperature measurement

Optical fibers have proven to be a versatile platform for sensing a wide range of physical magnitudes. One of the most relevant applications of fiber optic sensors is the measurement of strain and temperature. However, discrimination between strain and temperature measurements in many fiber optic sensors can be challenging, as both magnitudes often interfere with the sensor in the same way. To overcome this limitation, various strategies, adapted to each specific type of sensor, have been developed. In the case of fiber grating-based sensors, several temperature and strain discriminating techniques have been proposed, most of them involving two independent measurements with two gratings [1–5], although techniques involving measurements of two magnitudes in a single grating have been also proven [6–8].

Discrimination between these two magnitudes is also an issue in Brillouin fiber-optic distributed sensors, since the Brillouin frequency shift depends linearly on both magnitudes. Several solutions have been proposed to develop Brillouin-based sensors with discrimination capacity using a single fiber, such as the use of specialty optical fibers like PM fibers [9], Er^{3+}-doped fibers [10], or few-mode optical fibers [11]. However, many of these methods require technically complex measurement procedures. In recent years, there has been a surge of interest in using forward Brillouin scattering as a physical mechanism for fiber sensing. FBS offers unique sensing capabilities as it relies not only on the properties of the fiber itself but also on the surrounding environment [12, 13]. Furthermore, the potential of distributed fiber sensing using FBS has been successfully demonstrated [14–16]. In this context, we demonstrated that FBS in optical fibers represents an attractive alternative for strain and temperature sensing, offering a simple and reliable method for discrimination between these two parameters with high spatial resolution.

The approach that we proposed consist on combining the different response of $R_{0,m}$ and $TR^{(1)}_{2,m}$ modes to those magnitudes. For moderate changes of tempera-

ture and axial strain applied to the fiber, the shift of the resonance frequencies is rather linear. However, the temperature and axial strain coefficients of the longitudinal and shear acoustic velocities in the optical fiber are different, i.e., $\partial V_L/\partial T \neq \partial V_S/\partial T$ and $\partial V_L/\partial S_z \neq \partial V_S/\partial S_z$. Therefore, the temperature and strain sensitivity of $\Omega_{0,m}$ and $\Omega^{(1)}_{2,m}$ are different. The relative frequency shifts of an $R_{0,m}$ resonance and a $TR^{(1)}_{2,m}$ resonance can be expressed in terms of the changes in temperature (ΔT) and strain ($\Delta S_z = \Delta L/L_0$) applied to the fiber as,

$$\begin{pmatrix} \Delta\Omega_{0,m}/\Omega_{0,m} \\ \Delta\Omega^{(1)}_{2,m}/\Omega^{(1)}_{2,m} \end{pmatrix} = \begin{pmatrix} c^{S_z}_{0,m} & c^{T}_{0,m} \\ c^{S_z}_{2,m} & c^{T}_{2,m} \end{pmatrix} \begin{pmatrix} \Delta S_z \\ \Delta T \end{pmatrix}, \tag{4.6}$$

where $c^{S_z}_{0,m}$ and $c^{T}_{0,m}$ are the strain and temperature coefficients of radial resonance, and $c^{S_z}_{2,m}$ and $c^{T}_{2,m}$ are the coefficients of the torsional-radial mode of the first series. According to Eqs. 4.1 and 4.2, and for large mode orders, the relative frequency shift of all resonances within a given family will be nearly independent of the order m, which enables the possibility of using several resonances pairs to improve the accuracy of the sensor. Similarly, the coefficients $c^{S_z}_{0,m}$, $c^{T}_{0,m}$, $c^{S_z}_{2,m}$ and $c^{T}_{2,m}$ are common for all modes of the same series, thus, averaging the response of the different resonances can be applied to reduce the error with which they are obtained.

The errors for the strain and temperature increments, $e_{\Delta S_z}$ and $e_{\Delta T}$, can be obtained as [17],

$$e_{\Delta S_z} = \frac{\sqrt{\left(c^{T}_{2,m}\, e_{0,m}\right)^2 + \left(c^{T}_{0,m}\, e_{2,m}\right)^2}}{\left|c^{S_z}_{0,m}\, c^{T}_{2,m} - c^{T}_{0,m}\, c^{S_z}_{2,m}\right|}, \tag{4.7}$$

$$e_{\Delta T} = \frac{\sqrt{\left(c^{S_z}_{2,m}\, e_{0,m}\right)^2 + \left(c^{S_z}_{0,m}\, e_{2,m}\right)^2}}{\left|c^{S_z}_{0,m}\, c^{T}_{2,m} - c^{T}_{0,m}\, c^{S_z}_{2,m}\right|}, \tag{4.8}$$

where $e_{0,m}$ and $e_{2,m}$ represent the standard deviation of the relative frequency shift measurements of $R_{0,m}$ and $TR^{(1)}_{2,m}$ resonances, respectively. In the derivation of Eqs. 4.7 and 4.8, the uncertainty in the temperature and strain coefficients has

not been considered, and only the uncertainty related to the measurement of the frequency shift of the TAMRs has been accounted for.

Experimental results

TAMRs in an optical fiber were excited and interrogated using the setup depicted in Fig. 3.4, with an LPG written in the core of the fiber acting as the transducer. Measurements as a function of temperature were performed using a cooling-heating temperature chamber (WTB Binder MK 53), where the fiber section with the LPG was placed. The temperature of the experiments ranged from -20 °C to 80 °C, and the temperature inside the chamber was measured using a temperature meter (Di-LOG DL7102) with a temperature accuracy of 0.1 °C. Strain measurements were conducted by stretching the section of fiber with the LPG using a linear stage with a micrometer head. The strain response was measured within a range of $0-1.5$ mϵ, with a strain resolution of 10 μϵ. It is worth noting that the LPG itself exhibits sensitivity to changes in temperature and strain. Hence, to perform the characterization of the TAMRs with temperature and strain, the probe laser wavelength was tuned to track the LPG shift.

To obtain the temperature and strain coefficients for the $R_{0,m}$ and $TR^{(1)}_{2,m}$ resonances, we conducted two separate experiments. Firstly, we measured the resonances at various temperatures without any applied strain. Secondly, we measured the resonances at room temperature while varying the applied strain. Our analysis was limited to $R_{0,m}$ modes with $m > 3$ and $TR^{(1)}_{2,m}$ modes with $m > 10$. As shown in Figs. 4.3(a)-(d), the resonant frequencies of the TAMRs shifted towards higher frequencies as the temperature or strain was increased. Lorentzian curve fitting of the radio-frequency spectra enabled us to obtain accurate resonant frequencies due to the high Q values of the TAMRs ($> 2 \times 10^3$), with errors ranging from 50 to 300 Hz as the mode order increased.

Figs. 4.3(a)-(d) display the relative frequency shift $\Delta\Omega/\Omega$ of the $R_{0,10}$ and $TR^{(1)}_{2,15}$ resonances as a function of strain and temperature, respectively. The relative frequency shift of all the modes belonging to a specific family was found to be

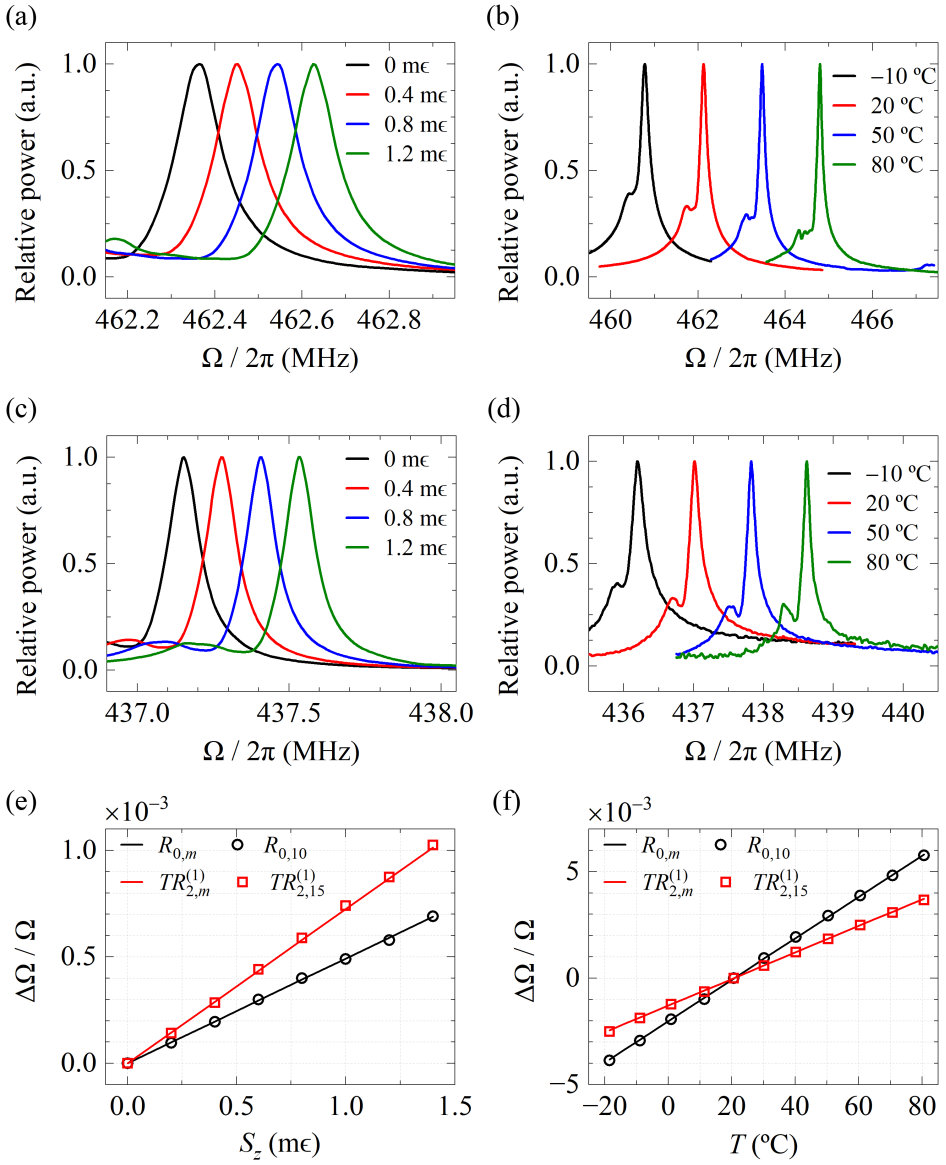

Figure 4.3: (a)-(d) Radio-frequency spectrum of a TAMR, for different values of strain and temperature. (a)-(b) $R_{0,10}$, (c)-(d) $TR^{(1)}_{2,15}$. (e)-(f) Relative frequency shift of TAMRs as a function of strain and temperature. Symbols are for experimental values of $R_{0,10}$ and $TR^{(1)}_{2,15}$ resonances. Solid lines show the linear fit of averaged values of $\Delta\Omega/\Omega$ over all the resonances of each family.

Table 4.1: Strain and temperature coefficients $c_{n,m}^{S_z,T}$ and inverse matrix $s_{n,m}^{S_z,T}$.

$c_{0,m}^{S_z}$ ($\mu\epsilon^{-1}$)	$c_{0,m}^{T}$ ($^{\circ}C^{-1}$)	$c_{2,m}^{S_z}$ ($\mu\epsilon^{-1}$)	$c_{2,m}^{T}$ ($^{\circ}C^{-1}$)
4.82×10^{-7}	9.73×10^{-5}	7.25×10^{-7}	6.24×10^{-5}
$s_{0,m}^{S_z}$ ($\mu\epsilon$)	$s_{0,m}^{T}$ ($^{\circ}C$)	$s_{2,m}^{S_z}$ ($\mu\epsilon$)	$s_{2,m}^{T}$ ($^{\circ}C$)
-0.154×10^{7}	0.179×10^{5}	0.240×10^{7}	-0.119×10^{5}

the same within the experimental error, in accordance with Eqs. 4.1 and 4.2. The solid line in Figs. 4.3(a)-(d) results from performing a linear fitting of the relative frequency shift values including all modes of the corresponding mode family. This property enables the use of the relative frequency shift average considering all modes of each family to determine ΔS_z and ΔT, thereby enhancing the accuracy of the measurements. The results of our calibration experiments are presented in Table 4.1, which includes the elements of the inverse matrix $s_{n,m}^{S_z,T}$ that can be used to determine the strain and temperature increments for a given measurement of the relative frequency shifts.

The temperature and strain accuracies can be estimated by considering the standard deviation of the relative frequency shift measurements and using Eqs. 4.7-4.8. After conducting repeated experiments and considering the characteristics of our measurement equipment, we estimate the uncertainty in the determination of frequency shift values $\Delta\Omega/2\pi$ to be better than 4 kHz. However, the standard deviation of the relative frequency shift $\Delta\Omega/\Omega$ measurements varies for different TAMRs and decreases with increasing frequency. Therefore, the sensor accuracy also vary slightly depending on the specific TAMR used to evaluate ΔS_z and ΔT. For instance, for the $R_{0,10}$ and $TR_{2,15}^{(1)}$ modes, the standard deviation of $\Delta\Omega/\Omega$ is around 9×10^{-6}, which leads to temperature and strain accuracies of approximately ± 0.2 °C and ± 25 $\mu\epsilon$, respectively. It is worth noting that higher order TAMRs improve the accuracy of strain and temperature estimation.

Table 4.2 presents a summary of the results obtained in this study, as well as a comparison with the performance of other methods reported in the literature

able to measure and discriminate between strain and temperature discrimination using optical fibers. Our results demonstrate figures of sensitivity and accuracy that are comparable to those reported in previous studies. However, further improvements could be made by optimizing the experimental setup and refining the frequency shift measurement procedure. It is worth to note that the present approach relies on measurements in the frequency domain, which offers several advantages over other methods based, for instance, on amplitude measurements, or spectral measurements in the optical domain. Specifically, this technique requires only a simple oscilloscope with a built-in fast Fourier transform, while other techniques may require more specialized electronic equipment or optical spectrum analyzers.

Table 4.2: Comparative of different techniques for discriminative measurement of strain and temperature using optical fibers.

Ref. / Technique	Strain / temperature range	Strain / temperature accuracy	Fiber length
Present work / FBS	0-1400 με / −20-80 °C	±25 με / ±0.2 °C	11 cm
[1] / Two superimposed FBGs	0-600 με / 10-60 °C	±10 με / ±5 °C	
[2] / FBG + LPG	290-1270 με / 25-50 °C	±9 με / ±1.5 °C	>3.5 cm
[3] / FBG in PANDA fiber	0-1100 με / 0-100 °C	±20 με / ±2 °C	
[4] / FBGs in undoped and boron doped fibers	0-1000 με / 30-130 °C	±18.4 με / ±2.2 °C	<15 mm
[5] / Laser-notched LPGs	0-1820 με / 20-200 °C	±21 με / ±0.3 °C	11.5 cm
[7] / Multiple bands in LPG	0-2100 με / 0-125 °C	±58 με / ±1 °C	
[8] / FBG in Hi-Bi fiber	0-4000 με / 30-70 °C	±60 με / ±6 °C	1 cm
[9] / Brillouin scatter. in PANDA fiber	0-1500 με / 10-70 °C	±3 με / ±0.08 °C	31 m
[10] / Brillouin scatter. + fluorescence in Er-doped fiber	0-4000 με / 30-100 °C	±300 με / ±4 °C	60 cm

4.3 High-accuracy measurement of Poisson's ratio

The accurate determination of Poisson's ratio (ν) in optical fibers has been a long-standing challenge for many years. Most reported values are for bulk silica, which significantly differs from experimental values obtained for silica optical fibers. Thus far, it was assumed that the value of ν falls within the range of 0.16 and 0.17, with an uncertainty of ± 0.01, corresponding to a relative error of 6% [18]. Accurate knowledge of Poisson's ratio and its dependence on magnitudes such as strain or temperature is crucial for two areas of research: the study of photo-elastic effects in optical fibers and the development of fiber sensors.

The uncertainty of Poisson's ratio is a limiting factor for the precision with which strain-optic coefficients were determined in the past [19], with relative errors of around 10% being common. Attempts to measure the chromatic dispersion of this coefficients in silica [20] are limited by the uncertainty of ν [19, 21]. The design and optimization of strain sensors based on fiber Bragg gratings also require accurate knowledge of Poisson's ratio and its dependence with strain and temperature. However, the accuracy of the Poisson's ratio has been a limiting factor in some instances. For example, in [22], values obtained for bulk silica with 10% error were used to model the response of a regenerated FBG. Similarly, while works on magnetic field sensors [23], geophysical applications [24], and fiber optic gyroscopes [25] assume a constant value for ν, they acknowledge the significance of strain and temperature effects.

Classical methods for determining ν in bulk samples of fused silica typically involve measuring both longitudinal and shear velocities. This can be accomplished through methods such as measuring the lower flexural and torsional frequencies of resonance [26] or using an ultrasonic pulse method with time detection [27]. While photo-elastic effects can also be utilized to evaluate ν in both bulk samples [20] and optical fibers [18, 19], the relatively high uncertainty of around 10% or higher limits their accuracy. These photo-elastic techniques typically combine interferometric and polarimetric measurements. We proposed

an alternative method based on FBS. Full characterization of TAMRs excited in the optical fiber, allows obtaining the Poisson's ratio with high accuracy, without requiring measurement of fiber dimensions. In the literature, we can find a low-accuracy attempt of exploiting torsional-radial acoustic resonances for this purpose in [28], but the use of only two resonances and their low Q factor results in an accuracy of only 10%. Here, we propose utilizing the complete spectrum of $R_{0,m}$ and $TR^{(1)}_{2,m}$ resonances. The key of the present technique is given by the fact that the Poisson's ratio depends on the ratio between the shear and the longitudinal acoustic velocities, $\alpha = V_S/V_L$,

$$\nu = \frac{1-2\alpha^2}{2(1-\alpha^2)}. \tag{4.9}$$

As described before, α can be obtained from the resonance frequencies of both series of modes, by combining the fitting results of the corresponding asymptotic expressions, Eqs. 4.4-4.5, to the experimental resonances.

Experimental results

To estimate the Poisson's ratio of an optical fiber and its dependence on temperature and strain, we utilized the same experimental setup as described in Section 4.2 for the strain-temperature sensor, employing the same narrowband LPG inscribed in an SM1500 (4.2/125) fiber. We chose this particular fiber for technical reasons related to the fabrication of the gratings in our laboratory facilities, but any single-mode optical fiber can be characterized with this method. TAMRs were excited via optical electrostriction by optical pump pulses and detected using the LPG and the probe wave. Temporal traces of the probe signal were recorded. We performed Fourier transforms of the temporal traces to obtain the RF spectrum and the resonant peaks for $R_{0,m}$ from $m = 5$ to $m = 23$ and $TR^{(1)}_{2,m}$ modes from $m = 12$ to $m = 28$, with errors ranging from 50 to 300 Hz. Experimental measurements were performed as a function of axial strain, in the range from 0 to 1.5 mϵ in steps of 10 μϵ, and as a function of temperatures, from -20 to 80 °C in steps of 5 °C.

At each value of strain/temperature, the experimental resonant frequencies of the $R_{0,m}$ and $TR^{(1)}_{2,m}$ modes were obtained, and then Eqs. 4.4 and 4.5 were fitted to the experimental data of the corresponding series. For room temperature (20 °C) and no applied strain, the results are depicted in Fig. 4.2, with the mentioned values for the ratio between acoustic velocities and radius of $V_L/a = (94\,463 \pm 6) \times 10^3$ s^{-1} and $V_S/a = (59\,345 \pm 9) \times 10^3$ s^{-1}. The experimental value of α is obtained by simply dividing both. Through these values and Eq. 4.9, a value of $\nu = 0.1740 \pm 0.0002$ at 20 °C was obtained. The uncertainty of the obtained value of ν corresponds to a relative error of 1.1‰. It is worth to note that the absolute error obtained by our method is about two orders of magnitude smaller than the

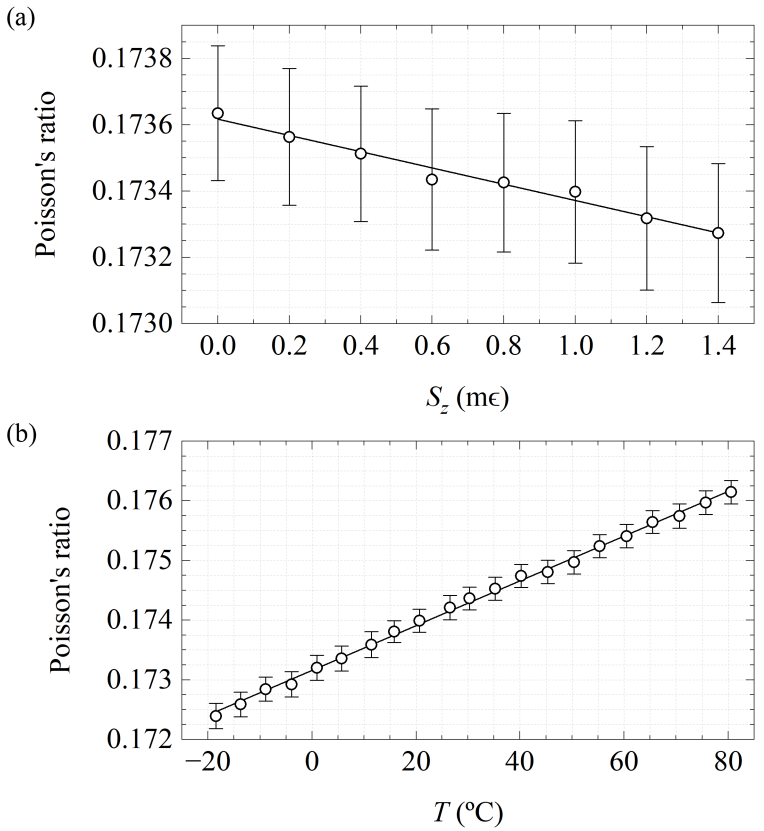

Figure 4.4: Poisson's ratio of the optical fiber used in the experiment as a function of (a) axial strain, and (b) temperature. Lines are best linear fit.

typically reported values. This accuracy is determined by the fact that no length measurements are required, the type of measurements required, the large Q factor of the acoustic resonances, and the good signal-to-noise ratio of the technique.

The resulting Poisson's ratio as a function of axial strain and temperature is shown in Figs. 4.4(a)-(b). Within the range of strain and temperature in our experiments, the Poisson's ratio exhibits a linear dependence on both magnitudes, decreasing with strain and increasing with temperature. The line of best fit was calculated in each case using the procedure described in [29], and we obtained,

$$\nu = (0.17362 \pm 1 \times 10^{-5}) + S_z\,[(-2.45 \pm 0.1) \times 10^{-7}], \tag{4.10}$$

$$\nu = (0.17316 \pm 2 \times 10^{-5}) + T\,[(3.76 \pm 0.04) \times 10^{-5}]\,^{\circ}\mathrm{C}^{-1}. \tag{4.11}$$

It is important to note that the Poisson's ratio estimation does not depend on the fiber radius, thus changes in fiber radius due to strain or thermal expansion do not affect the results. Table 4.3 presents a comparison between the Poisson's ratio of the optical fiber along with the corresponding temperature coefficient obtained from this study, and values reported in the literature for various techniques and samples, including both fused silica optical fibers and quartz bulk samples.

The dependence of the Poisson ratio with strain shown in Fig. 4.4(a) points out the nonlinear behavior of the elastic properties of silica. In the literature, one can find several studies of the non-Hookean behavior of silica [30–32]. However, references where specifically the strain coefficient of Poisson ratio is measured are scarce. In [33], Poisson ratio as a function of strain is reported, but measurements were performed for much large strain values than in this work.

Table 4.3: Comparative of Poisson's ratio and its temperature coefficient in silica optical fibers and bulk samples, obtained by different techniques.

Ref. / Technique	Sample	ν (at 20 °C)	$d\nu/dT$ (10^{-5}/K)
Present work / FBS ($R_{0,m}$ and $TR^{(1)}_{2,m}$)	Optical fiber SM1500	0.1740 ± 0.0002	3.76 ± 0.04
[18] / Interferometric measurement of photo-elastic effects	Optical fiber	0.17 ± 0.02	—
[19] / Interferometric and polarization measurements of photo-elastic effects	Optical fiber	0.154 ± 0.018^b	—
[27] / Ultrasonic pulse method	Bulk sample	0.1727 ± 0.0015^a	9.6 ± 0.2^a
[28] / FBS ($TR_{2,5}$ and $TR_{2,7}$)	Optical fiber	0.17^b	—
[20] / Interferometric measurement of photo-elastic effects	Bulk sample	0.164^b	—
[26] / Measurement of flexural and torsional resonances	Bulk sample	0.165 ± 0.017^b	4.0

[a] Values derived from Fig. 3 in Ref. [27] in the temperature range [-20, 80] °C

[b] Measurements at room temperature

References

[1] M. G. Xu, J.-L. Archambault, L. Reekie, and J. P. Dakin, "Discrimination between strain and temperature effects using dual-wavelength fiber grating sensors", *Electronics Letters*, vol. 30, no. 13, pp. 1085–1087, 1994.

[2] H. Patrick, G. Williams, A. Kersey, J. Pedrazzani, and A. Vengsarkar, "Hybrid fiber Bragg grating/long period fiber grating sensor for strain/temperature discrimination", *IEEE Photonics Technology Letters*, vol. 8, no. 9, pp. 1223–1225, 1996.

[3] M. Sudo, M. Nakai, K. Himeno, S. Suzaki, A. Wada, and R. Yamauchi, "Simultaneous measurement of temperature and strain using PANDA fiber grating", EN, in *12th International Conference on Optical Fiber Sensors (1997), paper OWC7*, Optica Publishing Group, 1997, OWC7.

[4] P. Cavaleiro, F. Araujo, L. Ferreira, J. Santos, and F. Farahi, "Simultaneous measurement of strain and temperature using Bragg gratings written in germanosilicate and boron-codoped germanosilicate fibers", *IEEE Photonics Technology Letters*, vol. 11, no. 12, pp. 1635–1637, 1999.

[5] H. Zeng *et al.*, "Combining two types of gratings for simultaneous strain and temperature measurement", *IEEE Photonics Technology Letters*, vol. 28, no. 4, pp. 477–480, 2016.

[6] Y. Kim, Y. W. Lee, and B. Lee, "Simultaneous measurement of strain and temperature using phase-shifted long-period grating written on polarization-maintaining fiber", in *Optical Fiber Sensors (2006), paper TuE82*, Optica Publishing Group, 2006, TuE82.

[7] V. Bhatia, D. Campbell, R. O. Claus, and A. M. Vengsarkar, "Simultaneous strain and temperature measurement with long-period gratings", *Optics Letters*, vol. 22, no. 9, pp. 648–650, 1997.

[8] S. T. Oh, W. T. Han, U. C. Paek, and Y. Chung, "Discrimination of temperature and strain with a single FBG based on the birefringence effect", *Optics Express*, vol. 12, no. 4, pp. 724–729, 2004.

[9] W. Zou, Z. He, and K. Hotate, "Complete discrimination of strain and temperature using Brillouin frequency shift and birefringence in a polarization-maintaining fiber", *Optics Express*, vol. 17, no. 3, pp. 1248–1255, 2009.

[10] M. Ding, Y. Mizuno, and K. Nakamura, "Discriminative strain and temperature measurement using Brillouin scattering and fluorescence in erbium-doped optical fiber", *Optics Express*, vol. 22, no. 20, pp. 24 706–24 712, 2014.

[11] Y. Weng, E. Ip, Z. Pan, and T. Wang, "Single-end simultaneous temperature and strain sensing techniques based on Brillouin optical time domain reflectometry in few-mode fibers", *Optics Express*, vol. 23, no. 7, pp. 9024–9039, 2015.

[12] Y. Antman, A. Clain, Y. London, and A. Zadok, "Optomechanical sensing of liquids outside standard fibers using forward stimulated Brillouin scattering", *Optica*, vol. 3, no. 5, p. 510, 2016.

[13] D. M. Chow and L. Thévenaz, "Forward Brillouin scattering acoustic impedance sensor using thin polyimide-coated fiber", *Optics Letters*, vol. 43, no. 21, p. 5467, 2018.

[14] D. M. Chow, Z. Yang, M. A. Soto, and L. Thévenaz, "Distributed forward Brillouin sensor based on local light phase recovery", *Nature communications*, vol. 9, no. 1, pp. 1–9, 2018.

[15] G. Bashan, H. H. Diamandi, Y. London, E. Preter, and A. Zadok, "Optomechanical time-domain reflectometry", en, *Nature Communications*, vol. 9, no. 1, p. 2991, 2018.

[16] C. Pang *et al.*, "Opto-mechanical time-domain analysis based on coherent forward stimulated Brillouin scattering probing", en, *Optica*, vol. 7, no. 2, p. 176, 2020.

[17] Z. Han, N. Zhao, Z. Yang, and G. Li, "Error analyses for simultaneous measurement of temperature and strain based on polarization-maintaining few-mode fibers", in *2018 Asia Communications and Photonics Conference (ACP)*, Hangzhou, China: IEEE, 2018, pp. 1–3.

[18] F. El-Diasty, "Multiple-beam interferometric determination of Poisson's ratio and strain distribution profiles along the cross section of bent single-mode optical fibers", *Applied Optics*, vol. 39, no. 19, pp. 3197–3201, 2000.

[19] A. Bertholds and R. Dandliker, "Determination of the individual strain-optic coefficients in single-mode optical fibres", *Journal of Lightwave Technology*, vol. 6, no. 1, pp. 17–20, 1988.

[20] W. Primak and D. Post, "Photoelastic constants of vitreous silica and its elastic coefficient of refractive index", *Journal of Applied Physics*, vol. 30, no. 5, pp. 779–788, 1959.

[21] X. Roselló-Mechó, M. Delgado-Pinar, A. Díez, and M. V. Andrés, "Measurement of Pockels' coefficients and demonstration of the anisotropy of the elasto-optic effect in optical fibers under axial strain", *Optics Letters*, vol. 41, no. 13, pp. 2934–2937, 2016.

[22] M. Lindner *et al.*, "Transition from purely elastic to viscoelastic behavior of silica optical fibers at high temperatures characterized using regenerated Bragg gratings", *Optics Express*, vol. 28, no. 5, pp. 7323–7340, 2020.

[23] Y. Shi, Y. Ma, and Y. Wang, "Magneto-elastic-optical coupling of Terfenol-D based optical fiber magnetic field sensors", en, *Materials Research Express*, vol. 6, no. 8, p. 086 106, 2019.

[24] S. DeWolf, F. K. Wyatt, M. A. Zumberge, and W. Hatfield, "Improved vertical optical fiber borehole strainmeter design for measuring Earth strain", *Review of Scientific Instruments*, vol. 86, no. 11, p. 114 502, 2015.

[25] Z. Zhang and F. Yu, "Quantitative analysis for the effect of the thermal physical property parameter of adhesive on the thermal performance of the quadrupolar fiber coil", *Optics Express*, vol. 25, no. 24, pp. 30 513–30 525, 2017.

[26] S. Spinner, "Elastic moduli of glasses at elevated temperatures by a dynamic method", *Journal of the American Ceramic Society*, vol. 39, no. 3, pp. 113–118, 1956.

[27] M. Fukuhara, A. Sanpei, and K. Shibuki, “Low temperature-elastic moduli, debye temperature and internal dilational and shear frictions of fused quartz”, *Journal of Materials Science*, vol. 32, no. 5, pp. 1207–1211, 1997.

[28] K. Shiraki and M. Ohashi, “Sound velocity measurement based on guided acoustic-wave Brillouin scattering”, *IEEE Photonics Technology Letters*, vol. 4, no. 10, p. 1177, 1992.

[29] D. York, N. M. Evensen, M. L. Martínez, and J. De Basabe Delgado, “Unified equations for the slope, intercept, and standard errors of the best straight line”, *American Journal of Physics*, vol. 72, no. 3, pp. 367–375, 2004.

[30] F. Ernsberger, D. Uhlmann, and N. Kreidl, “Elastic properties of glasses”, in *Glass Science and Technology*. Elsevier, 1980, vol. 5, pp. 1–19.

[31] J. T. Krause, L. R. Testardi, and R. N. Thurston, “Deviations from linearity in the dependence of elongation upon force for fibres of simple glass formers and of glass optical lightguides”, *Physics and Chemistry of Glasses*, vol. 20, no. 6, 1979.

[32] P. K. Gupta and C. R. Kurkjian, “Intrinsic failure and non-linear elastic behavior of glasses”, *Journal of Non-Crystalline Solids*, vol. 351, no. 27, pp. 2324–2328, 2005.

[33] M. Guerette, C. R. Kurkjian, S. Semjonov, and L. Huang, “Nonlinear elasticity of silica glass”, *Journal of the American Ceramic Society*, vol. 99, no. 3, T. Rouxel, Ed., pp. 841–848, 2016.

5 | Conclusions

This thesis compiles our main contributions in relation to the forward Brillouin scattering phenomenon in optical fibers. The study was divided into two main topics. Firstly, novel methods for detecting FBS and characterizing transverse acoustic mode resonances were demonstrated. We showed that fiber gratings can be very efficient in-fiber transducers to convert elastic perturbations into intensity variations of an optical signal. The use of whispering gallery mode resonances supported by the optical fiber itself provided complementary perspectives, enabling a comprehensive and full characterization of TAMRs in optical fibers. Secondly, based on these measurement methods, and on deep understanding of the physics involved in FBS, applications related to fiber sensing and optical fiber characterization were explored. These included the development of a strain-temperature discriminative sensor and the characterization of elastic properties of optical fibers, in particular, high accuracy Poisson's ratio in optical fibers, as well as its dependence on the mentioned magnitudes.

In Chapter 2, we presented a theoretical framework to describe the properties of TAMRs in optical fibers, along with their interaction with different optical waves supported by the fiber. We examined the various elastic modes that an optical fiber can withstand, solving the elastic wave equation. We focus on TAMRs, specifically on two particular series of TAMRs, which are radial modes $R_{0,m}$ and torsional-radial modes $TR_{2,m}$ that can be optically excited through the electrostriction force induced by the fundamental optical fiber mode. Additionally, we explored the different sources of acoustic dissipation, and we discussed with particular emphasis the different contributions that dominates acoustic dissipation in short fiber sections, in line with our experiments. Finally, we studied the photo-elastic changes in the propagation properties of optical guided modes in

the fiber caused by the perturbation induced by TAMRs in the dielectric tensor.

Chapter 3 introduced novel characterization techniques for forward Brillouin scattering in optical fibers. The methods rely on a pump-and-probe scheme where the mechanical stresses generated in the fiber by the oscillation of TAMRs were effectively converted into optical power modulation, which could be conveniently measured using a common photodetector. Compared to previous FBS detection methods that relied on phase modulation of a probe wave in large fiber sections, the newly introduced techniques require very short fiber sections of a few centimeters or less to achieve a significant signal-to-noise ratio in the interrogation of TAMRs.

Firstly, we proposed the use of long-period gratings and fiber Bragg gratings acting as acousto-optic transducer for measuring TAMRs, based on the photoelastic perturbation of the fiber grating. These devices provided a measurement of the effect of TAMRs on the fiber core, similar to the previously mentioned interferometric techniques, but with higher sensitivity due to its resonant nature. With the use of LPGs, we found that the linewidth of the acoustic resonances was shorter than in previous reports due to the short fiber section required by the present method, which significantly reduced the contribution of structural inhomogeneities to linewidth broadening. We were able to measure core effective index changes as small as 10^{-9} for pump pulses of 10 W peak power, still achieving a signal-to-noise ratio over 15 dB. By increasing the pump power, we could improve the SNR up to 40 dB. FBGs yielded similar results than LPGs with lower sensitivity and a more complex response. However, FBGs may have some potential advantages as they are not sensitive to changes in the surrounding medium.

Secondly, we demonstrated how the interplay between optical and acoustic resonances can be exploited to study and characterize TAMRs in optical fibers. Optical whispering-gallery modes are highly sensitive to changes in both, the refractive index and fiber geometry. The perturbation caused by radial acoustic resonances leads to modulation of the WGM resonant wavelength. By monitoring

the WGM resonances, we efficiently interrogated and detected $R_{0,m}$ modes. Additionally, we demonstrated that WGMS are insensitive to torsional-radial $TR_{2,m}$ acoustic modes. Complete characterization of $R_{0,m}$ modes was achieved using this technique. Our experimental results indicated that both the geometric and photoelastic perturbations caused by TAMRs contribute similarly to the modulation of WGMs. The low-order $R_{0,m}$ modes, which generate a significant modulation of the WGMs, could be accurately probed using this method, while they were difficult to be detected using previously reported probing techniques based on reading the core perturbations. The linewidths of the acoustic resonances obtained using this method were about 25% shorter than those achieved with the LPG. This feature may be attributed to further dissipation reduction as fiber inhomogeneities contribution becomes negligible. Up to our knowledge, this method has provided the narrowest acoustic resonances reported in the literature to date.

Chapter 4 presented various applications of FBS in optical fibers related with sensing and fiber characterization. The focus of previous studies reported in the literature regarding FBS-based applications has mainly been on the use of either $R_{0,m}$ or $TR_{2,m}$ acoustic resonances. However, we have shown that the potential capabilities of TAMRs can be further enhanced by combining the characteristics and response of both type of acoustic modes. Additionally, we derived accurate and simple asymptotic expressions for the resonance frequency of TAMRs, which allowed the proper characterization of $TR_{2,m}$ modes and simplifies dramatically the procedures to obtain physical information of the fiber from the experimental recordings. Furthermore, the techniques developed in this thesis allowed for point-measurements with high accuracy.

In the first place, we demonstrated a strain-temperature discriminative sensor that utilized the distinct sensitivity of radial $R_{0,m}$ resonances and torsional-radial $TR^{(1)}_{2,m}$ series of resonances to changes in strain and temperature. By calibrating the frequency shift of each type of TAMR against strain and temperature, we showed that the relative frequency shift is the same for all modes of a given series. With our experimental setup and frequency measurement procedure, we

estimated and demonstrated that strain and temperature can be measured simultaneously with an accuracy better than ± 25 με and ± 0.2 °C, respectively. The use of high-Q acoustic resonances and frequency encoding of the signal contribute to the accuracy of this approach, which is comparable to common wavelength multiplexing techniques using LPG and FBG.

In the second place, a technique based on TAMRs has been developed for the characterization of elastic properties of optical fibers. In particular, we demonstrate accurate measurement of the Poisson's ratio in optical fibers. This method does not requires any length measurements, it relies on radio-frequency measurements, and takes into account the experimental information provided by both $R_{0,m}$ and $TR^{(1)}_{2,m}$ resonances. The derived algebraic asymptotic expressions are used to calculate the resonance frequencies of both types of resonances, allowing for accurate fittings of the experimental data. The technique has been successfully applied to silica optical fibers, yielding a Poisson's ratio with an estimated relative error lower than 1‰. The high precision of this technique enabled the investigation of the dependence of the fiber Poisson's ratio on strain and temperature. Results showed that the Poisson's ratio decreases linearly with strain at a rate of -2.45×10^{-7} and increases linearly with temperature at a rate of $3.76 \times 10^{10-5}$ °C^{-1}. While the method has been applied to silica optical fibers, it can potentially be applied to fibers based on other materials. Furthermore, the method can be extended to measure other elastic properties of optical fibers.

The FBS point measurement and characterization techniques described in this thesis, as well as the demonstrated applications, show a great potential based on the high signal-to-noise ratio and narrow linewidhts obtained. Wavelength-multiplexed point sensors can serve as a promising substitute for classical FBS-distributed sensing, which involves more intricate experimental arrangements and signal processing compared to point sensors. The current limitation in fiber coating for FBS-distributed sensors has made wavelength-multiplexed point sensors with only short sections of uncoated fiber a more practical choice. Besides, sensors that rely on measuring the linewidth of the acoustic resonances and are

based on changes in the acoustic impedance of the outer fiber medium will benefit from the narrow linewidths reported in this thesis, enabling lower detection limits and improving the sensitivity of the sensor. The advancements mentioned above are likely to accelerate the progress of environmental sensing and biosensing applications. However, there is a need for further research in the area of long-range sensing and harsh conditions, as these aspects have not been thoroughly explored yet. Future development should focus on addressing these gaps and developing solutions that can operate effectively under challenging conditions.

A | Asymptotic expressions for TAMRs

In section 2.2, the characteristics equations for radial $R_{0,m}$ and torsional-radial $TR_{2,m}$ modes are derived. Numerical solution of such equations are required to obtain the resonance frequency of the acoustic modes resonances. These characteristic equations involve Bessel functions of the first kind.

We can obtain simple approximated expressions for the cutoff frequencies by analyzing the asymptotic behavior of the Bessel functions. When the argument is such that $|z| \to \infty$ and $|\arg(z)| < \pi$, we can use the Hankel's asymptotic expansion to approximate the Bessel functions of the first kind [1],

$$J_n(z) \sim \sqrt{\frac{2}{\pi z}} \left[P(n,z) \cos\left(z - \frac{n\pi}{2} - \frac{\pi}{4}\right) - Q(n,z) \sin\left(z - \frac{n\pi}{2} - \frac{\pi}{4}\right) \right], \tag{A.1}$$

where

$$P(n,z) = \sum_{k=0}^{\infty} (-1)^k \frac{(n,2k)}{(2z)^{2k}}, \tag{A.2}$$

$$Q(n,z) = \sum_{k=0}^{\infty} (-1)^k \frac{(n,2k+1)}{(2z)^{2k+1}}, \tag{A.3}$$

and

$$(n,2k) = \frac{\Gamma(n+k+1/2)}{k!\,\Gamma(n-k+1/2)}, \tag{A.4}$$

where Γ is the gamma function. It we truncate the series in Eqs. A.2 and A.3 to retain the terms proportional to z^0 and z^{-1}, we obtain the following approximated

expressions for J_0, J_2 and J_3,

$$J_0(z) \sim \sqrt{\frac{2}{\pi z}}\left[\cos\left(z-\frac{\pi}{4}\right)+\frac{1}{8z}\sin\left(z-\frac{\pi}{4}\right)\right], \tag{A.5}$$

$$J_2(z) \sim \sqrt{\frac{2}{\pi z}}\left[-\cos\left(z-\frac{\pi}{4}\right)+\frac{15}{8z}\sin\left(z-\frac{\pi}{4}\right)\right], \tag{A.6}$$

$$J_3(z) \sim \sqrt{\frac{2}{\pi z}}\left[\cos\left(z+\frac{\pi}{4}\right)+\frac{35}{8z}\sin\left(z+\frac{\pi}{4}\right)\right]. \tag{A.7}$$

The characteristic equation for the radial resonances $R_{0,m}$ of an elastic cylinder of radius a is given by,

$$\left(1-\alpha^2\right)J_0(\alpha\zeta)-\alpha^2 J_2(\alpha\zeta)=0. \tag{A.8}$$

where $\zeta=\Omega a/V_S$ and $\alpha=V_S/V_L$. We can take the approximated Eqs. A.5 and A.6 for J_0 and J_2 to Eq. A.8, and after some manipulations, we obtain,

$$\cot\left(\alpha\zeta-\frac{\pi}{4}\right)\approx\frac{16\alpha^2-1}{8\alpha\zeta}. \tag{A.9}$$

For large values of ζ, the right-hand term in Eq. A.9 tends to zero. We can use a first order Taylor expansion of the function $f(\alpha\zeta)=\cot(\alpha\zeta-\pi/4)$ to further reduce the expression. Zeroes of the cotangent function are given by $\alpha\zeta_m-\pi/4=m\pi-\pi/2$ for $m=1,2,3,\ldots$. Thus,

$$f(\alpha\zeta_m)=\cot\left(\alpha\zeta_m-\frac{\pi}{4}\right)=0, \tag{A.10}$$

and the first derivative,

$$f'(\alpha\zeta_m)=-\frac{1}{\sin^2\left(\alpha\zeta_m-\frac{\pi}{4}\right)}=-1, \tag{A.11}$$

Then, we can approximate the left-hand term of Eq. A.9 with a first order Taylor

expansion,

$$f(\alpha\zeta) \approx f(\alpha\zeta_m) + f'(\alpha\zeta_m)(\alpha\zeta - \alpha\zeta_m) = -\left(\alpha\zeta - m\pi + \frac{\pi}{4}\right), \qquad \text{(A.12)}$$

Taking this back to Eq. A.9 and approximating the term $\alpha\zeta$ in the denominator of the right-hand side by $\alpha\zeta_m = m\pi - \pi/4$, we obtain the following expression,

$$\alpha\zeta_{0,m} \approx c_m - \frac{16\alpha^2 - 1}{8c_m}, \qquad \text{(A.13)}$$

where $c_m = m\pi - \pi/4$. This analytical expression provides approximate values for the resonance frequency of the radial $R_{0,m}$ modes. To evaluate the accuracy of Eq. (A.12), we compare the resonance frequency of $R_{0,m}$ modes of an optical fiber calculated by numerical solutions of Eq. A.8 and by Eq. A.13. The relative difference is shown in A.1. This approximation is justified as the relative error committed with respect to the exact solution of Eq. A.8 is less than one part per thousand for $m \geq 2$.

The characteristic equation of the torsional-radial mode resonances $TR_{2,m}$ is

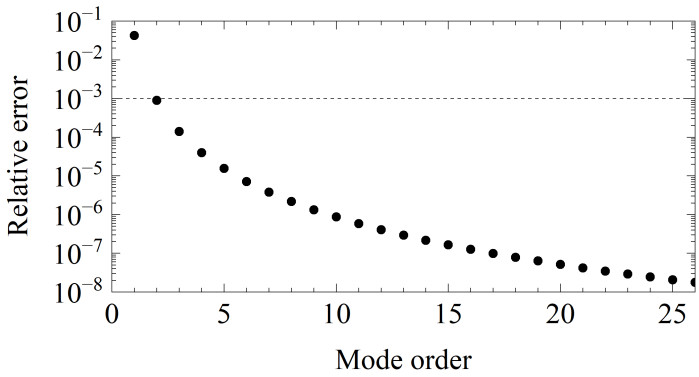

Figure A.1: Relative error of ζ for $\alpha = 0.63$ between the exact and approximated equations for $R_{0,m}$ resonances.

given by,

$$\begin{vmatrix} \left(3-\zeta^2/2\right)J_2(\alpha\zeta) & \left(6-\zeta^2/2\right)J_2(\zeta)-3\zeta J_3(\zeta) \\ J_2(\alpha\zeta)-\alpha\zeta J_3(\alpha\zeta) & \left(2-\zeta^2/2\right)J_2(\zeta)+\zeta J_3(\zeta) \end{vmatrix} = 0. \tag{A.14}$$

This equation can be rewritten in the following form,

$$J_2(\zeta)J_2(\alpha\zeta) = \Delta, \tag{A.15}$$

$$\Delta = \frac{\left[\left(6-\frac{\zeta^2}{2}\right)J_2(\zeta)-3\zeta J_3(\zeta)\right]\left[J_2(\alpha\zeta)-\alpha\zeta J_3(\alpha\zeta)\right]}{\left(3-\frac{\zeta^2}{2}\right)\left(2-\frac{\zeta^2}{2}\right)}, \tag{A.16}$$

In a first-order approximation, the term Δ can be approached to zero. We will demonstrate later that the dominant term of this expression is proportional to ζ^{-2}. In such a case, we see from Eq. A.15 that there are two series of $TR_{2,m}$ modes, the first one whose cutoff frequencies are determined by the zeroes of $J_2(\zeta)$ and the second by the zeroes of $J_2(\alpha\zeta)$, assuming that there are no degenerated resonances. The first series is denoted as $TR^{(1)}_{2,m}$ and the second as $TR^{(2)}_{2,m}$. By using Eq. A.6 to approximate $J_2(\zeta)$ in Eq. A.15, we obtain,

$$\cot\left(\zeta-\frac{5\pi}{4}\right) \approx \frac{15}{8\zeta}+\frac{\Delta}{\sin\left(\zeta-\frac{5\pi}{4}\right)J_2(\alpha\zeta)}. \tag{A.17}$$

As we assume $\Delta \approx 0$, and the first term of the right-hand side tends to zero for large values of ζ, we can apply a Taylor expansion for the cotangent function in a similar way as for the previous case of radial resonances. Now, the zeroes for the cotangent are $\zeta_m - 5\pi/4 = m\pi - \pi/2$ for $m = 1,2,3,\ldots$.

By evaluating the Δ term in A.17 at ζ_m using Eqs. A.6 and A.9 to approximate $J_2(\zeta)$ and $J_3(\zeta)$, we obtain,

$$\frac{\Delta}{(-1)^m J_2(\alpha\zeta_m)} \approx \frac{\left[-\left(6-\frac{\zeta_m^2}{2}\right)\frac{15}{8\zeta_m}-3\zeta_m\right]\left[J_2(\alpha\zeta_m)-\alpha\zeta_m J_3(\alpha\zeta_m)\right]}{\left(3-\frac{\zeta_m^2}{2}\right)\left(2-\frac{\zeta_m^2}{2}\right)J_2(\alpha\zeta_m)} \tag{A.18}$$

For large ζ_m we can approximate the expressions in parenthesis to $-\zeta_m^2/2$. If we also approximate $J_2(\alpha\zeta)$ and $J_3(\alpha\zeta)$) using Eqs. A.6 and A.9, we have,

$$\frac{\Delta}{(-1)^m J_2(\alpha\zeta_m)} \approx \frac{33}{4}\left[\frac{J_3(\alpha\zeta_m)}{J_2(\alpha\zeta_m)}\frac{\alpha}{\zeta_m^2} - \frac{1}{\zeta_m^3}\right] \approx \frac{33}{4}\left[\tan\left(\alpha\zeta_m - \frac{5\pi}{4}\right)\frac{\alpha}{\zeta_m^2} - \frac{1}{\zeta_m^3}\right], \tag{A.19}$$

which does not contain terms proportional to ζ_m^0 and ζ_m^{-1}, as noted earlier. In addition, this is fulfilled for $J_2(\alpha\zeta) \neq 0$, which states that the resonances of both series are not degenerated.

The approximated expression for the cutoff frequencies of the $TR_{2,m}^{(1)}$ resonances is given by,

$$\zeta_{2,m}^{(1)} \approx c_{m+1} - \frac{15}{8c_{m+1}}, \tag{A.20}$$

where $c_m = m\pi - \pi/4$. We can perform a similar procedure for the $TR_{2,m}^{(2)}$ series of resonances. In this case, we obtain the following expression,

$$\alpha\zeta_{2,m}^{(2)} \approx c_{m+1} - \frac{15}{8c_{m+1}}. \tag{A.21}$$

Figure A.2 shows the relative error introduced when calculating the cutoff frequency of both series of torsional-radial resonances in this approximation. As it

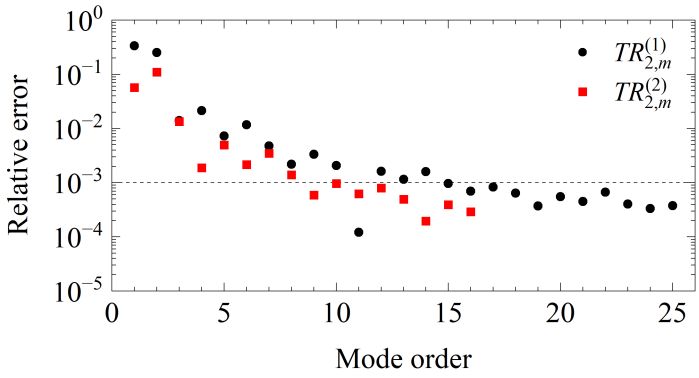

Figure A.2: Relative error of ζ for $\alpha = 0.63$ between the exact and approximated equations for $TR_{2,m}^{(1)}$ and $TR_{2,m}^{(2)}$ resonances.

can be seen, this approximation is not as accurate as the corresponding derived in the case of $R_{0,m}$. Nevertheless, the relative error decreases as the mode order increases, reaching values below one part per thousand for $m = 15$ in the case of $TR_{2,m}^{(1)}$ and $m = 10$ in the case of $TR_{2,m}^{(2)}$.

References

[1] M. Abramowitz and I. A. Stegun, *Handbook of Mathematical Functions with Formulas, Graphs, and Mathematical Tables*. New York: Dover, 1964.

B | Analysis of coupling to an oscillating microresonator

In this appendix, we study the excitation of a high-Q whispering-gallery mode of an oscillating optical microresonator, i.e. the optical fiber, by a propagating wave in an evanescent wave coupler. In the context of this thesis, oscillation of the microresonator is given by the presence of an $R_{0,m}$ acoustic resonance in the fiber. As described in Chapter 2, an $R_{0,m}$ resonance change the refractive index and the dimensions of the resonator, resulting in a variation of the WGM frequency. In the case of a slowly varying field amplitude, the optical fields obey the following equations [1],

$$\frac{d}{dt}A_{MR}(t) + \left[\frac{\omega}{2Q} - j\Delta\omega(t)\right]A_{MR}(t) = j\sqrt{\frac{\omega}{\tau Q_{ext}}}A_{in}, \tag{B.1}$$

$$A_{out}(t) = \sqrt{1 - \frac{\tau\omega}{Q_{ext}}}A_{in} + j\sqrt{\frac{\tau\omega}{Q_{ext}}}A_{MR}(t), \tag{B.2}$$

where A_{in}, $A_{MR}(t)$ and $A_{out}(t)$ are the normalized amplitudes of the input field, the field inside the microresonator, and the output (transmitted) field. Figure B.1(a) shows a scheme of the coupling system. Q is the total quality factor which is comprised of two contributions $1/Q = 1/Q_0 + 1/Q_{ext}$. Q_0 is related to the cavity decay rate $\kappa_0 = \omega/(2Q_0)$ due to inherent radiation of the field inside the microresonator, while Q_{ext} is related to the coupling rate $\kappa_{ext} = \eta^2/(2\tau) = \omega/(2Q_{ext})$ between the coupler and the cavity. η is the coupling coefficient, τ is the photon round-trip time in the cavity and ω is the frequency of the optical field. $\Delta\omega(t)$ is the detuning between the frequency of the optical field and the resonant frequency of the WGM. For an harmonic oscillation of frequency Ω,

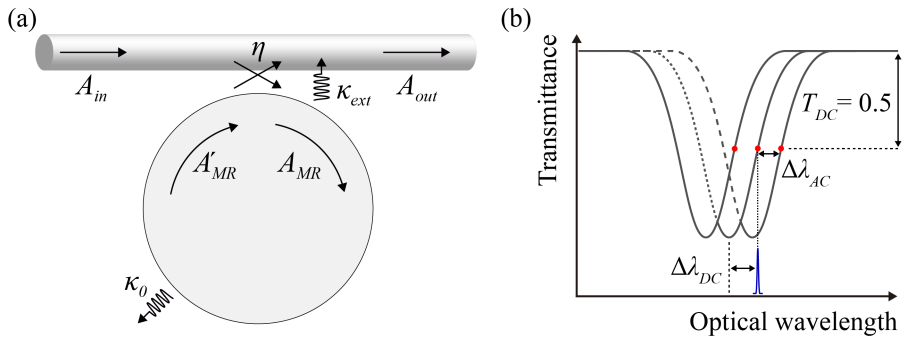

Figure B.1: (a) Scheme of the coupling system. (b) Diagram illustrating the detuning parameters.

we can express the detuning as,

$$\Delta\omega(t) = \Delta\omega_{DC} + \Delta\omega_{AC}\cos(\Omega t), \tag{B.3}$$

where $\Delta\omega_{DC} = \omega - \omega_0$ is the detuning in the absence of oscillation and $\Delta\omega_{AC}$ is the amplitude of the oscillating detuning. The output power transmittance is given by $T(t) = |A_{out}(t)/A_{in}|^2$, and can be expressed as the sum of a transient term $T_{tr}(t)$ and a steady-state term $T_{st}(t)$. When the frequency of the input light matches one of the edges or the WGM spectrum, we can assume that, for small perturbations, the steady-term response can also be expressed as the sum of DC and AC components,

$$T_{st}(t) \approx T_{DC} + \Delta T_{AC}\cos(\Omega t), \tag{B.4}$$

where T_{DC} is the steady-state transmittance when there is no perturbation of the cavity frequency and ΔT_{AC} is the amplitude of the transmittance modulation due to the perturbation. Figure B.2 shows an illustrative example of the optical power transmittance when solving numerically Eqs. B.1-B.2.

In addition to the strength of the perturbation determined by $\Delta\omega_{AC}$, the amplitude ΔT_{AC} will depend on the Q factor of the WGM and the perturbation frequency Ω. To study the interplay between these magnitudes with more detail, we can solve

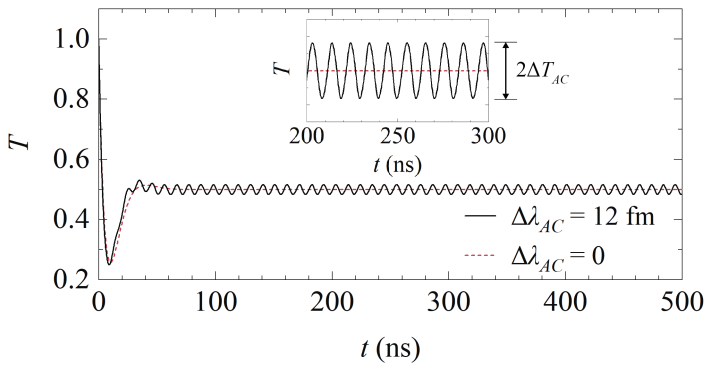

Figure B.2: Optical power transmittance as a function of time for a representative case. The inset shows the steady-state regime. Parameters: $Q_0 = Q_{ext} = 10^7$, $\lambda = 1.5$ µm, $\tau = 1.9$ ps, $\Delta\lambda_{DC} = 150$ fm, $\Delta\lambda_{AC} = 12$ fm, $\Omega = 2\pi \times 100$ MHz. The red dashed line is the calculation for the static case $\Delta\lambda_{AC} = 0$.

analytically Eqs. B.1-B.2 for the steady-state term $T_{st}(t)$. For high visibility resonances ($Q_0 = Q_{ext} = Q$) and a detuning ω_{DC} adjusted to obtain $T_{DC} = 0.5$, we obtain,

$$T_{st}(t) \approx \frac{1}{2}\left|1 - \frac{\Delta\omega_{AC}}{\sqrt{\Omega^2 - j2(\omega/2Q)^2}}\cos(\Omega t + \phi)\right|^2. \tag{B.5}$$

We see that, at low frequencies ($\Omega \to 0$), the sensitivity of the technique $\Delta T_{AC}/\Delta\omega_{AC} \approx Q/\omega$, i.e., is proportional to the quality factor of the WGM and it is essentially determined by the slope of the WGM transmission spectrum $\partial T_{DC}/\partial\Delta\omega_{DC}$. At high frequencies ($\Omega \to \infty$), the sensitivity is $\Delta T_{AC}/\Delta\omega_{AC} \approx 1/\Omega$, i.e., the transmittance response of the WGM is attenuated for high frequencies. This correspond to a low-pass filter response, as depicted in Fig. 3.15.

The cutoff frequency of the transmittance response in Eq. B.5 is driven by the complex pole $\Omega = (1 \pm j)\omega/2Q$ which determines that $\Omega_{cutoff} \approx \omega/\sqrt{2}Q$, which is inversely proportional to the quality factor (see Fig. 3.15). The cavity lifetime, defined as $\tau_{lifetime} = Q/\omega$, determines the low and high frequency regimes when $T_\Omega >> \tau_{lifetime}$ and $T_\Omega << \tau_{lifetime}$, respectively, being $T_\Omega = 2\pi/\Omega$ the period of the perturbation with frequency Ω.

References

[1] M. L. Gorodetsky and V. S. Ilchenko, “Optical microsphere resonators: Optimal coupling to high-Q whispering-gallery modes”, en, *Journal of the Optical Society of America B*, vol. 16, no. 1, p. 147, 1999.

List of publications

Articles in journals

- L. A. Sánchez, A. Díez, J. L. Cruz, and M. V. Andrés, "Efficient interrogation method of forward Brillouin scattering in optical fibers using a narrow bandwidth long-period grating", *Optics Letters*, vol. 45, no. 19, p. 5331, 2020.

- L. A. Sánchez, C. Cuadrado-Laborde, A. Carrascosa, A. Díez, J. L. Cruz, and M. V. Andrés, "Low-repetition-rate all-polarization maintaining thulium-doped passively modelocked fiber laser", *Optics and Laser Technology*, vol. 149, p. 107 856, 2022.

- L. A. Sánchez, A. Díez, J. L. Cruz, and M. V. Andrés, "Strain and temperature measurement discrimination with forward Brillouin scattering in optical fibers", *Optics Express*, vol. 30, no. 9, p. 14 384, 2022.

- L. A. Sánchez, A. Díez, J. L. Cruz, and M. V. Andrés, "High accuracy measurement of Poisson's ratio of optical fibers and its temperature dependence using forward-stimulated Brillouin scattering", *Optics Express*, vol. 30, no. 1, p. 42, 2022.

- L. A. Sánchez, A. Díez, J. L. Cruz, and M. V. Andrés, "Recent advances in forward Brillouin scattering: Sensor applications", *Sensors*, vol. 23, no. 1, p. 318, 2022.

- L. A. Sánchez, M. Delgado-Pinar, A. Díez, J. L. Cruz, and M. V. Andrés, "Forward Brillouin scattering spectroscopy in optical fibers with whispering-gallery modes", Manuscript submitted for publication.

Communications to conferences

Oral contributions

- L. A. Sánchez, A. Díez, J. L. Cruz, and M. V. Andrés, "Measurement of the electrostriction-induced refractive index modulation using long period fiber gratings", (virtual conference), OSA Advanced Photonics Congress, Jul. 2020, SoM2H.

- L. A. Sánchez, A. Díez, J. L. Cruz, and M. V. Andrés, "Accurate measurement of Poisson ratio in optical fibers based on forward-stimulated Brillouin scattering", (virtual conference), Conference on Lasers and Electro-Optics 2021 (CLEO/Europe), Jun. 2021, CH–12.5.

- L. A. Sánchez, A. Díez, J. L. Cruz, and M. V. Andrés, "Discriminative measurement of strain and temperature via transverse acoustic resonances in optical fibers", (virtual conference), XIII Reunión Nacional de Óptica (RNO 2021), Nov. 2021, pp. 345–346.

- L. A. Sánchez, M. Delgado-Pinar, A. Díez, and M. V. Andrés, "Detection of forward Brillouin scattering in optical fibers through optical whispering-gallery modes", (Maastricht, Netherlands), OPTICA Advanced Photonics Congress, Jul. 2022, NpTu4F.5.

- L. A. Sánchez, M. Delgado-Pinar, A. Díez, J. L. Cruz, and M. V. Andrés, "Whispering-gallery modes to investigate opto-mechanical interactions in optical fibers", (Munich, Germany), Conference on Lasers and Electro-Optics/Europe – European Quantum Electronics Virtual Conferences (CLEO/Europe-EQEC 2023), Jun. 2023.

- L. A. Sánchez, C. A. Álvarez-Campo, M. Delgado-Pinar, A. Díez, J. L. Cruz, and M. V. Andrés, "Modal analysis of acoustic resonances in an optical fiber: All-optical excitation and detection", (Bucharest, Romania), International Conference on Transparent Optical Networks (ICTON 2023), Jul. 2023.

Poster contributions

- L. A. Sánchez, A. Carrascosa, L. Escalante-Zárate, J. L. Cruz, A. Díez, and M. V. Andrés, "All-polarization-maintaining mode-locked thulium-doped fiber laser", (Zaragoza, Spain), Reunión Nacional de Optoelectrónica (OPTOEL 2019), Jul. 2019, SP3.FIB01.
- L. A. Sánchez, A. Díez, J. L. Cruz, and M. V. Andrés, "Detection of transverse acoustic resonances in optical fibers using a narrow-band long period grating", (virtual conference), Reunión Nacional de Optoelectrónica (OPTOEL 2021), Jul. 2021, pp. 18–21.
- L. A. Sánchez, C. Cuadrado-Laborde, A. Carrascosa, A. Díez, J. L. Cruz, and M. V. Andrés, "All-polarization maintaining thulium-doped passively modelocked fiber laser under long and short cavity configurations", (virtual conference), XIII Reunión Nacional de Óptica (RNO 2021), Nov. 2021, pp. 298–299.
- L. A. Sánchez, A. Díez, J. L. Cruz, and M. V. Andrés, "Novel methods for the characterization of forward Brillouin scattering in optical fibers and its applications", (Murcia, Spain), XXXVIII Reunión Bienal de la RSEF, Jul. 2022, p. 222.
- C. Cuadrado-Laborde, L. A. Sánchez, J. L. Cruz, A. Díez, and M. V. Andrés, "All polarization-maintaining passively modelocked thulium doped fiber lasers", (San José, Costa Rica), XI Ibero-American Conference on Optics (RIAO 2023), XIV Latin-American Meeting on Optics, Lasers, and Applications (OPTILAS 2023), Mar. 2023.

- O. Ortíz, C. A. Álvarez-Campo, L. A. Sánchez, A. Díez, J. L. Cruz, and M. V. Andrés, "Resonantly opto-excitated transverse acoustic modes in optical fibers", (San José, Costa Rica), XI Ibero-American Conference on Optics (RIAO 2023), XIV Latin-American Meeting on Optics, Lasers, and Applications (OPTILAS 2023), Mar. 2023.
- L. A. Sánchez, A. Díez, J. L. Cruz, and M. V. Andrés, "Expanding the sensing capabilities of forward Brillouin scattering in optical fibers by exploiting the differential response of radial and torsional-radial acoustic modes", (Mons, Belgium), European Workshop on Optical Fibre Sensors (EWOFS 2023), May 2023.
- J. Julián-Barriel, L. A. Sánchez, M. Delgado-Pinar, J. L. Cruz, A. Díez, and M. V. Andrés, "Measurement of the UV-induced radius decrease in a silica fiber by means of optic and acoustic resonances", (Sevilla, Spain), Reunión Nacional de Optoelectrónica (OPTOEL 2023), Jun. 2023.
- A. I. Garrigues-Navarro, L. A. Sánchez, M. Delgado-Pinar, A. Díez, and M. V. Andrés, "Analysis of the frequency response of a dynamically modulated, high Q, optical fiber ring resonator", (Sevilla, Spain), Reunión Nacional de Optoelectrónica (OPTOEL 2023), Jun. 2023.